Université de Lille 1 – Science et Technologies
Ecole Doctorale Science pour l'Ingénieure (EDSPI 72)
Laboratoire De Mécanique de Lille (LML – FRE3723)

Order number : 42588

Dissertation submitted for the degree of

Doctor of Philosophy

# Numerical and experimental modeling of blood flow in the arteries

**Hesham ELKANANI**

Thesis defended the 19 January 2018 in front of jury:

| | | | |
|---|---|---|---|
| Shahrour Isam | Professor | LML, Universite de Lille 1 | President |
| Al-Bahkali Essam | Professor | King Saud University, KSA | Reviewer |
| Erchiqui Fouad | Professor | University of Quebec, Canada | Reviewer |
| Ozdemir Zuhal | Lecturer | The University of Scheifield, UK | Examiner |
| Naji Hassen | Professor | LML, Universite de Lille 1 | Examiner |
| Souli Mhamed | Professor | LML, Universite de Lille 1 | Supervisor |

Université de Lille 1 – Science et Technologies
Ecole Doctorale Science pour l'Ingénieure (EDSPI 72)
Laboratoire De Mécanique de Lille (LML – FRE3723)

Order number : 42588

Dissertation submitted for the degree of

Doctor of Philosophy

# Numerical and experimental modeling of blood flow in the arteries

**Hesham ELKANANI**

Thesis defended the 19 January 2018 in front of jury:

| | | | |
|---|---|---|---|
| Shahrour Isam | Professor | LML, Universite de Lille 1 | President |
| Al-Bahkali Essam | Professor | King Saud University, KSA | Reviewer |
| Erchiqui Fouad | Professor | University of Quebec, Canada | Reviewer |
| Ozdemir Zuhal | Lecturer | The University of Scheifield, UK | Examiner |
| Naji Hassen | Professor | LML, Universite de Lille 1 | Examiner |
| Souli Mhamed | Professor | LML, Universite de Lille 1 | Supervisor |

Université de Lille 1 – Science et Technologies
Ecole Doctorale Science pour l'Ingénieure (EDSPI 72)
Laboratoire De Mécanique de Lille (LML – FRE3723)

Numéro d'order : 42588

Thèse présentée devant l'Université de Lille 1 pour obtenir le grade de Docteur

Spécialité : Mécanique

par

**Hesham ELKANANI**

# Modélisation expérimentale des écoulements sanguins dans les artères

Thèse soutenue le 19 Janvier 2018 devant le jury composé de :

| | | | |
|---|---|---|---|
| Shahrour Isam | Professeur | LML, Universite de Lille 1 | Président du jury |
| Al-Bahkali Essam | Professeur | Université King Saud, KSA | Rapporteur |
| Erchiqui Fouad | Professeur | Université du Québec, Canada | Rapporteur |
| Ozdemir Zuhal | Lecturer | L'Université de Sheffield, UK | Examinateur |
| Naji Hassen | Professor | LML, Universite de Lille 1 | Examinateur |
| Souli Mhamed | Professeur | LML, Université de Lille 1 | Directeur de thèse |

**Keywords:** blood flow, artery, pulse wave velocity (pwv), coupled eulerian lagrangian (cel), fluid structure interaction (fsi), smoothed particles hydrodynamics (sph), noise, vibration and harshness (nvh)

**Mots clés :** flux sanguin, artère, vitesse de l'onde pulsée (pwv), couplage lagrangien eulérien (cel), interaction de la structure fluide (fsi), hydrodynamique des particules lissées, bruit, vibrations et dureté (nvh)

This thesis has been prepared at:

**Laboratoire de Mecanique de Lille FRE 3723**
Av. Paul Langevin
Cite Scientifique
59650 Villeneuve d'Ascq
France
☎ (33)(0)3 20 33 71 52
🖷 (33)(0)3 20 33 71 53
lml@univ-lille1.fr
Web site http://www.univ-lille1.fr/

Art is science made clear.

Wilson Mizner

Science is organized knowledge.
Wisdom is organized life.

Immanuel Kant

Science without religion is lame,
religion without science is blind.

Albert Einstein

The science of today is the
technology of tomorrow.

Edward Teller

**Numerical and experimental modeling of blood flow in the arteries**

# Abstract

The aim of this thesis is to investigate blood flow in arteries using Fluid-Structure Interaction (FSI) numerical approach. There are different approaches which could be used, Finite Element (FE) method for modelling artery wall and either FE or Smoothed Particles Hydrodynamic (SPH) method for blood modeling. In biomedical applications there are very few experimental data accessible in the literatures. In order to investigate the appropriate numerical method to solve our biomedical problem, we apply both FE and SPH methods in well-known applications where the experimental data are available. The first application was Noise, Vibration and Harshness (NVH) and random vibration fatigue analysis of both landing gear of unmanned aerial vehicle and pre-stressed airplane seat tube, where we apply FE method to estimate the life time of the proposed applications. Those are two projects where we published two journal papers and three conference papers as listed in Appendix (A). The aim of those two projects is to validate our fatigue life estimation method to be apply on biomedical problems such as plaque rupture and arteries' valves fatigue life. Due to time restriction we considered those applications as a future work. We apply SPH method in investigate the membrane inflation application where the experiment data are available and we got promising results and hence draw some conclusions. From that study we published one journal paper and one conference paper (Appendix A). Finally, we use Coupled Eulorian Lagrangian (CEL) approach for investigation of Pulse Wave Velocity (PWV) in large arteries where we compare our results with both the theoretical theory and previous work published in the literatures. From this study we conclude the significant parameters affecting both the accuracy and the computational cost where we published a journal paper (Appendix A).

This thesis follows the practices gathered from the mentioned simulation problems. Those practices draw the conclusion about the best practice for modeling blood flow in arteries. This conclusion is that FE method is the most suitable method for modeling blood as it uses less number of elements comparing with SPH method which needs more number of particles and hence more computation time.

**Keywords:** blood flow, artery, pulse wave velocity (pwv), coupled eulerian lagrangian (cel), fluid structure interaction (fsi), smoothed particles hydrodynamics (sph), noise, vibration and harshness (nvh)

**Laboratoire de Mecanique de Lille FRE 3723**
Av. Paul Langevin - Cite Scientifique - 59650 Villeneuve d'Ascq - France

**Modélisation expérimentale des écoulements sanguins dans les artères**

# Résumé

Le but de cette thèse est d'étudier le flux sanguin dans les artères en utilisant l'approche numérique par interaction fluide-structure (FSI). Il existe différentes approches qui pourraient être utilisées, la méthode des éléments finis (FE) pour modéliser la paroi artérielle et FE ou la méthode hydrodynamique de particules lissées (SPH) pour la modélisation du sang. Dans les applications biomédicales, il existe très peu de données expérimentales accessibles dans les littératures. Afin d'étudier la méthode numérique appropriée pour résoudre notre problème biomédical, nous appliquons les méthodes FE et SPH dans des applications bien connues où les données expérimentales sont disponibles. La première application était le bruit, la vibration et la dureté (NVH) et l'analyse aléatoire de la fatigue vibratoire du train d'atterrissage d'un véhicule aérien sans pilote et d'un tube de siège d'avion précontraint où nous appliquons la méthode FE pour estimer la durée de vie des applications proposées. Il s'agit de deux projets dans lesquels nous avons publié deux documents de journal et trois documents de conférence qui figurent à l'annexe (A). Le but de ces deux projets est de valider notre méthode d'estimation de la durée de vie de la fatigue à appliquer à des problèmes biomédicaux tels que la rupture de la plaque et la durée de vie de la fatigue des valves artérielles. En raison de la restriction de temps, nous avons considéré ces applications comme un travail futur. Nous appliquons la méthode SPH dans l'étude de l'application de l'inflation membranaire où les données expérimentales sont disponibles et nous avons obtenu des résultats prometteurs et donc tirer quelques conclusions. À partir de cette étude, nous avons publié un journal et un document de conférence (annexe A). Enfin, nous utilisons l'approche couplée Eulorian Lagrangian (CEL) pour l'étude de la vélocité de l'onde de pulsation (PWV) dans les grandes artères où nous comparons nos résultats avec la théorie et les travaux précédents publiés dans les littératures. À partir de cette étude, nous concluons les paramètres significatifs affectant à la fois l'exactitude et le coût de calcul où nous avons publié un journal (Annexe A). Cette thèse suit les pratiques issues des problèmes de simulation mentionnés. Ces pratiques tirent la conclusion sur les meilleures pratiques pour modéliser le flux sanguin dans les artères. Cette conclusion est que la méthode FE est la méthode la plus appropriée pour modéliser le sang car elle utilise moins de nombre d'éléments en comparaison avec la méthode SPH qui nécessite plus de nombre de particules et donc plus de temps de calcul.

**Mots clés :** flux sanguin, artère, vitesse de l'onde pulsée (pwv), couplage lagrangien eulérien (cel), interaction de la structure fluide (fsi), hydrodynamique des particules lissées, bruit, vibrations et dureté (nvh)

# Acknowledgements

I would like to express my deepest gratitude to Prof. M'Hamed Souli, my thesis supervisor, and Prof. Essam Al-Bahkali for all their guidance, continuous encouragement and support during the preparation of this thesis. My sincere gratitude is also due to my advisory committee, Prof. Isam Shahrour, Prof. Hassen Naji, Prof. Fouad Erchiqui and Dr. Zuhal Ozdemir for having accepted to be examiners of my thesis.

Without support of my dear friend Dr. Mohamed Amdi, I could not overcome any difficulty in my hard times. His kind assistance during the registration and re-registration every year is gratefully acknowledged.

I would like to thank my wife Noha for her love, continuous help and patience. She always gives me the reason to live and progress. Heartfelt thanks are also due to my older sun Eng. Ahmed for his endless and invaluable morale support. No words can express my appreciation and gratitude to my family.

# Contents

# List of Tables

# List of Figures

# Introduction

## Context

Fluid Structure Interaction (FSI) has become more and more the focus of computational engineering in many problems. These problems are computer time consuming and require new stable and accurate coupling algorithms in order to be solved. Over the last few decades, both the new development of coupling algorithms and the advancement of computer performance have enabled some of the problems to be solved and have led to more physical problems that were inaccessible in the past. In the future this trend is likely to continue and to take more realistic problems into account such that those found in many medical applications specially blood flow in arteries.

The aim of this thesis is to investigate blood flow in arteries using FSI numerical approach. There are different approaches which could be used, Finite Element (FE) method for modelling artery wall and either FE method or Smoothed Particles Hydrodynamic (SPH) method for blood modeling. In biomedical applications there are very few experimental data accessible in the literatures. In order to investigate the appropriate numerical method to solve our biomedical problem, we apply both FE and SPH methods in well-known applications where the experimental data are available. The first application was Noise, Vibration and Harshness (NVH) and random vibration fatigue analysis of a notched aluminum beam. The second one is a pre-stressed airplane seat tube. The third one is landing gear of unmanned aerial vehicle, where we apply FE method to estimate the life time of the proposed applications. The last two applications are two projects where we published one ISI paper, with two citations till now, one SCOPUS paper and three conference papers as listed in Appendix (A). The aim of those two projects is to validate our fatigue life estimation method to be applied on biomedical problems such as plaque rupture and arteries' valves fatigue life. Due to time restriction we considered those

applications as a future work. We apply SPH method for investigating the membrane inflation application where the experiment data are available and we got promising results and hence draw some conclusions. From this study, we published an ISI journal paper. Finally, we use Coupled Eulorian Lagrangian (CEL) approach for investigating Pulse Wave Velocity (PWV) of blood flow in large arteries where we validate our results with the theoretical theory, previous work done with different finite elements commercial packages and in vivo data published in the literatures. From this study, we conclude the significant parameters affecting both the accuracy and the computational cost where we published an ISI journal paper (Appendix A).

This thesis follows the practices gathered from the mentioned simulation problems that simulated using Abaqus®, nCode DesignLife® and LS-DYNA® finite element commercial packages. Those practices draw the conclusion about the best practice for modeling blood flow in arteries. This conclusion is that FE method is the most suitable method for modeling blood as it uses less number of elements comparing with SPH method which needs more number of particles and hence more computation time.

The following collaboration projects supported this thesis:

- Numerical Investigation of Pulse Wave Propagation in Arteries Using Fluid Structure Interaction Capabilities, King Saud University, Deanship of Scientific Research, College of Engineering Research Center.
- Experimental and numerical investigation for membrane deployment using SPH and ALE formulations, King Saud University, Deanship of Scientific Research, College of Engineering Research Center.
- Failure and fatigue life estimate of a pre-stressed aircraft seat support tube, King Saud University, Deanship of Scientific Research, College of Engineering Research Center.
- NVH and Random Vibration Fatigue Analysis of a Landing Gear's Leg for an Un-Manned Aerial Vehicle Using Modal Analysis, King Saud University, Deanship of Scientific Research, College of Engineering Research Center.

# State of the Art

## Pulse Wave Velocity (PWV)

PWV is the rate at which a pressure wave propagates along a blood vessel. It is inversely related to vascular compliance and clinicians are considered it as an indication of human blood vessels' stiffness.

The computation of PWV with magnetic resonance imaging (MRI) was first discussed in 1989 [1]. Renewed interest facilitated by faster and more robust MR imaging sequences has led to a recent rapid increase in reported studies with MRI-based PWV measurements. The differences between gold standard, clinical standard, and MRI-based measurements must be understood in the context of global versus regional PWV measurements. The pulse wave can be understood as a wave superimposed on the flow/pressure waveform of the blood. This superimposed pulse wave accelerates and decelerates as it traverses distally in the vasculature relative to the stiffness of the vessel in a given vascular segment. With some of the methods described below, PWV is evaluated regionally in a small area of the vasculature [for example, computing PWV from the temporal shift between two subsequent velocity waveforms. As a result, this PWV measurement is subject to sampling error, such that the area of evaluation could be in a region of stiffness, giving an elevated PWV, or the area of evaluation could be in an area of less stiffness, giving a lower PWV. If a vessel is heterogeneous in stiffness, a PWV measurement could be erroneous depending on the area selected for evaluating PWV. Some methods of computing PWV, including applanation tonometry, Doppler ultrasound and some MRI-based methods, evaluate PWV globally over a very large region of the vasculature [for example, computing PWV from the temporal shift amongst a series of velocity waveforms. While global PWV measurements are minimally prone to sampling bias, areas of stiffness and elevated PWV will be averaged with normal areas of the vasculature. This averaging suppresses differences between individuals with a healthy vasculature and individuals with sporadic areas of stiffness.

The gold standard of measuring PWV is via the use of flow meters or catheter-based pressure probes. Both pressure and flow waveforms within the vasculature can be used to detect the superimposed pulse wave. While these methods provide highly accurate measurements of PWV, the invasiveness involved in placing them intravascularly limits their use to animal studies or to patients otherwise undergoing cardiac catheterization.

Fiber optic probes can be used to measure pressure waveforms. Simultaneous data collection from two probes with a known distance between them are needed to measure PWV, such that the temporal shift between the two pressure waveforms can be used to compute PWV in the region between the tips of the two probes. Fiber optic probes use a Fabry-Perot interferometer configuration [2] and transmit pressure via a microelectromechanical system (MEMS), which houses a diaphragm that deflects in proportion to the amount of strain imparted on it. The pressure sensors contain temperature and pressure resistors. The pressure resistor is a strain gauge attached to a membrane that deforms under pressure; the measurements are corrected via measurements with the temperature resistor. The outer diameter of these pressure probes is often less than 0.5 mm, which minimizes flow disturbances created by their presence within the vasculature. The pressure probes can be inserted with minimal invasiveness via an arterial cut down.

PWV also can be measured with transit-time ultrasound flow meters [3]. These flow meters are placed perivascularly and use an ultrasonic wave to measure flow. Within a given flow meter one ultrasonic wave is transmitted with the direction of flow and another wave is transmitted against the direction of flow. The difference in transit time between the upstream and downstream ultrasonic waves is directly proportional to the velocity of blood within a vessel. Regional PWV could be computed by noting the temporal shift between the flow waveforms of two ultrasonic flow meters separated by a known distance. This distance would need to be measured in vivo with a measuring tape after the flow meters are placed surgically. It may be difficult to measure accurately the separation distance, particularly if the distance between the two flow meters is large and the vessel is tortuous. The greater invasiveness needed to place the ultrasound flow meters perivascularly is a disadvantage of this method relative to the pressure probes.

Both the pressure probes and the ultrasonic flow meters provide a number of advantages that allow for highly accurate PWV measurements. The pressure probes have a high sampling rate, on the order of 100-2,000 Hz. While the two probes can be separated by a substantial distance for global PWV measurements, the high temporal resolution of these probes allows for the assessment of regional PWV. For example, if a subject's PWV is on the order of 10 m/s, and the sampling rate is 1,000 Hz, the two probes need to be separated by as little as 1 cm. Ultrasonic flow meters provide yet higher sampling rates, on the order of >1 MHz. There is effectively no minimum separation distance needed between two ultrasonic flow meters for computing PWV. Another advantage of the high temporal resolution provided by the pressure probes and ultrasonic flow meters is that pressure and flow waveforms are measured in real-time, and thus numerous cardiac cycles can be obtained in a few seconds. A PWV measurement can be obtained for every cardiac cycle, and thus averaged over all cardiac cycles, to account for any variability in PWV. A final advantage of both the fiber optic pressure probes and ultrasonic flow meters is that they can be made MR-compatible; these methods therefore allow for the direct validation of MRI-based PWV measurements.

## Smoothed Particles Hydrodynamic Method (SPH)

"SPH provides a fascinating tool that has some of the properties of molecular dynamics while retaining the attributes of the macroscopic equations of continuum mechanics." J. J. Monaghan [48].

The majority of state-of-the-art simulation tools for continuum mechanics relate to meshbased Finite-Volume (FV) or Finite-Element (FE) solvers. Such traditional grid-based numerical methods provide a good predictive accuracy and can be applied to a wide range of engineering problems. However, these approaches have limitations, especially if it comes to applications that involve: large relative motions, multiple interacting rigid structures, multiple phases and continua, complex free surface flows, large deformations, and fragmentation of solids.

Contrary to this, mesh-free methods solve the governing equations without a rigid alignment to grid structures or discrete topologies. That way, many of the above mentioned drawbacks of mesh-based procedures can easily be overcome. Several mesh-free techniques have been developed in the last decades; good summaries are given e.g. in a review paper of Belytschko et al. [49], the PhD thesis of Chaniotis [50] and the book of Liu [6]. Some of the formulations still incorporate grids as necessary ingredients of the numerical method. On the contrary, Smoothed-Particle-Hydrodynamics (SPH) can be considered a truly mesh-free approach. In SPH, the continuum is descritised by set of finite particles that can arbitrarily move. By using an interpolation technique known as reproducing kernel approximation, field values can be approximated at a certain point as a weighted average over a set of nearby particles.

The method was originally developed in 1977 independently by Lucy [51] and Gingold and Monaghan [52] to study cosmological problems. Since then, it has considerably matured [48], [53], [54] and was successfully used to study problems from a large variety of disciplines. Its highly diverse range of applications has recently been extended to marine, hydraulic, geoenvironmental and geotechnical engineering problems. Published examples include, but are not limited to, general free-surface flows [55], ship dynamics [56], landslide simulations [57], [58] reservoir flushing [59], flood simulations [60] or embankment failures [61], [62].

The SPH method developed originally for solving astrophysics problem has been extended to solid mechanics by Libersky et al. [63] to model problems involving large deformation including high velocity impact. SPH method provides many advantages in modeling severe deformation as compared to classical FEM formulation which suffers from high mesh distortion. The method was first introduced by Lucy [64] and Gingold and Monaghan [65] for gas dynamic problems and for problems where the main concern is a set of discrete physical particles than the continuum media. The method was extended to solve high velocity impact in solid mechanics, CFD applications governed by Navier-Stokes equations and fluid structure interaction problems.

It is well known from previous papers, that SPH method suffers from lack of consistency, that can lead to poor accuracy of motion approximation. Unlike Finite Element, interpolation in SPH method cannot reproduce constant and linear functions.

## NVH and Random Vibration Analysis

Most real fatigue loadings are random processes in respect of frequency and stress amplitude. Estimating fatigue damage with Power Spectrum Density (PSD) was first proposed by Rice [76] in 1954. The stress power spectra density (PSD) represents the frequency domain approach input into the fatigue. This is a scalar function that describes how the power of the time signal is distributed among frequencies [77]. Mathematically this function can be obtained by using a Fourier transform of the stress time history's autocorrelation function, and its area represents the signal's standard deviation. It is clear that PSD is the most complete and concise representation of a random process [78]. Finite element analysis is very efficient in taking the PSD of applied loads and determining the PSD of the resulting stresses at various points in the structure. A method of taking the PSD of stress and calculating fatigue lives therefore has attractions. Much of the early work on fatigue analysis from PSD's was carried out by NASA in order to determine the fatigue damage caused by vibration and buffeting of space vehicles.

Finite element analysis is very efficient in taking the Power Spectral Density (PSD) of applied loads and determining the PSD of the resulting stresses at various points in the structure. A method of taking the PSD of stress and calculating fatigue lives therefore has attractions.

Random response linear dynamic analysis is used to predict the response of a structure subjected to a nondeterministic continuous excitation that is expressed in a statistical sense by a cross-spectral density (CSD) matrix. The random response procedure uses the set of eigenmodes extracted in a previous eigenfrequency step to calculate the corresponding power spectral densities (PSD) of response variables (stresses, strains, displacements, etc.) and, hence—if required—the variance and root mean square values of these same

variables. This section provides brief definitions and explanations of the terms used in this type of analysis based on the book by Clough and Penzien [80].

Examples of random response analysis are the study of the response of an airplane to turbulence; the response of a car to road surface imperfections; the response of a structure to noise, such as the “jet noise” emitted by a jet engine; and the response of a building to an earthquake.

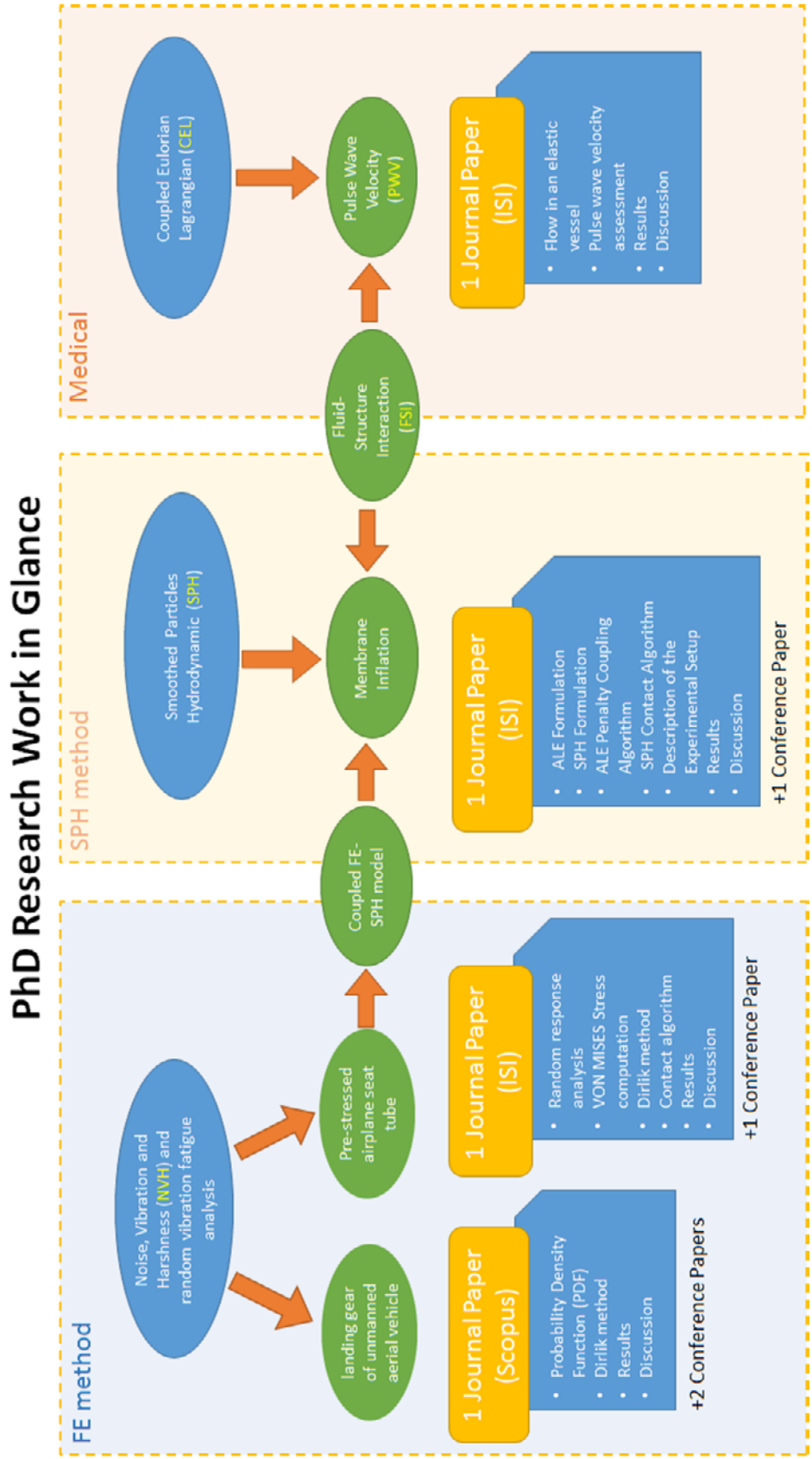

## Thesis objectives and development

The objectives of this thesis are as follows:

- Investigation and implementation a reliable model for PWV assessment in arteries.
- Validation of SPH, ALE, FSI and CEL methods in Abaqus®.
- Validation of fatigue life time estimation in LS-DYNA® and nCode DesignLifeV coupled Abaqus®.

Chapter 1 presents a reliable computational scheme to serve in pulse wave velocity (PWV) assessment in large arteries. In this investigation, the simulation of PWV was conducted using a three-dimension elastic tube representing an artery. The constitutive material model specific for vascular applications was applied to the tube material. The fluid was defined with an equation of state representing the blood material. The onset of a velocity pulse was applied at the tube inlet to produce wave propagation. The Coupled Eulerian−Lagrangian (CEL) modeling technique with fluid-structure interaction (FSI) was implemented. The scaling of sound speed and its effect on results and computing time is discussed. Two methods were used to assist the PWV measurement.

In chapter 2, we present experimental and numerical investigation for membrane deployment using SPH and ALE formulations. The new formulations SPH method (Smooth Particle Hydrodynamic), which have been developed for FSI applications using mesh free methods, is introduced. The mathematical and numerical implementation of the ALE and SPH formulations are, also, described in this chapter. To validate the statement, we perform a simulation of membrane deployment generated by high pressurized gas.

In chapter 3, Noise, Vibration, and Harshness (NVH) study is applied to three case studies: fatigue life prediction of a notched aluminium beam using Abaqus® and nCode DesignLife®, fatigue life estimate of a pre-stressed aircraft seat support tube and fatigue life estimate of landing gear's leg. In this study we investigate the effect of pre-stresses on modal analysis and demonstrate different methods used for life time estimation. A notched

aluminum beam is considered as a benchmark for many literatures [4] where the experimental data and results obtained using other commercial codes are available. So, it was selected as a first case study in order to test our approach for random vibration analysis and fatigue life prediction.

Chapter 1

# Numerical Investigation of Pulse Wave Propagation in Arteries Using Fluid Structure Interaction Capabilities

Partly adapted from postprint version of:

**Numerical Investigation of Pulse Wave Propagation in Arteries Using Fluid Structure Interaction Capabilities**

Hisham Elkenani[1], Essam Al-Bahkali[1] and Mhamed Souli[2]

[1]Department of Mechanical Engineering, King Saud University, P.O. Box 800, Riyadh 11421, Saudi Arabia

[2]Laboratoire de Mécanique de Lille, UMR CNRS 8107, Villeneuve-d'Ascq, France

Published in:
Computational and Mathematical Methods in Medicine
Volume 2017, Article ID 4198095, Pages 1-12, 2017
https://doi.org/10.1155/2017/4198095

In this chapter, we present a reliable computational scheme to serve in pulse wave velocity (PWV) assessment in large arteries. PWV is the rate at which a pressure wave propagates along a blood vessel. It is inversely related to vascular compliance and clinicians are considered it as an indication of human blood vessels' stiffness. In this investigation, the simulation of PWV was conducted using a three-dimension elastic tube representing an artery. The constitutive material model specific for vascular applications was applied to the tube material. The fluid was defined with an equation of state representing the blood material. The onset of a velocity pulse was applied at the tube inlet to produce wave propagation. The Coupled Eulerian−Lagrangian (CEL) modeling technique with fluid-structure interaction (FSI) was implemented. The scaling of sound speed and its effect on results and computing time is discussed, and we concluded that a value of 60 m/s was suitable for simulating vascular biomechanical problems. Two methods were used to assist the PWV measurement: foot-to-foot measurement of velocity waveforms and slope of the regression line of the wall radial-deflection wave peaks throughout a contour plot. Both methods showed coincident results. Results were approximately 6% less than those calculated from the Moens−Korteweg equation, which describes the PWV in elastic tubes. The proposed method was able to describe the increase in the stiffness of the walls of large human arteries via the PWV estimates.

## 1.1 Introduction

Computational analysis of cardiovascular problems incorporating FSI is a challenging problem. Detailed analysis of the blood flow field and artery wall behavior can assist in clinicians' assessment of vascular diseases [5]. The first person to investigate a formula for the velocity of pressure waves in a thin elastic tube was Young [6] in 1808. Womersley [7] investigated the dynamic response of a tube with a sinusoidal flow and defined an analytical solution for the flow domain.

In this study, we investigated the propagation of a pulse wave through an elastic vessel. This application is of clinical relevance as PWV measurements are currently considered to be the clinical gold standard measure of arterial stiffness [8]. PWV is typically a

disturbance's propagation speed through a vessel resulting from the flow pressure. As blood is an almost-incompressible fluid [9] [10] [11], the finite PWV is mainly the result of the FSI between the local pressure of the blood on the vessel wall and the resultant wall deformation it causes. To validate the obtained results, we used the same model used by Kuntz et al. [12] and Penrose et al. [13] who validated their simulation, conducted with ANSYS-CFX commercial software, with the theoretical results obtained by the Moens−Korteweg equation [14]. Moatamedi et al. [15] and Souli et al. [16] used the same model in their study and validated their simulation, conducted with LS-DYNA commercial package, with those obtained from the Moens−Korteweg equation.

Shahmirzadi et al. [17] validated their work conducted with ABAQUS explicit solver with the Moens−Korteweg equation, but they used a different model. Fukui et al. [18] implemented their model using the commercial code Radioss (Altair Engineering) to investigate the effect of both elasticity and wall thickness on PWV through a long elastic tube.

Because PWV techniques will be at the center of this thesis' medical application, a comprehensive analysis of the phenomena and clinical and technical implications of measuring PWV is now provided. Section 1.1 initiates the discussion with a formal definition of the PWV parameter. Section 1.2 provides theoretical evidence on the relationship between PWV and arterial stiffness. Section 1.3 studies clinical aspects and applications of PWV, going from the non-invasive assessment of arterial stiffness to the generation of cardiovascular risk factor markers. Section 1.4 provides a comprehensive summary of the state of the art in PWV measuring techniques. The subsequent sections demonstrate the numerical model and validation of the obtained results with both theoretical theory and in vivo data.

### 1.1.1 Definition of Pulse wave velocity

In cardiovascular research and clinical practice, PWV refers to the velocity of pressure pulses that propagate along the arterial tree. In particular, one is interested in those pressure pulses generated during left ventricular ejection: at the opening of the aortic valve, the sudden rise of aortic pressure is absorbed by the elastic aorta walls. Subsequently a pulse

wave naturally propagates along the aorta exchanging energy between the aortic wall and the aortic blood flow (Figure 1-1).

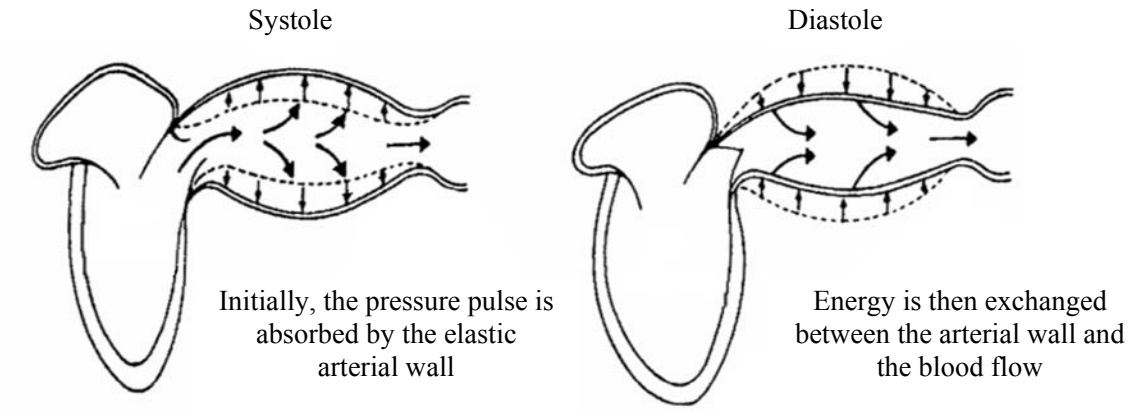


Figure 1-1 Genesis of pressure pulses: after the opening of the aortic valve the pulse propagates through the aorta exchanging energy between the aortic wall and the blood flow. Adapted from [19].

At each arterial bifurcation, a fraction of the energy is transmitted to the following arteries, while a portion is reflected backwards. Note that one can easily palpate the arrival of arterial pressure pulses at any superficial artery, such as the temporal, carotid or radial artery: already in the year 1500, traditional Chinese medicine performed clinical diagnosis by palpating the arrival of pressure pulses at the radial artery [20]. But why do clinicians nowadays gather interest in the velocity of such pulses, and especially in the aorta? The reason is that the velocity of propagation of aortic pressure pulses depends on the elastic and geometric properties of the aortic wall. We will show later that while arterial stiffness is difficult to measure non-invasively, PWV is nowadays available in vivo to clinicians. Hence, the PWV parameter is an easily-accessible potential surrogate for the constitutive properties of the arterial wall.

## 1.2 Pulse wave velocity and stiffness: the Moens-Korteweg equation

It has already been stated that modifications of the biomechanical properties of the arterial wall will induce changes at the velocity at which pressure pulses travel along it. The goal of the current section is to provide a simple mathematical model supporting this relationship. In particular, the proposed model [21] aims at establishing the relationship between PWV and biomechanical characteristics such as wall stiffness, wall thickness and arterial diameter via the commonly-known Moens-Korteweg equation.

The derivation of the equation relies on a mass model of a volume of blood moving through an arterial segment (Figure 1-2), as well as on a model of the biomechanics of the arterial wall (Figure 1-3). Both models assume that the volume of blood $V$ induces a flow $Q$ while undergoing a pressure $P$. The geometry of the models is defined by an arterial length $dx$, an internal arterial radius $R$, a constant internal area $A$, and an arterial wall thickness h. Blood density is assumed to be $\rho$, wall shear stress $\tau$, and wall circumferential stress $\sigma_\theta$.

The Moens-Korteweg derivation startthe law of mass conservation, *i.e.*:

$$
\begin{aligned}
Q_{in} - Q_{out} &= \frac{dV}{dt} \\
Q - (Q + dQ) &= \frac{d(Adx)}{dt} \\
-dQ &= \frac{dA}{dt}\, dx \\
\frac{dQ}{dx} + \frac{dA}{dt} &= 0
\end{aligned}
\qquad (1\text{-}1)
$$

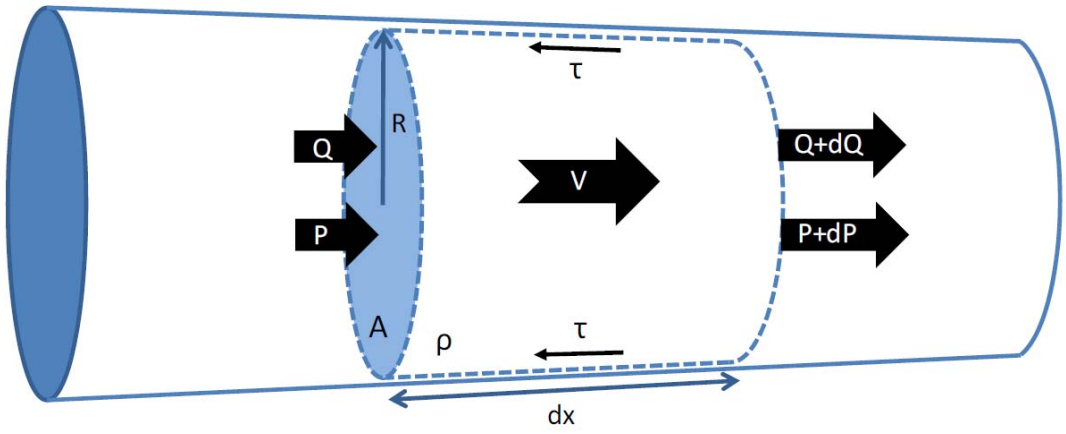


Figure 1-2 Geometrical and mass model of a volume of blood moving along an artery. R: arterial radius, dx: arterial length, P: influx pressure, P+dP: outflux pressure, Q: influx blood flow, Q+dQ: outflux blood flow, V: blood velocity, τ: wall shear stress, and ρ: blood density.

Imposing as well the law of momentum conservation (Newton's law) one obtains:

$$\sum F_x = m\, a_x$$

$$\big(P - (P + dP)\big)A - \tau 2\pi R dx = m\, a_x$$

$$\big(P - (P + dP)\big)A - \tau 2\pi R dx = \rho A dx \frac{dV}{dt} \qquad (1\text{-}2)$$

$$-\frac{dP}{dx}A - \tau 2\pi R = \rho A \frac{dV}{dt}$$

Assuming now wall shear stress (friction) to be negligible, and assuming $A$ to be constant along $dx$ (compared to $V$) Eq. 1-2 becomes:

$$-\frac{dP}{dx}A = \rho\frac{dAV}{dt}$$

$$-\frac{dP}{dx}A = \rho\frac{dQ}{dt} \qquad (1\text{-}3)$$

$$\frac{dQ}{dt} = -\frac{A}{\rho}\frac{dP}{dx}$$

We define now arterial compliance to be $C_A = \frac{dA}{dP}$. Recalling the mass conservation expression of Eq. 1-1, and assuming $C_A$ to be constant in time, one obtains:

$$\frac{dA}{dt} + \frac{dQ}{dx} = 0$$

$$\frac{dA}{dP}\frac{dP}{dt} + \frac{dQ}{dx} = 0$$

$$C_A\frac{dP}{dt} + \frac{dQ}{dx} = 0 \qquad (1\text{-}4)$$

$$C_A\frac{\partial^2 P}{\partial t^2} + \frac{\partial^2 Q}{\partial x\,\partial t} = 0$$

We rewrite now the momentum conservation expression of Eq.1-3 in order to contain the $\frac{\partial^2 Q}{\partial x\,\partial t}$ term as well, assuming A to be a constant arterial section:

$$\frac{\partial^2 Q}{\partial x\,\partial t} = -\frac{A}{\rho}\frac{\partial^2 P}{\partial x^2} \qquad (1\text{-}5)$$

Finally including the modified momentum expression of Eq. 1-5 into the modified mass expression of Eq.1-4, one obtains the following wave equation:

$$\frac{\partial^2 P}{\partial t^2} = \frac{A}{\rho C_A}\frac{\partial^2 P}{\partial x^2} \qquad (1\text{-}6)$$

Therefore, according to the proposed model, a pressure wave $P(x,t)$ travels along an arterial segment obeying a wave equation, i.e.

$$\frac{\partial^2 P}{\partial t^2} = c^2\frac{\partial^2 P}{\partial x^2} \qquad (1\text{-}7)$$

with a propagation speed determined by:

$$c = \sqrt{\frac{A}{\rho C_A}} \qquad (1\text{-}8)$$

The propagation speed of a pressure pulse travelling along an artery is thus expected to be inversely related to the arterial compliance, i.e. the more compliant the artery the slower the pulse will propagate. Eq. 1-8 is known as Bramwell-Hill equation [22].

Developing further the definition of arterial compliance one obtains:

$$C_A = \frac{dA}{dP} = \frac{d(\pi R^2)}{dP} = 2\pi R\frac{dR}{dP} \qquad (1\text{-}9)$$

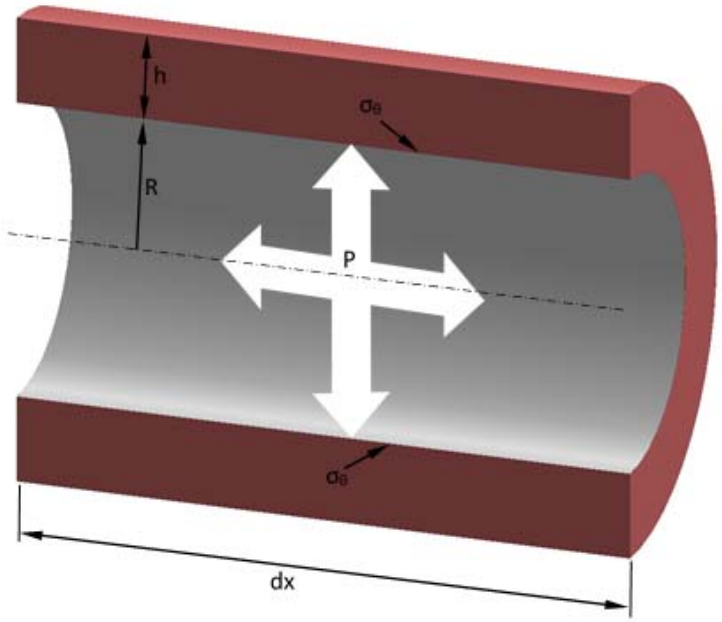


Figure 1-3 Biomechanical model of the arterial wall. *R*: internal arterial radius, *h*: thickness, *dx*: segment length, $\sigma_\theta$: wall circumferential stress, and *P*: arterial pressure.

And by inserting Eq.1-9 into the Eq. 1-8 a modified Bramwell-Hill equation is obtained:

$$c = \sqrt{\frac{R}{2\rho}\frac{dP}{dR}} \qquad (1\text{-}10)$$

Unfortunately, both the Bramwell-Hill equation and its modified version are unable to predict the propagation speed of pressure pulses along an artery from the stiffness of its wall. In the following we aim at expressing the term $\frac{dP}{dR}$ appearing in the modified Bramwell-Hill equation as a function of the wall Young's modulus.

Based on the arterial wall biomechanical model proposed by Figure 1-3, we start by applying the momentum conservation law to all tangential components:

$$\begin{gathered}\sum F_\theta = 0 \\ P2Rdx - 2\sigma_\theta h dx = 0 \\ \sigma_\theta = \frac{PR}{h}\end{gathered} \quad (1\text{-}11)$$

obtaining the so-called Laplace law. By differentiating Eq. 1-11 one obtains:

$$d\sigma_\theta = \frac{RdP}{h} + \frac{PdR}{h} - \frac{PRdh}{h^2} \quad (1\text{-}12)$$

Assuming the arterial wall to be incompressible and thin, i.e. $h \ll R$,

$$\begin{gathered}\pi(R+h)^2 - \pi R^2 = \gamma \\ h(2R+h) = \gamma' \\ hR = \gamma'' \\ dr\ h = -r\ dh\end{gathered} \quad (1\text{-}13)$$

one obtains a differenced Laplace law in the form:

$$d\sigma_\theta = \frac{RdP}{h} + 2\frac{PdR}{h} \quad (1\text{-}14)$$

At this point, we recall the concept of Young's elastic modulus and we aim at introducing it into Eq. 1-14. The Young's elastic modulus describes the measured arterial wall stress ($\sigma_\theta$) when a given strain ($\varepsilon$) is applied to it, i.e.:

$$E_{inc} = \frac{d\sigma_\theta}{d\varepsilon} = \frac{d\sigma_\theta}{dR/_R} \quad (1\text{-}15)$$

Merging now the geometrical description of the arterial wall (Eq. 1-14) together with the introduced biomechanical variable of Eq. 1-15, one obtains:

$$\begin{gathered}E_{inc} = \frac{R^2 dP}{hdR} + 2\frac{PR}{h} \\ E_{inc} = \frac{R^2 dP}{hdR} + 2\sigma_\theta\end{gathered} \quad (1\text{-}16)$$

Assuming now the $\sigma_\theta$ term to be negligible, one obtains the searched relationship between $\frac{dP}{dR}$ and Young's modulus of the arterial wall:

$$E_{inc} = \frac{R^2}{h}\frac{dP}{dR} \qquad (1\text{-}17)$$

Finally introducing the Young's modulus expression of Eq. 1-17 into the modified Bramwell-Hill expression of Eq. 1-10, one obtains the so-called Moens-Korteweg equation:

$$c = \text{PWV} = \sqrt{\frac{hE_{inc}}{2\rho R}} \qquad (1\text{-}18)$$

Accordingly, the speed of propagation of a pressure pulse along the arterial wall depends on:

- the biomechanics properties of the wall: and in particular its stiffness $E_{inc}$ or Young's modulus,
- the geometry of the wall, and in particular its thickness *h* and radius *R*,
- and the density of blood.

Even though the derivation of the Moens-Korteweg model relies on several (and severe) simplifications, it provides an intuitive insight on the propagation phenomenon in arteries predicting that the stiffer the artery (increased $E_{inc}$) the faster a pressure pulse will propagate along it. Therefore, for large elastic arteries such the aorta where the thickness to radius ratio is almost invariable, PWV is expected to carry relevant information related to arterial stiffness.

## 1.3 Clinical Aspects of Pulse Wave Velocity

Recall that the present thesis aims at exploiting PWV as a technique to non-invasively and non-occlusively measure blood pressure. Nevertheless, it is of capital importance to understand the clinical context in which PWV techniques have been historically developed. Therefore, this section reviews the clinical aspects and implications of PWV measurements, and in particular, in relation to the assessment of arterial stiffness.

Cardiovascular disease is the leading cause of morbidity and mortality in western countries and is associated with changes in the arterial structure and function. It is today generally

accepted that arterial stiffening has a central role in the development of such diseases. Aortic PWV is considered the gold standard for the assessment of arterial stiffness and is one of the most robust parameters for the prediction of cardiovascular events [23]. Because the structure of the arterial wall differs between the central (elastic) and the peripheral (muscular) arteries, several PWV values are encountered along the arterial tree, with increasing stiffness when moving to the periphery. Because carotid-to-femoral PWV is considered as the standard measurement of aortic arterial stiffness, we will refer to it as simply PWV.

In the following we review the most important factors determining PWV of elastic arteries, we analyze the pathophysiological consequences of increased arterial stiffness and, we highlight the clinical relevance of PWV as an independent marker of cardiovascular risk.

### 1.3.1 **Major determinants of Pulse Wave Velocity**

Before elucidating the role that PWV plays in the generation and diagnosis of pathological situations, it is necessary to understand which are its determinant factors under normal conditions. It is currently accepted that the four major determinants of PWV are age, blood pressure, gender and heart rate.

Age affects the wall properties of central elastic arteries (aorta, carotid, iliac) in a different manner than in muscular arteries (brachial, radial, femoral, popliteal). With increasing age the pulsatile strain breaks the elastic fibers, which are replaced by collagen [24]. These changes in the arterial structure lead to increased arterial stiffness, and consequently to increased central PWV (Figure 1-4). On the other hand, there is only little alteration of distensibility of the muscular, i.e. distal, arteries with age [23], [25]. This fact supports the use of generalized transfer functions to calculate the central aortic pressure wave from the radial pressure wave in adults of all ages.

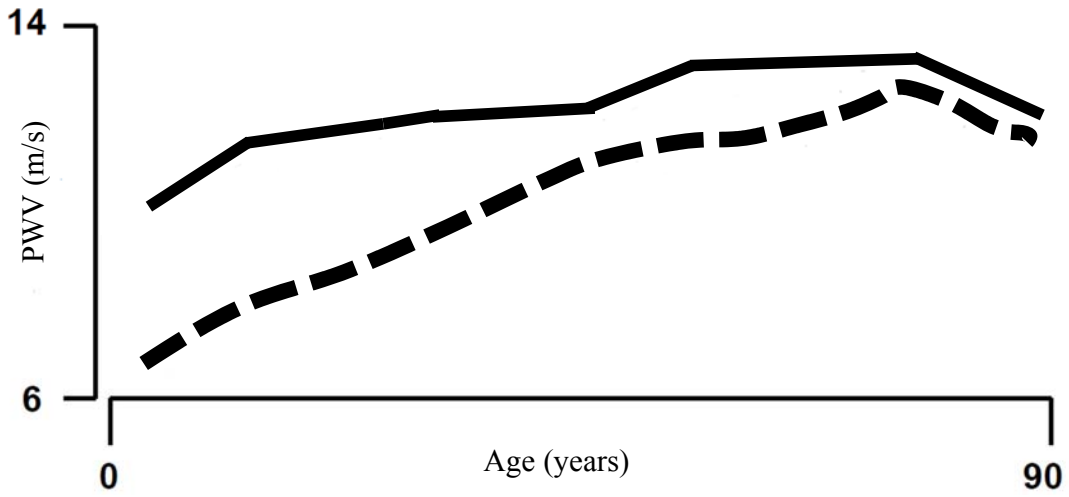


Figure 1-4 The dependency of PWV with age for central elastic arteries (dashed line) and peripheral muscular arteries (continuous line). Adapted from [19].

Arterial blood pressure is also a major determinant of PWV. Increased blood pressure is associated with increased arterial stiffness and vice versa. Ejection of blood into the aorta generates a pressure wave that travels along the whole arterial vascular tree. A reflected wave that travels backwards to the ascending aorta is principally generated in the small peripheral resistance arterioles. With increasing arterial stiffness, both the forward and the reflected waves propagate more rapidly along the vessels. Consequently, instead of reaching back the aorta during the diastole, the reflected pulse wave reaches it during the systole. This results in an increase of aortic pressure during systole and reduced pressure during diastole, thus leading to an increase of the so-called Pulsatile Pulse (PP) parameter (Figure 1-5). Asmar studied large untreated populations of normotensive and hypertensive subjects and found that the two major determinants of PWV were age and systolic blood pressure in both groups [22]. This result confirms the close interdependence between systolic blood pressure and arterial stiffness.

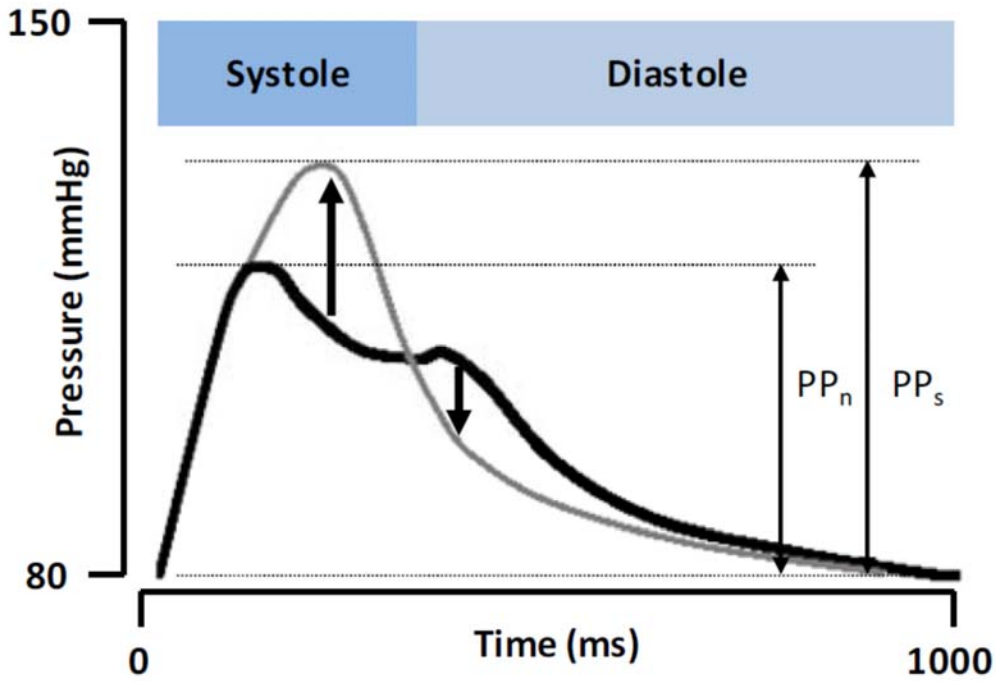


Figure 1-5 Consequences of increased arterial stiffness on central blood pressure: increase of systolic and decrease of diastolic central pressures. Pulsatile Pressure is defined as the difference of both pressure amplitudes. $PP_n$ stands for PP under normal condition.

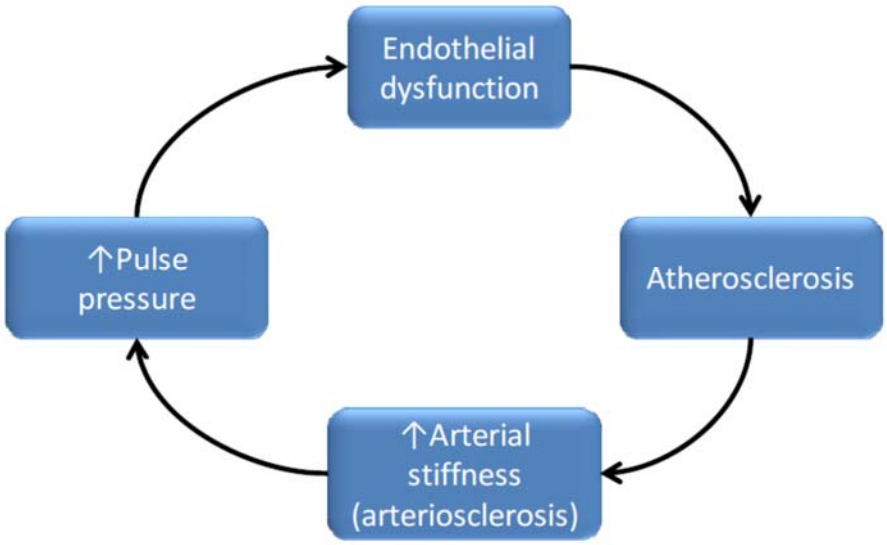


Figure 1-6 Vicious circle of events resulting from endothelial dysfunction and augmented arterial stiffness.

Concerning gender, studies in children revealed no gender difference in PWV, whereas in young and middle age, healthy adult men displayed higher PWV values compared to women [26], [27]. Indeed premenopausal women show lower carotid-radial PWV values than age matched men, but carotid-femoral PWV is found to be similar. Once women become postmenopausal, PWV values become similar to those of age-matched men [26].

Heart rate is related to PWV through two independent mechanisms. Firstly, heart rate influences PWV because of the frequency-dependant viscoelasticity of the arterial wall: if heart rate increases, the time allowed to the vessels to distend is reduced, resulting in an increased rigidity of the arterial wall. Hence, increasing rate is associated with increasing arterial stiffness. In a recent study [28], it was showed that particularly in hypertensive patients increased heart rate was one of the major determinants of accelerated progression of arterial stiffness. Secondly, heart rate is related to PWV through the influence of the sympathetic nervous system: sympathetic activation is associated with increased stiffness of the arteries [29] due to an increase in heart rate, blood pressure and smooth muscle cells tonus.

## 1.4 The State of the Art in PWV Measuring Techniques

The computation of PWV with magnetic resonance imaging (MRI) was first discussed in 1989 [1]. Renewed interest facilitated by faster and more robust MR imaging sequences has led to a recent rapid increase in reported studies with MRI-based PWV measurements. The purpose of this review is to summarize and synthesize the state-of-the-art in MRI-based PWV measurements. In addition, both gold standard and clinical standard methods of computing PWV will be reviewed briefly.

The differences between gold standard, clinical standard, and MRI-based measurements must be understood in the context of global versus regional PWV measurements (Figure 1-7). The pulse wave can be understood as a wave superimposed on the flow/pressure waveform of the blood. This superimposed pulse wave accelerates and decelerates as it traverses distally in the vasculature relative to the stiffness of the vessel in a given vascular segment. With some of the methods described below, PWV is evaluated regionally in a small area of the vasculature [for example, computing PWV from the temporal shift

between two subsequent velocity waveforms (Figure 1-7B). As a result, this PWV measurement is subject to sampling error, such that the area of evaluation could be in a region of stiffness, giving an elevated PWV, or the area of evaluation could be in an area of less stiffness, giving a lower PWV. If a vessel is heterogeneous in stiffness, a PWV measurement could be erroneous depending on the area selected for evaluating PWV. Some methods of computing PWV, including applanation tonometry, Doppler ultrasound and some MRI-based methods, evaluate PWV globally over a very large region of the vasculature [for example, computing PWV from the temporal shift amongst a series of velocity waveforms (Figure 1-7B). While global PWV measurements are minimally prone to sampling bias, areas of stiffness and elevated PWV will be averaged with normal areas of the vasculature. This averaging suppresses differences between individuals with a healthy vasculature and individuals with sporadic areas of stiffness.

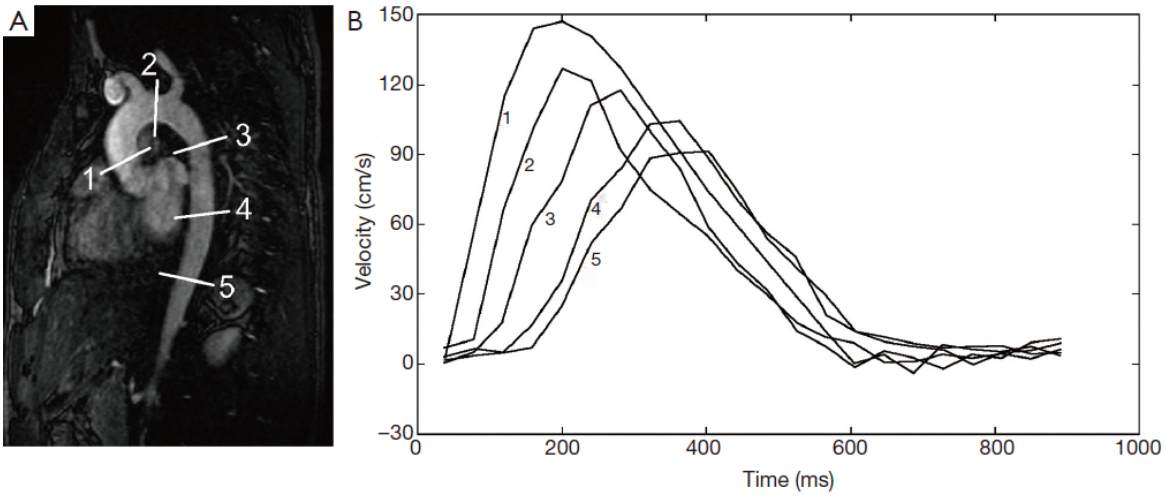


Figure 1-7 This double oblique view of the thoracic aorta from a magnetic resonance angiogram (MRA) (A) is used to show five slices from which aortic mean velocity waveforms are derived from a flow sensitive MR imaging sequence. (B) From the five velocity waveforms a temporal shift can be appreciated as the aorta is traversed. This shift can be used to compute the pulse wave velocity either regionally, for example from any two of these waveforms, or globally, using all of the waveforms. Note that maximum velocity decreases progressively at downstream slice locations; maximum velocity decreases for a number of reasons, including resistance to flow and loss of flow volume from vessels branching from the aorta. The 5 flow waveforms in (B) are derived from the 5 slices in (A). [30]

## 1.5 Gold Standard Measurements of Pulse Wave Velocity

The gold standard of measuring PWV is via the use of flow meters or catheter-based pressure probes. Both pressure and flow waveforms within the vasculature can be used to detect the superimposed pulse wave. While these methods provide highly accurate measurements of PWV, the invasiveness involved in placing them intravascularly limits their use to animal studies or to patients otherwise undergoing cardiac catheterization.

Fiber optic probes can be used to measure pressure waveforms. Simultaneous data collection from two probes with a known distance between them are needed to measure PWV, such that the temporal shift between the two pressure waveforms can be used to compute PWV in the region between the tips of the two probes. Fiber optic probes use a Fabry-Perot interferometer configuration [2] and transmit pressure via a microelectromechanical system (MEMS), which houses a diaphragm that deflects in proportion to the amount of strain imparted on it. The pressure sensors contain temperature and pressure resistors. The pressure resistor is a strain gauge attached to a membrane that deforms under pressure; the measurements are corrected via measurements with the temperature resistor. The outer diameter of these pressure probes is often less than 0.5 mm, which minimizes flow disturbances created by their presence within the vasculature. The pressure probes can be inserted with minimal invasiveness via an arterial cut down.

PWV also can be measured with transit-time ultrasound flow meters [3]. These flow meters are placed perivascularly and use an ultrasonic wave to measure flow. Within a given flow meter one ultrasonic wave is transmitted with the direction of flow and another wave is transmitted against the direction of flow. The difference in transit time between the upstream and downstream ultrasonic waves is directly proportional to the velocity of blood within a vessel. Regional PWV could be computed by noting the temporal shift between the flow waveforms of two ultrasonic flow meters separated by a known distance. This distance would need to be measured in vivo with a measuring tape after the flow meters are placed surgically. It may be difficult to measure accurately the separation distance, particularly if the distance between the two flow meters is large and the vessel is tortuous.

The greater invasiveness needed to place the ultrasound flow meters perivascularly is a disadvantage of this method relative to the pressure probes.

Both the pressure probes and the ultrasonic flow meters provide a number of advantages that allow for highly accurate PWV measurements. The pressure probes have a high sampling rate, on the order of 100-2,000 Hz. While the two probes can be separated by a substantial distance for global PWV measurements, the high temporal resolution of these probes allows for the assessment of regional PWV. For example, if a subject's PWV is on the order of 10 m/s, and the sampling rate is 1,000 Hz, the two probes need to be separated by as little as 1 cm. Ultrasonic flow meters provide yet higher sampling rates, on the order of >1 MHz. There is effectively no minimum separation distance needed between two ultrasonic flow meters for computing PWV. Another advantage of the high temporal resolution provided by the pressure probes and ultrasonic flow meters is that pressure and flow waveforms are measured in real-time, and thus numerous cardiac cycles can be obtained in a few seconds. A PWV measurement can be obtained for every cardiac cycle, and thus averaged over all cardiac cycles, to account for any variability in PWV. A final advantage of both the fiber optic pressure probes and ultrasonic flow meters is that they can be made MR-compatible; these methods therefore allow for the direct validation of MRI-based PWV measurements.

The above methods provide high temporal resolution such that the shape of the pressure or velocity/flow waveform can be accurately depicted. On the other hand, sampling at lower temporal resolution can substantially change the shape of the waveform (Figure 1-8). As discussed below, PWV is computed from MR data using various characteristics of the waveform, such as the peak and foot of the waveform. As the temporal distance between sampling points becomes greater, the discretization error increases and there is a greater likelihood that these waveform characteristics will be misrepresented, leading to inaccurate PWV measurements.

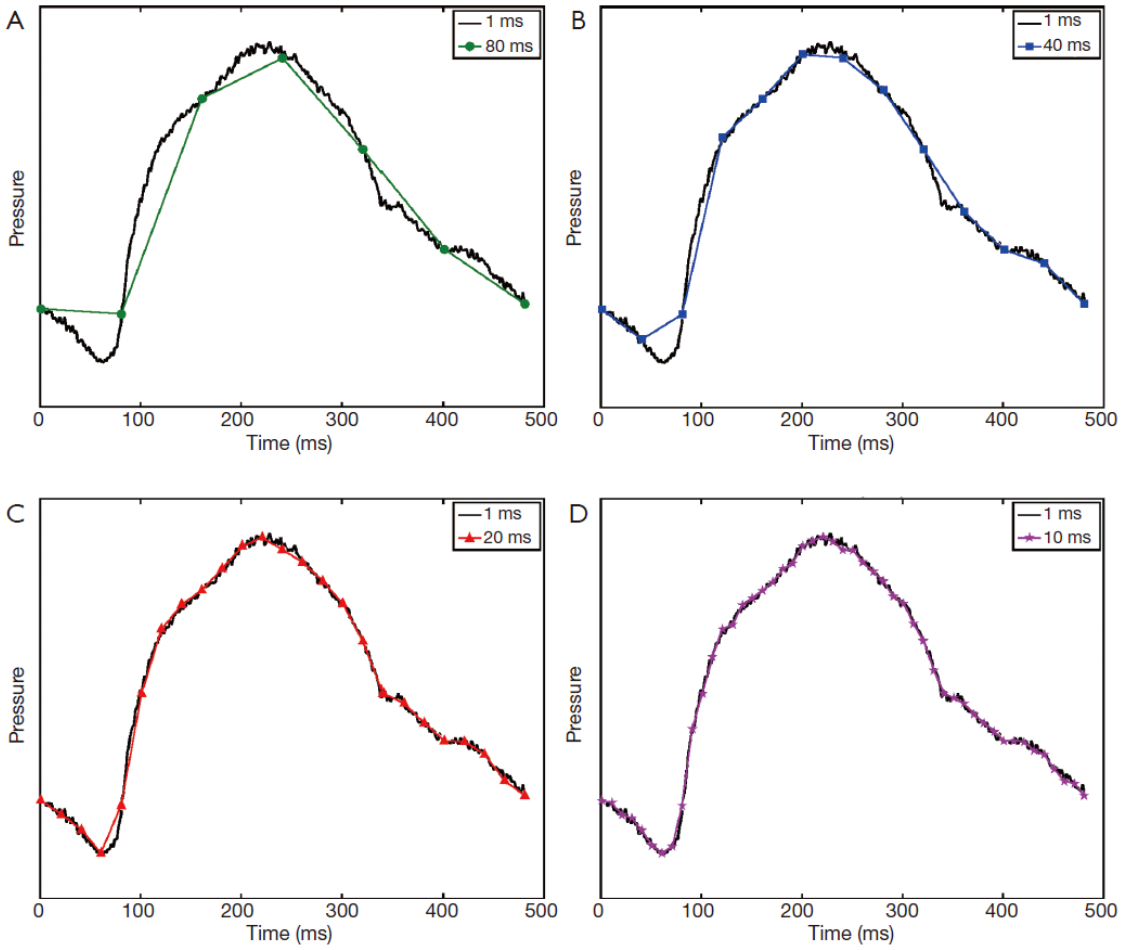


Figure 1-8 Sampling an aortic pressure waveform at 80 ms (A), 40 ms (B), 20 ms (C), and 10 ms (D) as compared to sampling at 1 ms. These high temporal resolution 1 ms data were acquired in the aorta of a pig with a fiber optic intravascular pressure sensor. For (A), (B), and (C) the waveform was downsampled to demonstrate that the shape of the waveform is highly dependent on adequate sampling of the data. [3]

## 1.6 Flow in an Elastic Vessel

The transient progression of a pressure pulse through a tube has been investigated by many researchers over the years. A good review of this research is available [31]. The first work on wave propagation in an elastic tube was presented by Moens and Korteweg at the end of the 19th century [14]. It is based on Newton's work on the speed of sound in air. Taking E as the wall's Young's Modulus, h as the thickness of the wall, R as the inner radius, and ρ is the fluid density, and relating the change in radius to the applied pressure, the wave

speed ($c_0$) can be written as:

$$c_0 = \sqrt{\frac{E.h}{2R.\rho}} \qquad (1\text{-}19)$$

Errors resulting from the thin tube assumption can be compensated by using the Bergel correction [32], which accounts for the thickness through Poisson's ratio ($\upsilon$). The difference between the modified wave speed ($c'$) and the original one ($c_0$) is calculated by Eq. 1-20:

$$\left(\frac{c'}{c_0}\right)^2 = \frac{(2-\gamma)}{[2-2\gamma(1-\upsilon-2\upsilon^2)+\gamma^2(1-\upsilon-\upsilon^2)-2\upsilon^2]} \qquad (1\text{-}20)$$

where γ is the ratio of the wall thickness and tube outer radius. Simplifying this expression and incorporating it into Eq. 1-19, the modified wave speed ($c'$) becomes as in Eq. 1-21:

$$c' = \sqrt{\frac{E.h}{2R.\rho(1-\upsilon^2)}} \quad . \qquad (1\text{-}21)$$

## 1.7 Numerical Modeling

The numerical setup used for this three-dimensional fluid structure interaction (FSI) study was based on a tube with an internal diameter of 4 mm and a wall thickness of 0.12 mm as shown in Figure 1-9. The length of the model was set as 100 times as long as the internal radius of the tube to be long enough as per the Moens−Korteweg equation's condition. The vessel wall was considered as elastic with a density of 1075 kg/m$^3$, a Poisson's ratio of 0.45, and an initial Young's modulus (E) of 3 MPa. These values are well representative of a blood vessel's physiological state.

Interaction between blood and arterial wall is the main mechanism for propagation of pressure wave from the heart to peripheral vessels. To investigate the coupling between blood dynamic and artery, the blood flow is simulated as an quasi incompressible Newtonian fluid [16]. This assumption has been adapted by different authors to study blood

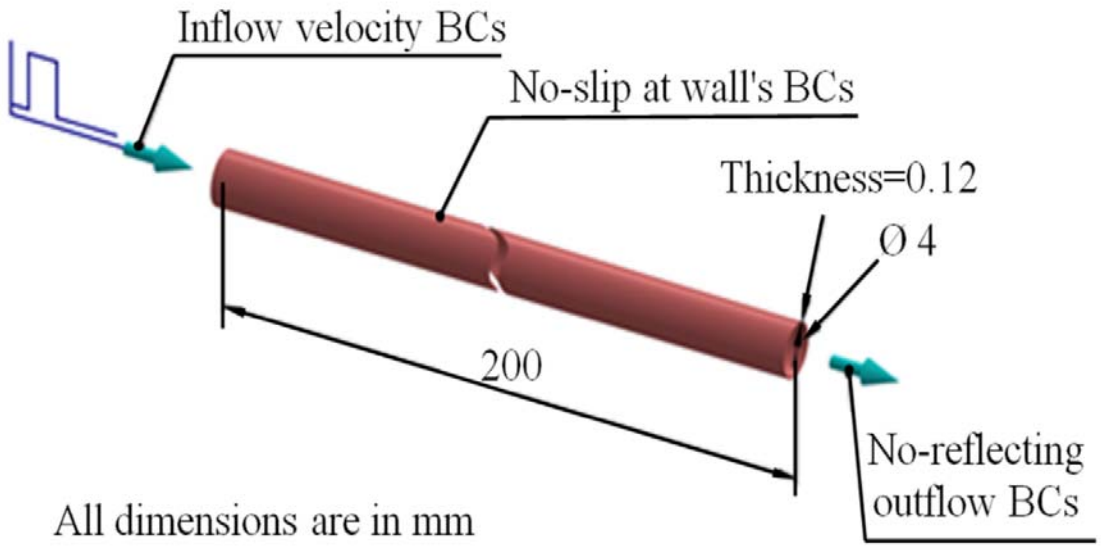


Figure 1-9 The long elastic tube model and boundary conditions

flow in internal carotid artery [33]. Studies conducted by Gupta [34] and Fan [35] have been carried out to investigate the flow field in the carotid artery considering fluid-structure interaction and the comparison between Newtonian and Non-Newtonian fluid. Fan et al. [35] suggest that the flow behaviors obtained by the Non-Newtonian model had no difference when compared with the flow characterizations obtained by the Newtonian model. However, the difference between Newtonian and Non-Newtonian simulation mainly appears in the region of low shear rate and flow recirculation zones. Thus, the blood material was modeled with a quasi incompressible Newtonian equation of state (EOS) which related the density of the blood $\rho$ to the external pressure $P$ and the sound speed $c$ according to Eq. 1-22:

$$\rho = \rho_o + \frac{P}{c} \qquad (1\text{-}22)$$

where $\rho_o$ is the initial blood density. This constitutive material law gives slight compressibility to the blood, which improves the stability and convergence of our computation. Thus, the higher the sound speed the higher the incompressibility of the fluid.

The initial blood density $\rho_o$ was set to 1000 kg/m$^3$ and a dynamic viscosity of 0.001 Pa.s. The sound speed $c_o$ was set to 60 m/s according to a separate study where a range of sound speeds were tested, ranging from 15 m/s to the real value of 1460 m/s. It was found that a sound speed of 60 m/s provided reasonable results and incurred less computational cost. Higher values yielded similar accuracy, but with relatively high computational cost. Lower values such as 15 m/s led to underestimation in the results. We thus concluded that a value of 60 m/s was practical for simulating vascular biomechanical problems.

From Eq. 1-23, it can be seen that the bulk modulus $K$ of the blood can differ by more than $10^3$ more than the arterial wall's Young's modulus ($E$). Materials with elastic modulus differ by $10^3$ or more is not practicable for the FSI study with the current available modeling techniques as noted by Fukui et al. [18].

$$K = \rho {c_o}^2 \qquad (1\text{-}23)$$

A three-dimensional, two-ways coupled simulations of pulse wave propagation were performed using the coupled Eulerian- Lagrangian (CEL) explicit solver of Abaqus® 6.13 (Simulia, RI, USA) [36]. The Lagrangian solid elements were imposed inside the Eulerian elements, and the void elements were added to the outer surface of the Lagrangian element so that the deflected artery walls were always surrounded by Eulerian mesh during the dynamic analysis as shown in Figure 1-10. The problem was set up with 141400 linear hexahedra elements assigned for the fluid and 44800 linear hexahedra elements assigned for the artery, with four layers of elements through the radial thickness. The elements' thickness along the longitudinal direction was 1 mm. All translational degrees of freedom constraints were applied on the inlet and exit sections of the vessel wall. A single rectangular pulse of 1 m/s over a period of 2 ms (Reynolds number = 4000) as shown in Figure 1-11 was applied at the tube inlet to serve as the driving force to produce a propagating wave. A no-slip FSI was defined between the wall and the fluid. A non-reflecting boundary condition was pointed at the tube outlet to reduce the wave reflection due to the truncation of the computational domain; see Eq. 1-24 and Eq. 1-25.

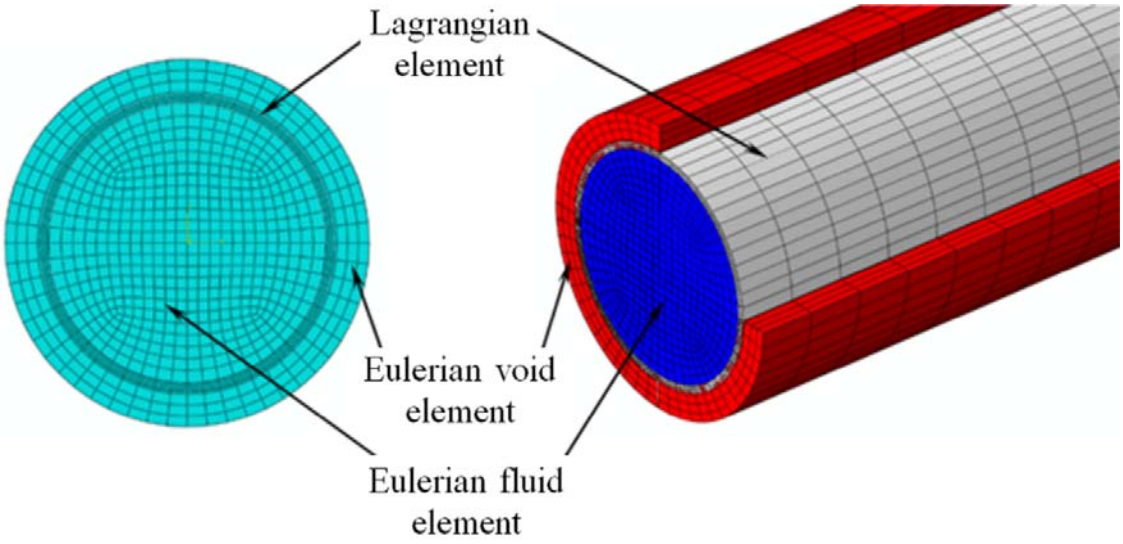


Figure 1-10 Meshed parts of the model

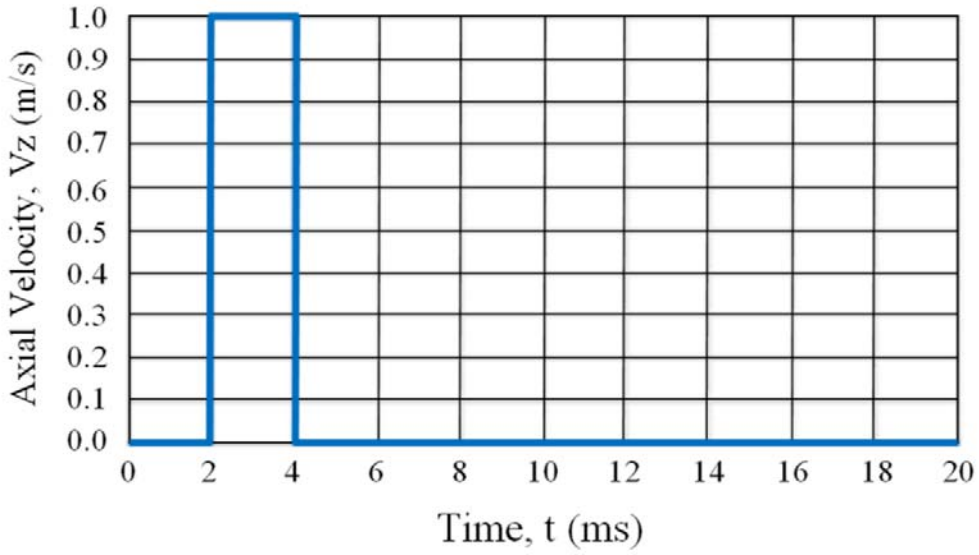


Figure 1-11 Inlet boundary conditions, a velocity pulse in the axial direction

Grote and Keller [37] [38] derived two sets of non-reflecting boundary conditions for the wave equation:

$$B_1 \emptyset + \frac{1}{R}\sum_{n=1}^{\infty}\sum_{m=-n}^{n} e_n \cdot z_{nm}(t)\, Y_{nm}(\theta,\varphi) = 0 \qquad (1\text{-}24)$$

$$B_2 \emptyset + \frac{1}{R}\sum_{n=2}^{\infty}\sum_{m=-n}^{n} \hat{e}_n \cdot z_{nm}(t)\, Y_{nm}(\theta,\varphi) = 0 \qquad (1\text{-}25)$$

where $\phi$ *(x,t)* is the solution to the scalar wave equation, *R* is the radius of a spherical artificial boundary $\Gamma$, $Y_{nm}$ are spherical harmonics, $e_n$, $\hat{e}_n$, are vectors of coefficients, and $z_{nm}(t)$ are solutions to a first-order system of ordinary differential equations driven by the radial harmonics $\phi_{nm} = (\phi, Y_n)\Gamma$. The summation over the series in Eq. 1-24 and Eq. 1-25 may be considered as extensions of the local $B_1$ and $B_2$ operators, respectively, of Bayliss et al. [39]. In computation, the sum over n in Eq. 1-24 and Eq. 1-25 is truncated at an arbitrary value $N \geqq 1$ and $N \geqq 2$, respectively. Both boundary conditions were exact for modes $n \leqq N$.

## 1.8 Wave Propagation

The simulation ran with a 20-ms explicit step-time for a Young's moduli range of 3, 2, 1, 0.5, and 0.1 MPa assigned to the tube material. Using a Dell computer with an Intel® Xeon® CPU running at 2.8 GHz with 12 processors and 24 GB RAM, it took approximately 13 h to complete each calculation. Figure 1-12 shows the radial disturbance of the tube wall due to wave propagation in three different time frames.

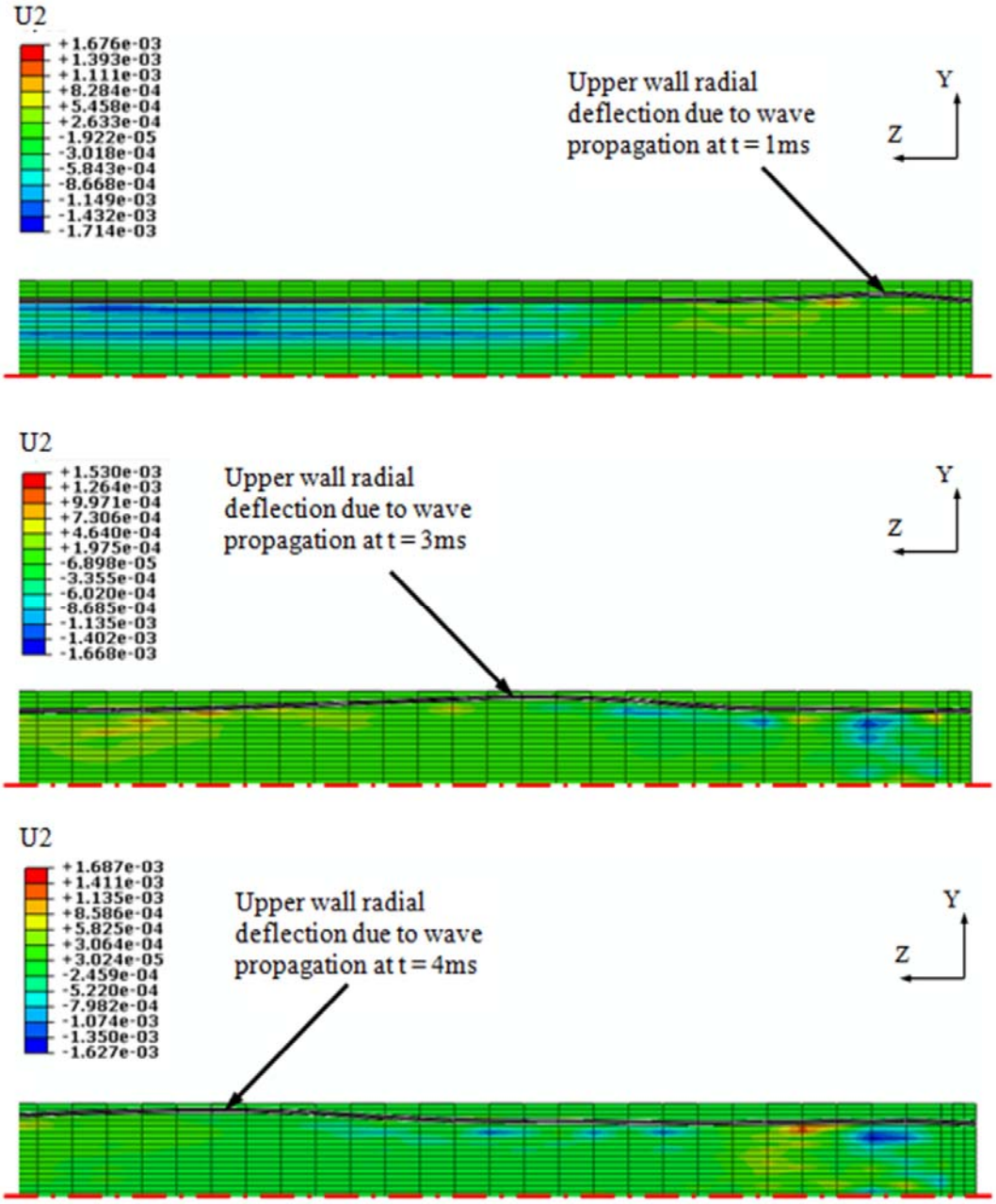


Figure 1-12 : Three different time frames of the radial disturbance of the tube wall due to wave propagation. The displacement of the structure has been magnified by factor of 5. The unit of the scale is mm.

## 1.9 Velocity Waveforms

Figure 1-13 shows the velocity waveforms at different locations along the tube center line, typically at distances 70, 100, and 130 mm from the tube inlet. The waveforms were plotted from the axial velocity component (Vz). The fluctuations of the velocity curve are a result of FSI. The peaks of the waveforms decreased with simulation time and shifted in the flow direction because of the damping effect.

## 1.10 Pulse Wave Velocity Assessment

Two different methods were used to assist the PWV: foot-to-foot measuring of velocity waveforms and slope of the regression line of the wall radial-deflection wave peaks throughout a contour plot.

### 1.10.1 Foot-to-foot Velocity Waveform Method

The PWV was calculated from the time delay of each waveform relative to its preceding waveform. The waveforms were plotted for equal-spaced intervals along the tube center line. To measure the time interval between two sites, we used the foot-to-foot method [40]. As shown in Figure 1-14, a best fit straight line was fitted to the velocity ascending points between 20% and 80% of the maximum. The pulse arrival time was defined as the point where the line intersected the baseline. The pulse arrival time was determined for two progressive waveforms. PWV was calculated from the distance between the two positions [41], where the axial velocity was plotted, divided by the difference in arrival time (Δt)

$$PWV = \frac{l}{\Delta t}. \qquad (1\text{-}26)$$

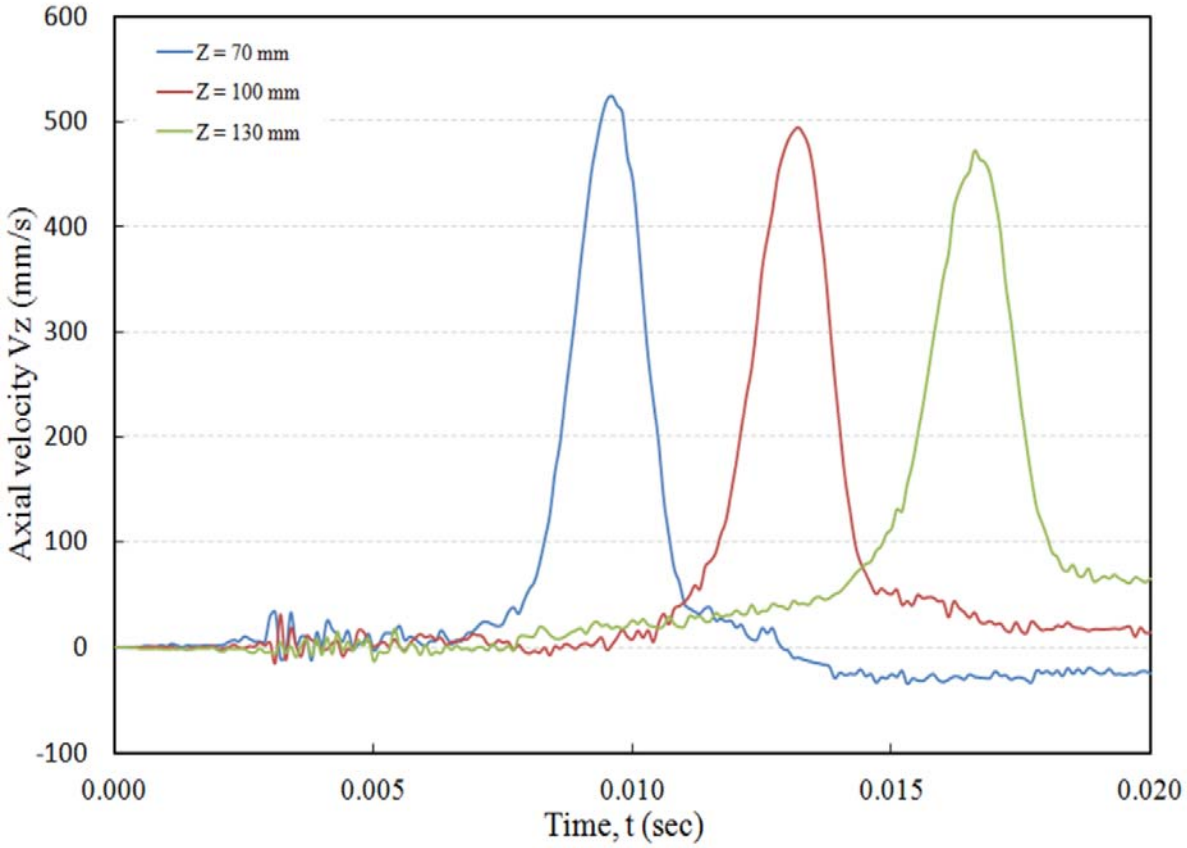


Figure 1-13 Axial velocity waveforms at different locations along the tube center line for artery with Young's modulus of 3.0 MPa.

We take the sites at a distances 70, 100 and 130 mm from the tube inlet to be far away from the tube ends where a wave reflections expected due to fixed boundary conditions at those ends.

### 1.10.2 Slope of Regression Line of Wall Radial-deflection Wave Peaks

The wall radial deflection at equally spaced locations along the tube center line were plotted against time and are shown as a 3D mesh plot in Figure 1-15-a where the peaks of the forward waves are shown. Figure 1-15-b shows the contour plot of the wall radial deflection against time and axial locations. The color coding clearly shows the slope of the waves' peaks through the forward direction. The slope of the regression line represents the value of the PWV. Both methods gave coincident results for the PWV.

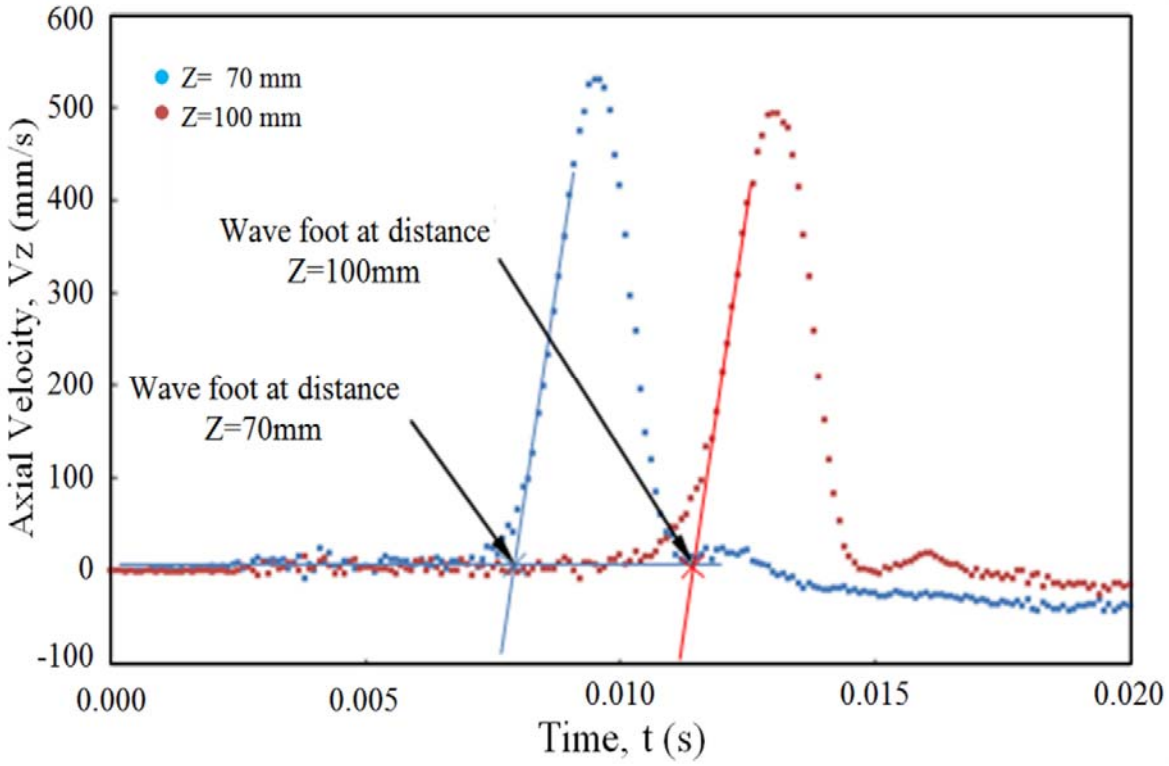


Figure 1-14 Arrival time for two progressive waveforms indicated by foot-to-foot method.

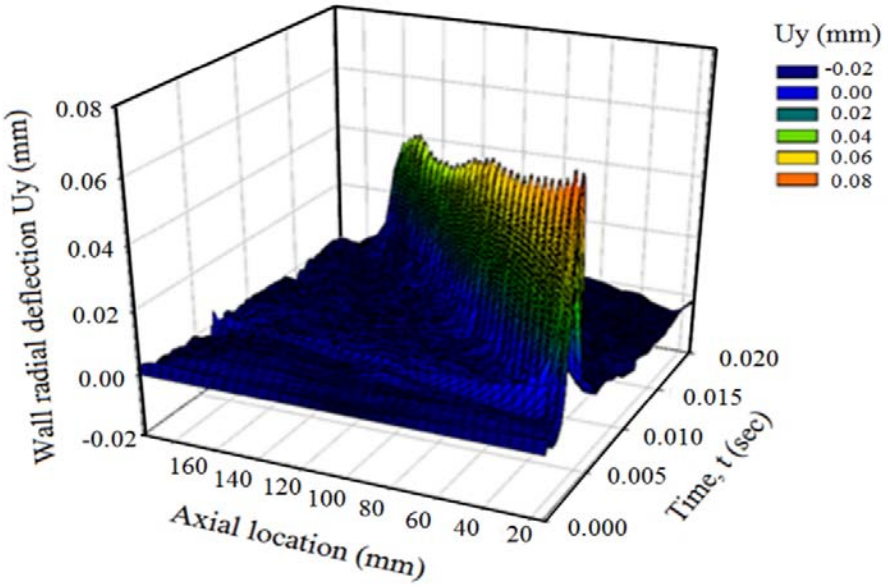


(a) 3D mesh plot

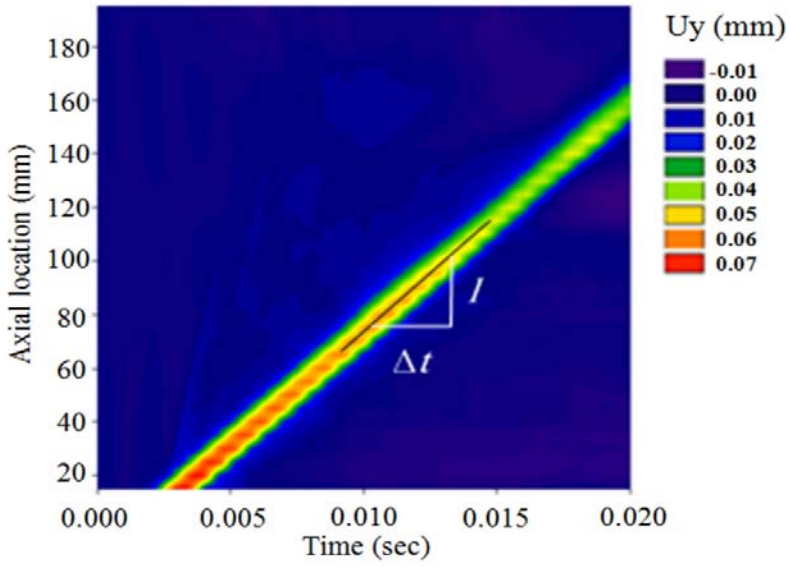


(b) 2D contour plot

Figure 1-15 Model with Young's modulus, E = 3.0 MPa: (a) 3D mesh plot of the wall radial deflection against temporal and spatial coordinates. It shows the peaks of the forward waves. (b) 2D contour plot of the wall radial deflection. The slope of the peaks regression line indicates the PWV.

## 1.11 Validation of Numerical Simulation

### 1.11.1 Validation with the Idealized Theory

The obtained results were plotted with the values calculated from the modified Moens−Korteweg equation, Eq. 1-21, as well as the results obtained by ANSYS-CFX and LS-DYNA as shown in Figure 1-16. These results were computed for different Young's moduli for the tube material. The obtained results corresponded well with the idealized theory with underestimation depending on the value of a wall's Young's modulus.

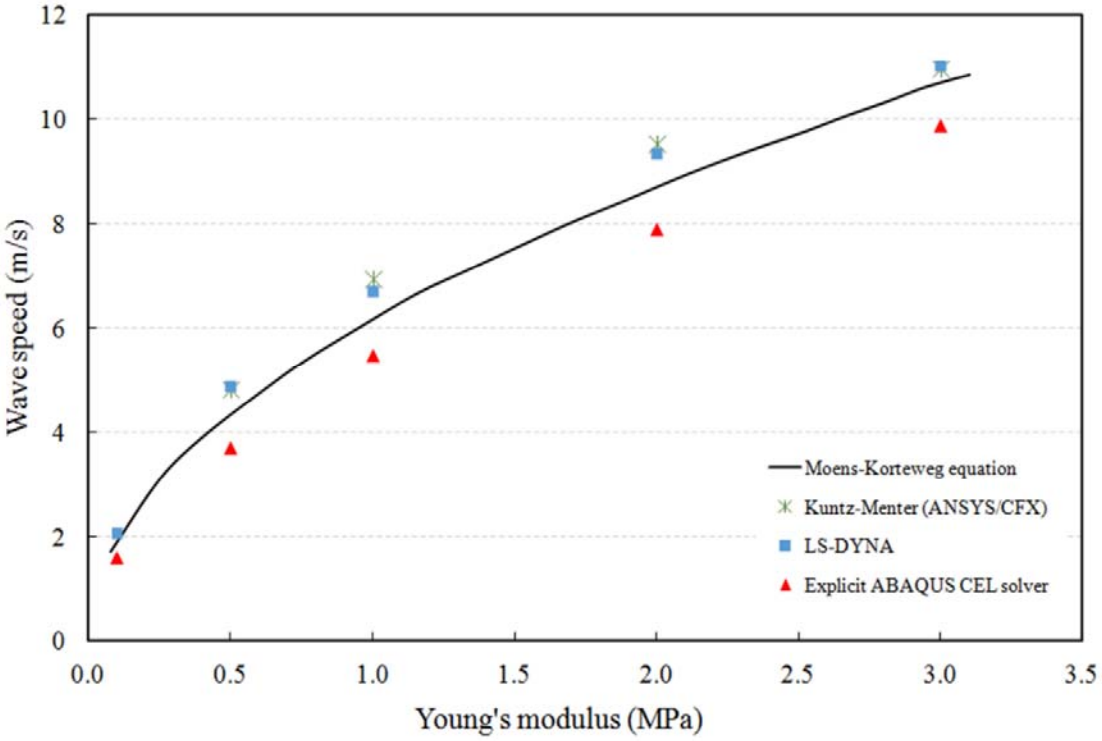


Figure 1-16 PWV as function of young's modulus: comparison of numerical results and idealized theory.

### 1.11.2 Validation with in Vivo Measurements of PWV

Figure 1-17 shows the effect of ageing on elastic properties of arteries where incremental Young's modulus plotted against age for normal human aorta at a pressure of 100 mm Hg

according to the work of Caro et al. [42]. We use our approach to model the PWV corresponding to each age interval using those values for Young's modulus. The obtained results are plotted with in vivo PWV values obtained from literature [43] as shown in Figure 1-18. The graph shows that the obtained results corresponded well with the normal values for in vivo PWV.

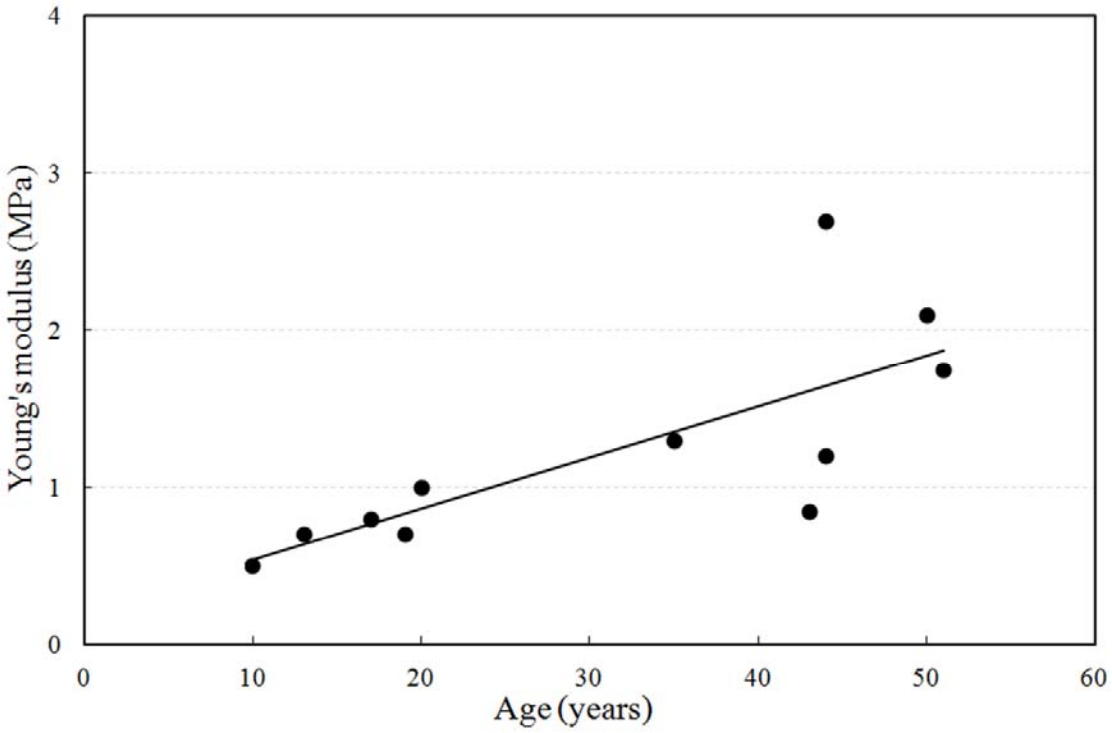


Figure 1-17 Effect of ageing on elastic properties of arteries, incremental Young's modulus plotted against age for normal human aorta at a pressure of 100 mm Hg [37].

## 1.12 Discussion

Figure 1-16 shows that the PWV is proportional to the wall stiffness. The obtained results are slightly underestimated compared to the basic theory. The underestimation is attributed to two basic reasons. First, waves were reflected because of the finite tube length and fixed boundary conditions, which pointed at the tube ends. Second, the scaling down of the speed of sound added some compressibility to the fluid resulting in significant damping, which

played a role in slowing the wave propagation speed. The underestimation difference increased with increases in wall stiffness. Therefore, we kept underestimation at a minimum of 7% corresponding to Young's modulus E = 3.0 MPa by using a "long enough"

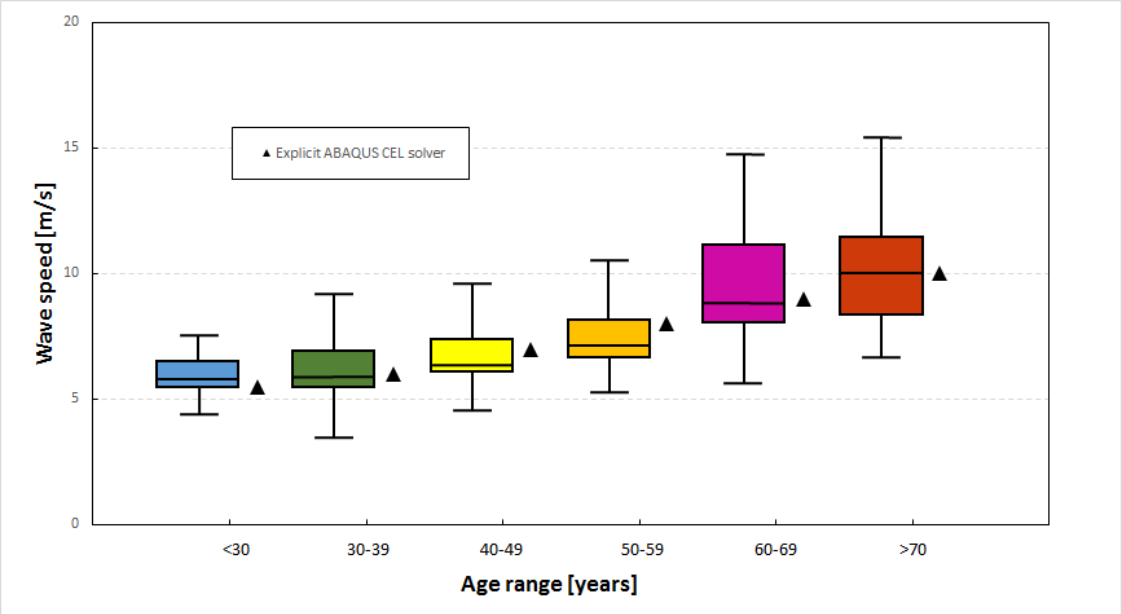


Figure 1-18 Normal values for PWV (average according to age (1455 subjects), boxes contain 50% of the data and bars contain the remainder; horizontal lines indicate medians) [38] plotted with the corresponding values obtained from our approach.

tube length with a tube length to radius ratio, l/r, of 100 and by applying non-reflecting boundary conditions at the tube outlet. Scaling down the speed of sound to 60 m/s provided a reasonable computational cost without affecting the accuracy of the obtained results. However, the results obtained from other models such as that of Fukui et al. [18] and Shahmirzadi et al. [41], [17], who implemented their work with the commercial code Radioss (Altair Engineering) and ABAQUS (Simulia, USA), respectively, also show underestimation in most cases.

## 1.13 Conclusion

In this study, a basic computational scheme for a strongly coupled FSI in an elastic artery was developed and validated with basic theory. Qualitative agreement was obtained indicating that this computational method for PWV analysis is accurate enough to evaluate its value with accepted accuracy. The scaling down of sound speed has a significant effect on results convergence and computation cost, and we conclude that a value of 60 m/s is reasonable enough for solving vascular biomechanical problems. In other side, the PWV values obtained from our new approach are corresponded well with in vivo reference values published in the literatures [37], [38].

# Chapter 2

# SPH Method Applied to Membrane Inflation

Partly adapted from postprint version of:

**Experimental and numerical investigation for membrane deployment using SPH and ALE formulations**

Essam Al-Bahkali[1], Hisham Elkenani[1], and Mhamed Souli[2]

[1]Department of Mechanical Engineering, King Saud University, P.O. Box 800, Riyadh 11421, Saudi Arabia

[2]Laboratoire de Mécanique de Lille, UMR CNRS 8107, Villeneuve-d'Ascq, France

Published in:
Computer Modeling in Engineering & Sciences
Volume 104, Issue 5, Pages 405-424, 2015.

In this chapter, we present experimental and numerical investigation for membrane deployment using SPH and ALE formulations. Simulation of airbag and membrane deployment under pressurized gas problems becomes more and more the focus of computational engineering, where FEM (Finite Element Methods) for structural mechanics and Finite Volume for CFD are dominant. New formulations have been developed for FSI applications using mesh free methods as SPH method, (Smooth Particle Hydrodynamic). Up to these days very little has been done to compare different methods and assess which one would be more suitable. For small deformation, FEM Lagrangian formulation can solve structure interface and material boundary accurately, the main limitation of the formulation is high mesh distortion for large deformation and moving structure. One of the commonly used approach to solve these problems is the ALE formulation which has been used with success in the simulation of FSI (Fluid Structure Interaction) with large structure motion such as sloshing fuel tank in automotive industry and bird impact in aeronautic industry. For some applications, including bird impact and high velocity impact problems, engineers have switched from ALE to SPH method to reduce CPU time and save memory allocation.

The mathematical and numerical implementation of the ALE and SPH formulations are, also, described in this chapter. From different simulation, it has been observed that for the SPH method to provide similar results as ALE or Lagrangian formulations, the SPH meshing, or SPH spacing particles needs to be finer than the ALE mesh.

To validate the statement, we perform a simulation of membrane deployment generated by high pressurized gas. For this simple problem, the particle spacing of SPH method needs to be at least two times finer than ALE mesh. A contact algorithm is performed at the FSI for both SPH and ALE formulations.

## 2.1 Introduction

Theoretical and experimental analysis of fluid structure interaction for airbag and membrane deployment have been considered by several researchers over the past decades, using uniform pressure methods. The uniform pressure formulation does not consider the

gas simulation, and no CFD modeling is involved. Experiments have shown, that the resulting flow is quite complex, involving several physical phenomena as damping effects. Numerical simulation using appropriate hydrodynamic equations for the gas, helps to describe these phenomena, and also minimize the number of tests required that are very costly. Once simulations are validated by test results, it can be used as design tool for the improvement of the system structure involved. Initially FEM Lagrangian were used to simulate these problems, unfortunately classical Lagrangian methods cannot resolve large mesh distortion, runs are stopped before reaching termination time, due to negative Jacobian in highly distorted element. ALE multi-material description of motion developed in Aquelet, Souli and Olovson [44] can be used as an alternative for the simulation of high explosive phenomena. The ALE formulations have been developed to overcome the difficulties due to large mesh distortion. For some applications, including underwater explosions and their impact on the surrounding structure, engineers have switched from ALE to SPH method to reduce CPU time and save memory allocation.

It is well known from previous papers, see Ozdemir, Souli and Fahjan [45] that the classical FEM Lagrangian method is not suitable for most of the FSI problems due to high mesh distortion in the fluid domain. In many applications the ALE formulation has been the only alternative to solve fluid structure interaction for engineering problems. For the last decade, SPH method has been usefully used for engineering problems to simulate high velocity impact problems, high explosive detonation in soil, underwater explosion phenomena, and bird strike in aerospace industry. SPH is a mesh free Lagrangian description of motion, that can provide many advantages in fluid mechanics and also for modeling large deformation in solid mechanics. Unlike ALE method, and because of the absence of the mesh, SPH method suffers from a lack of consistency that can lead to poor accuracy.

In the literature there are different formulations of meshless methods, the Meshless Local Petrov-Galerkin Method for solving the bending problem of a thin, see Han and Atluri [46] and Shuyao and Atluri [47] and also Meshless Finite Volume Method developed for solving elasto-static, see Alturi, Han, and Rajendran [48]. In Meshless Local Petrov-Galerkin Method mixed approach, both the strains as well as displacements are

interpolated, at randomly distributed points in the domain, through local meshless interpolation schemes such as the movingleast squares or radial basis functions.

In this chapter, devoted to ALE and SPH formulations for fluid structure interaction problems, the mathematical and numerical implementation of the ALE and SPH formulations are described. From different simulation, it has been observed that for the SPH method to provide similar results as ALE formulation, the SPH meshing, or SPH spacing particles needs to be finer than the ALE mesh. To validate the statement, we perform a simulation of a membrane deployment generated by pressurized gas. For this problem, the particle spacing of SPH method needs to be at least two times finer than ALE mesh. A contact algorithm is performed at the fluid structure interface for both SPH and ALE formulations.

In Section 2.2, the governing equations of the ALE formulation are described. In this section, we discuss the advection algorithms used to solve mass, momentum and energy conservation in the multi-material formulation. Section 2.3 describes the SPH formulation, unlike ALE formulation which based of the Galerkin approach, SPH is a collocation method. The last section is devoted to numerical simulation of a membrane deployment under high pressurized gas, using both ALE and SPH methods. The numerical results will be compared to experimental data.

## 2.2 ALE Formulation

Fluid problems, in which interfaces between different materials (gas and ambient air) are present, are more easily modeled by using a Lagrangian mesh. However, if an analysis for complex tank geometry is required, the distortion of the Lagrangian mesh makes such a method difficult to use many re-meshing steps are necessary for the calculation to continue. Another method to use is the Eulerian formulation. This change from a Lagrangian to an Eulerian formulation, however, introduces two problems. The first problem is the interface tracking [49] and the second problem is the advection phase or advection of fluid material across element boundaries.

To solve these problems, an explicit finite element method for the Lagrangian phase and a finite volume method (flux method) for the advection phase are used. We can refer to several explicit codes such as Pronto, Dyna3D and LS-DYNA®; see [50] for a full description of the explicit finite element method. The advection phase has been developed for extending the range of applications that cannot be used with the Lagrangian formulation. Current applications include sloshing involving a 'free surface', and high velocity impact problems where the target is modeled as a fluid material, thus providing a more realistic representation of the impact event by capturing large deformations.

An ALE formulation contains both pure Lagrangian and pure Eulerian formulations. The pure Lagrangian description is the approach that: the mesh moves with the material, making it easy to track interfaces and to apply boundary conditions. Using an Eulerian description, the mesh remains fixed while the material passes through it. Interfaces and boundary conditions are difficult to track using this approach; however, mesh distortion is not a problem because the mesh never changes. In solid mechanics a pure Eulerian formulation it is not useful because it can handle only a single material in an element, while an ALE formulation is assumed to be capable of handling more than one material in an element.

In the ALE description, an arbitrary referential coordinate is introduced in addition to the Lagrangian and Eulerian coordinates. The material derivative with respect to the reference coordinate can be described in Eq. 1.1. Thus substituting the relationship between the material time derivative and the reference configuration time derivative derives the ALE equations.

$$\frac{\partial f(X_i,t)}{\partial t} = \frac{\partial f(x_i,t)}{\partial t} + w_i \frac{\partial f(x_i,t)}{\partial x_i} \tag{2-1}$$

where $X_i$ is the Lagrangian coordinate, $x_i$ the Eulerian coordinate, $w_i$ is the relative velocity. Let denote by *v* the velocity of the material and by *u* the velocity of the mesh. In order to simplify the equations we introduce the relative velocity $w = v - u$. Thus the governing equations for the ALE formulation are given by the following conservation Eqs. 2.2 to 2.4:

### 2.2.1 Mass equation.

$$\frac{\partial \rho}{\partial t} = -\rho \frac{\partial v_i}{\partial x_i} - w_i \frac{\partial \rho}{\partial x_i} \tag{2-2}$$

### 2.2.2 Momentum equation.

The strong form of the problem governing Newtonian fluid flow in a fixed domain consists of the governing equations and suitable initial and boundary conditions. The equations governing the fluid problem are the ALE description of the Navier-Stokes equations:

$$\rho \frac{\partial v_i}{\partial t} = \sigma_{ij,j} + \rho b_i - \rho w_i \frac{\partial v_i}{\partial x_j} \tag{2-3}$$

Boundary and initial conditions need to be imposed for the problem to be well posed.

The superscript means prescribed value, $n_i$ is the outward unit normal vector on the boundary, and $\delta_{ij}$ is Kronecker's delta function.

### 2.2.3 Energy equation.

$$\rho \frac{\partial e}{\partial t} = \sigma_{ij} v_{i,j} + \rho b_i v_i - \rho w_j \frac{\partial e}{\partial x_j} \tag{2-4}$$

Note that the Eulerian equations commonly used in fluid mechanics by the CFD community, are derived by assuming that the velocity of the reference configuration is zero and that the relative velocity between the material and the reference configuration is therefore the material velocity. The term in the relative velocity in Eqs. 2.3 and 2.4 is usually referred to as the advective term, and accounts for the transport of the material past the mesh. It is the additional term in the equations that makes solving the ALE equations much more difficult numerically than the Lagrangian equations, where the relative velocity is zero.

In the second phase, the advection phase, transport of mass, internal energy and momentum across cell boundaries are computed; this may be thought of as remapping the displaced mesh at the Lagrangian phase back to its original or arbitrary position.

From a discretization point of view of Eqs. 2.2, 2.3 and 2.4, one point integration is used for efficiency and to eliminate locking,. The zero energy modes are controlled with an hourglass viscosity Benson [51], A shock viscosity, with linear and quadratic terms, is used to resolve the shock wave [52]; a pressure term is added to the pressure in the energy Eq. 2.4. The resolution is advanced in time with the central difference method, which provides a second order accuracy in time using an explicit method in time. For each node, the velocity and displacement are updated as follows:

$$u^{n+1/2} = u^{n-1/2} + \Delta t \,.\, M^{-1} \,.(F_{exl} + F_{int}) \tag{2-5}$$

The multi-material formulation is attractive for solving a broad range of non-linear problems in fluid and solid mechanics, because it allows arbitrary large deformations and enables free surfaces to evolve. The Lagrangian phase of the VOF method is easily implemented in an explicit ALE finite element method. Before advection, special treatment for the partially voided element is needed. For an element that is partially filled, the volume fraction satisfies $V_f \leq 1$ , and the total stress by $\sigma$ is weighed by volume fraction $\sigma_f = \sigma . V_f$ .

In the second phase, the transport of mass, momentum and internal energy across the element boundaries is computed. This phase may be considered as a ‘re-mapping’ phase. The displaced mesh from the Lagrangian phase is remapped into the initial mesh for an Eulerian formulation, or an arbitrary undistorted mesh for an ALE formulation.

In this advection phase, we solve a hyperbolic problem, or a transport problem, where the variables are density, momentum and internal energy per unit volume, where the Donor Cell algorithm, a first order advection method and the Van Leer algorithm, a second order advection method [51] are used. As an example, the equation for mass conservation is:

$$\frac{\partial \rho}{\partial t} + \nabla . (\rho u) = 0 \tag{2-6}$$

It is not the goal of this study to describe the different algorithms used to solve Eq. 2.7. Figure 2-1 describes the two phases for a one step explicit calculation.

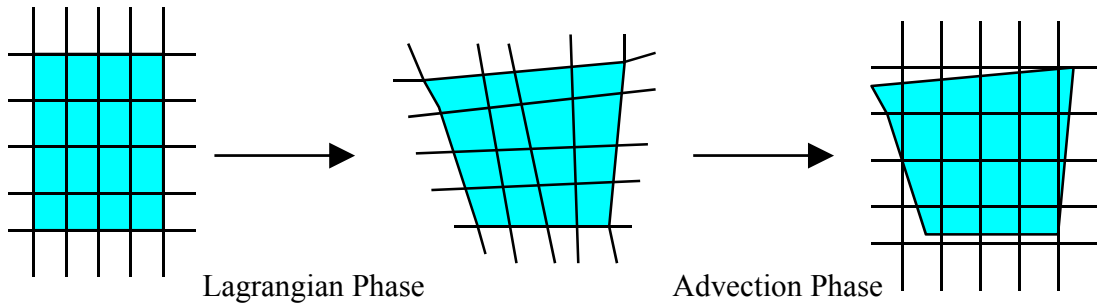


Figure 2-1 - Lagrangian and Advection phases in multi-material ALE formulation

## 2.3 SPH formulation

"SPH provides a fascinating tool that has some of the properties of molecular dynamics while retaining the attributes of the macroscopic equations of continuum mechanics." J. J. Monaghan [53].

The majority of state-of-the-art simulation tools for continuum mechanics relate to meshbased Finite-Volume (FV) or Finite-Element (FE) solvers. Such traditional grid-based numerical methods provide a good predictive accuracy and can be applied to a wide range of engineering problems. However, these approaches have limitations, especially if it comes to applications that involve: large relative motions, multiple interacting rigid structures, multiple phases and continua, complex free surface flows, large deformations, and fragmentation of solids.

Contrary to this, mesh-free methods solve the governing equations without a rigid alignment to grid structures or discrete topologies. That way, many of the above mentioned drawbacks of mesh-based procedures can easily be overcome. Several mesh-free techniques have been developed in the last decades; good summaries are given e.g. in a review paper of Belytschko et al. [54], the PhD thesis of Chaniotis [55] and the book of Liu [6]. Some of the formulations still incorporate grids as necessary ingredients of the

numerical method. On the contrary, Smoothed-Particle-Hydrodynamics (SPH) can be considered a truly mesh-free approach. In SPH, the continuum is descritised by set of finite particles that can arbitrarily move. By using an interpolation technique known as reproducing kernel approximation, field values can be approximated at a certain point as a weighted average over a set of nearby particles.

The method was originally developed in 1977 independently by Lucy [56] and Gingold and Monaghan [57] to study cosmological problems. Since then, it has considerably matured [53], [58], [59] and was successfully used to study problems from a large variety of disciplines. Its highly diverse range of applications has recently been extended to marine, hydraulic, geoenvironmental and geotechnical engineering problems. Published examples include, but are not limited to, general free-surface flows [60], ship dynamics [61], landslide simulations [62], [63] reservoir flushing [64], flood simulations [65] or embankment failures [66], [67].

The SPH method developed originally for solving astrophysics problem has been extended to solid mechanics by Libersky et al. [68] to model problems involving large deformation including high velocity impact. SPH method provides many advantages in modeling severe deformation as compared to classical FEM formulation which suffers from high mesh distortion. The method was first introduced by Lucy [69] and Gingold and Monaghan [70] for gas dynamic problems and for problems where the main concern is a set of discrete physical particles than the continuum media. The method was extended to solve high velocity impact in solid mechanics, CFD applications governed by Navier-Stokes equations and fluid structure interaction problems.

It is well known from previous papers, that SPH method suffers from lack of consistency, that can lead to poor accuracy of motion approximation. Unlike Finite Element, interpolation in SPH method cannot reproduce constant and linear functions.

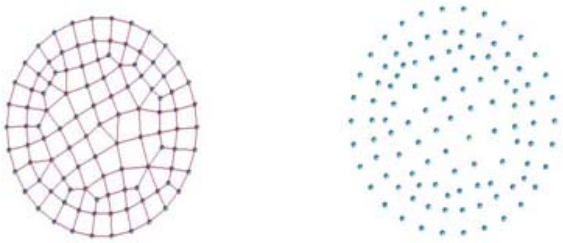

Figure 2-2 FEM model, mesh and nodes (left) and SPH model, particles (right)

A detailed overview of the SPH method is developed by Liu M.B. and Liu G.R. [58] and Violeau [71] where the two steps for representing of function f, an integral interpolation and a kernel approximation are given by:

$$u(x_i) = \int u(y).\delta(x_i - y)dy \tag{2-7}$$

Where the Dirac function satisfies:

$$\delta(x_i - y) = 1, \text{ if } x_i = y \tag{2-8}$$

$$\delta(x_i - y) = 0, \text{ if } x_i \neq y$$

The approximation of the integral function Eq. 2.7 is based on the kernel approximation W, which approximates the Dirac function based on the smoothing length h,

$$W(d,h) = \frac{1}{h^{\alpha}}.\theta\left(\frac{d}{h}\right), \tag{2-9}$$

that represents support domain of the kernel function, see Figure 2-3.

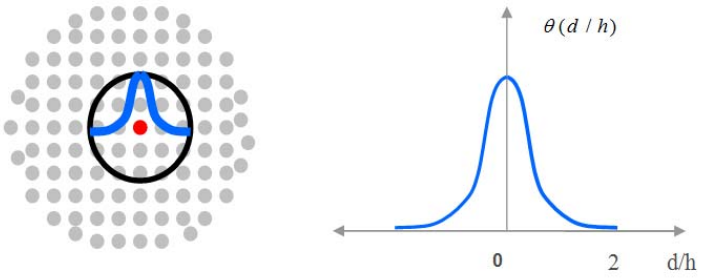


Figure 2-3 Kernel Function and its support domain for a 2D function

So that Eq. 2.7 becomes,

$$< u(x_i) >= \int u(y).W(\|x - y\|, h)dy \tag{2-10}$$

Taking in consideration de support domain of the kernel function, the SPH approximation of a particle $x_i$ is obtained discretizing the integral into a sum over the particles that are within the kernel support domain as it is shown in

Figure 2-3.

$$u_{sph}(x_i) = \sum_{j \in D_i} \omega_j . u_j . W(\|x_i - x_j\|, h), \tag{2-11}$$

where the weight $\omega_j = \frac{m_j}{\rho_j}$ is the volume of the particle.

Integrating by part Eqs. 2.3 and 2.4 and considering the properties of the SPH interpolation and that $\nabla(u) = u.\nabla(1) - 1.\nabla(u)$, the SPH approximation for the gradient operator of a function is given by,

$$\nabla u_{sph}(x_i) = \sum_{j \in D_i} \omega_j . (u_i - u_j) . \nabla W(\|x_i - x_j\|, h), \tag{2-12}$$

Considering that $\frac{\nabla(P)}{\rho} = \frac{P}{\rho^2}\nabla(\rho) + \nabla\left(\frac{P}{\rho}\right)$, applying the SPH interpolation on Navier-Stokes equations, one can derive a symmetric SPH formulation for Navier-Stokes equations such that the principle of action and reaction is respected and that the accuracy is improved. Finally, we have the following discretized set of equations:

### 2.3.1 Mass equation.

$$\frac{D\rho_i}{Dt} = \rho_i \sum_{j\in D_i} \omega_j . \left(v_i^\beta - v_j^\beta\right) . \frac{\partial W\left(\left\|x_i - x_j\right\|, h\right)}{\partial x_i^\beta} \tag{2-13}$$

### 2.3.2 Momentum equation.

$$\frac{Dv_i^\alpha}{Dt} = \sum_{j\in D_i} m_j . \left(\frac{\sigma_i^{\alpha\beta}}{\rho_i^2} + \frac{\sigma_j^{\alpha\beta}}{\rho_j^2}\right) . \frac{\partial W\left(\left\|x_i - x_j\right\|, h\right)}{\partial x_i^\beta} + f_{ext} \tag{2-14}$$

### 2.3.3 Energy equation.

$$\frac{De_i}{Dt} = \frac{1}{2}\sum_{j\in D_i} m_j . \left(\frac{P_i}{\rho_i^2} + \frac{P_j}{\rho_j^2}\right) . \left(v_i^\beta - v_j^\beta\right) \frac{\partial W\left(\left\|x_i - x_j\right\|, h\right)}{\partial x_i^\beta} + \frac{\mu_i}{\rho_i}\varepsilon_i^{\alpha\beta}\varepsilon_i^{\alpha\beta} \tag{2-15}$$

## 2.4 ALE Penalty Coupling Algorithm

Penalty coupling behaves like a spring system and penalty forces are calculated proportionally to the penetration depth and spring stiffness. The head of the spring is attached to the structure or slave node and the tail of the spring is attached to the master node within a fluid element that is intercepted by the structure, as illustrated in Figure 2-4. Similarly to penalty contact algorithm, the coupling force is described by Eq. 2.6:

$$F = k.d \tag{2-16}$$

where $k$ represents the spring stiffness, and $d$ the penetration. The force $F$ in Figure 2-4 is applied to both master and slave nodes in opposite directions to satisfy force equilibrium at the interface coupling, and thus the coupling is consistent with the fluid-structure interface conditions namely the action-reaction principle.

The main difficulty in the coupling problem comes from the evaluation of the stiffness coefficient $k$ in Eq. 2.16. The stiffness value is problem dependent, a good value for the stiffness should reduce energy interface in order to satisfy total energy conservation, and prevent fluid leakage through the structure. The value of the stiffness $k$ is still a research topic for explicit contact-impact algorithms in structural mechanics. In this paper, the stiffness value is similar to the one used in Lagrangian explicit contact algorithms, described in Benson [51]. The value of $k$ is given in term of the bulk modulus $K$ of the fluid element in the coupling containing the slave structure node, the volume $V$ of the fluid element that contains the master fluid node, and the average area $A$ of the structure element connected to the structure node.

$$k = p_f \cdot \frac{K.A^2}{V} \tag{2-17}$$

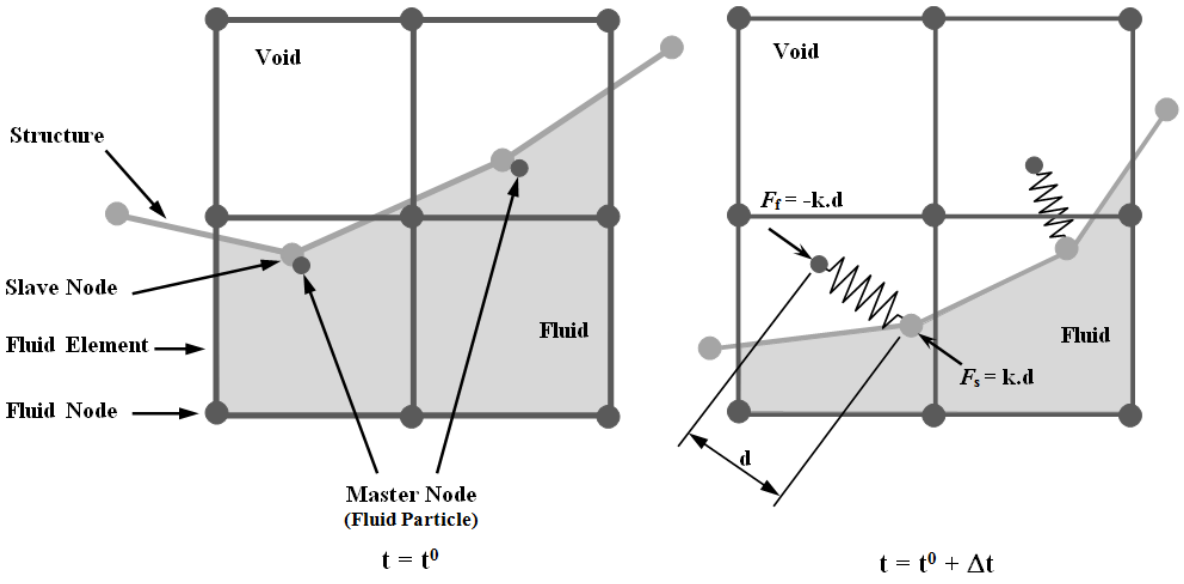


Figure 2-4 Description of Penalty Coupling Algorithm

## 2.5 SPH Contact Algorithm

Several contact methods have been published in litterarture between different structure material parts. Classical implicit and explicit coupling are described in detail in Longatte et al. [72] and Longatte et al. [73], where hydrodynamic forces from the fluid solver are passed to the structure solver for stress and displacement computation. In this study, a coupling method based on contact algorithm is used. Since the coupling method described in this chapter is based on the penalty method for contact algorithms, the contact approach is a good introduction to this method. In contact algorithms, a contact force is computed proportional to the penetration vector, the amount the constraint is violated. In contact algorithms, one surface is designated as a slave surface, and the second as a master surface. The nodes lying on both surfaces are also called slave and master nodes respectively. In an explicit FEM method, contact algorithms compute interface forces due to impact of the slave node on the master node, these forces are applied to the slave and master nodes in contact in order to prevent a node from passing through contact interface. The penalty method imposes a resisting force to the slave node, proportional to its penetration through the master segment, as shown in Figure 2-5 describing the contact process. This force is applied to both the slave node and the nodes of the master segment in opposite directions to satisfy equilibrium.

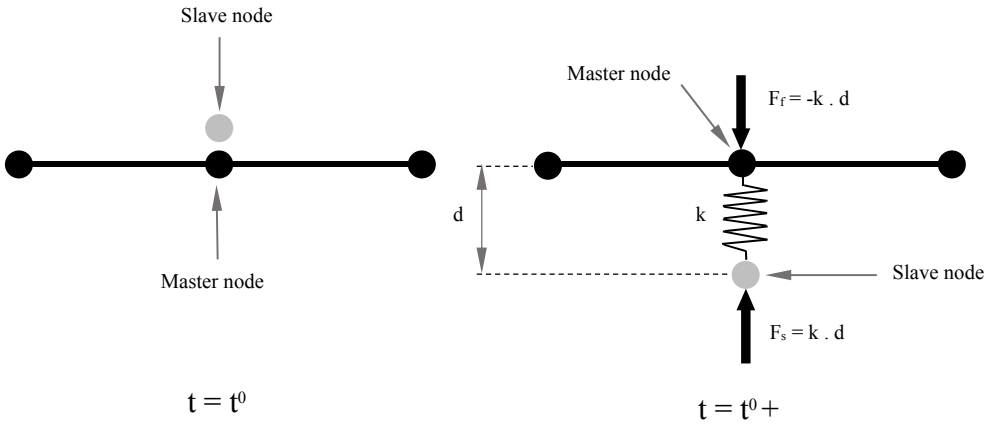


Figure 2-5 Description of Penalty Contact algorithm between slave particle and master structure

## 2.6 Description of the Experimental Setup

Erchiqui et al. [74] experimentally investigated the inflation behavior in a thermoplastic membrane under the combined effects of applied stress and temperature using bubble inflation tests. The results were used to identify the material constants embedded in the constitutive models of the polymeric materials in this work. The polymeric material, acrylonitrile-butadiene-styrene (ABS), was tested under biaxial deformation using the bubble inflation technique. The initial ABS sheet thickness was 1.57 mm. The experimental setup is shown in Figure 2-6.

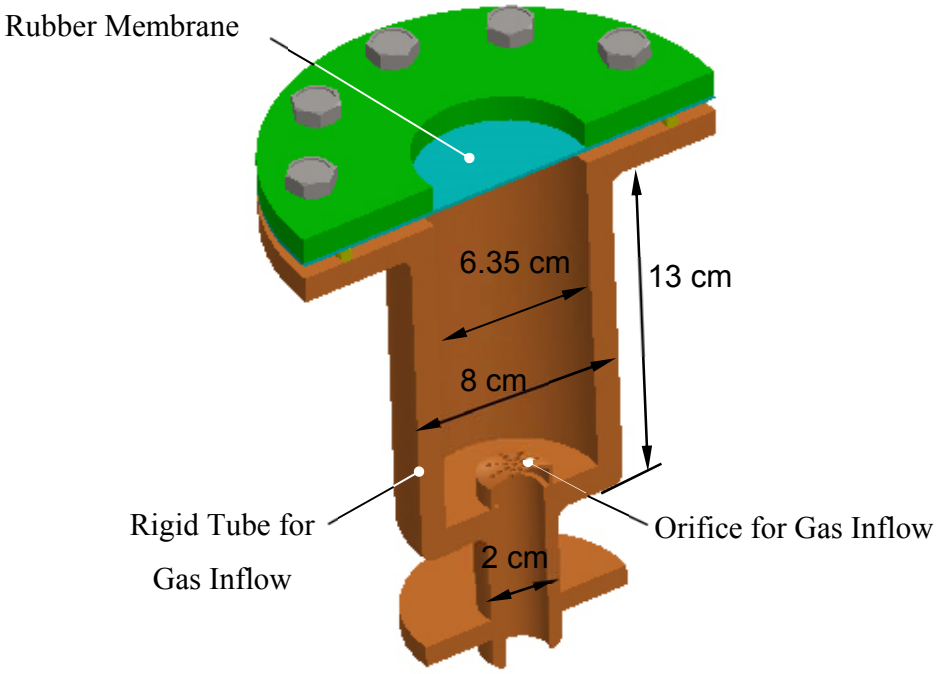


Figure 2-6 Test rig used in the experiment

The circular membranes were mounted between two metal disks containing a circular aperture and subsequently clamped onto a support. The exposed circular area of diameter D = 6.35 cm was heated in an infrared heating chamber to the softening point. When the temperature became uniform over the flat sheet, the circular area was inflated using compressed air under a controlled flow rate. The applied inflation pressure, which was

uniform over the membrane, was measured with a pressure sensor during the testing. The height at the hemispheric pole (or the center of the membrane) and the time were recorded simultaneously using a video camera and a data acquisition system.

## 2.7 Numerical Simulation Using SPH Method

A commercial FE software package was used as a software platform. The next subsections describe the model set up including all simulation approaches used as well as the boundary conditions applied to the model.

### 2.7.1 1. Model and parts' materials properties

The model, as shown in Figure 2-7, consists of four parts, a membrane, fluid domain, sidewall, and a rigid plate acts as a piston. The fluid domain in this case has the property of air. Table 2-1 denotes the details of the property values.

| Material Behaviors | Value, SI units |
|---|---|
| Density, $\rho$ | 1.2047 $kg/m^3$ |
| Viscosity, $\mu$ | 1.8205E-5 $N/m^2 . s$ |
| EOS | $C_0$ = 343.210 m/s, (Us – Up) |

Table 2-1 Properties of air used in the simulation

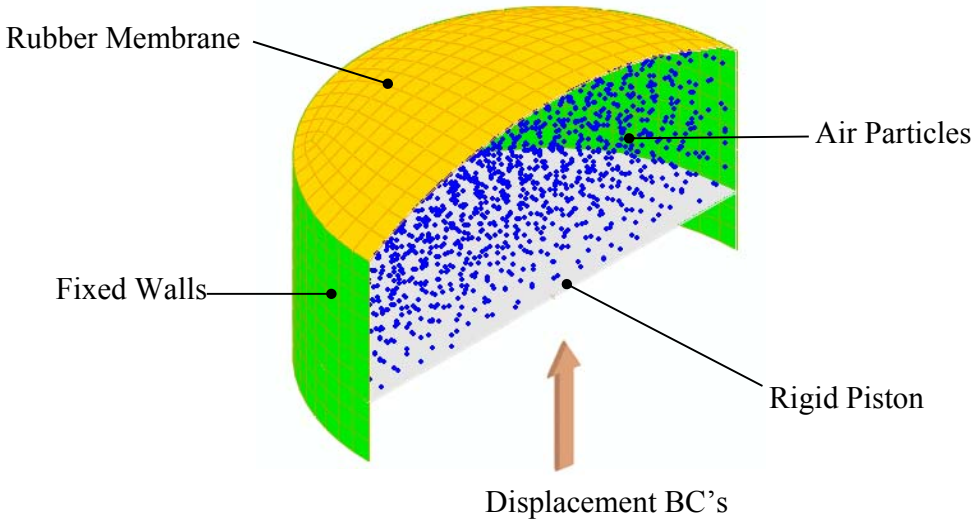


Figure 2-7 The model used for membrane inflation simulation

The membrane is modeled using acrylonitrile-butadiene-styrene (ABS). The material constants for Moony-Rivlin model are $C_{10}$= 105000 Pa and $C_{01}$ = 10500 Pa [25], corresponding to α= 0.1 (α = $C_{01}$/ $C_{10}$). The theoretical material constants are obtained by fitting pressure deformation experimental data with a membrane radius of 0.03175 m and a sheet thickness of 0.00157 m. Figure 2-8 shows fitting curves for various values for α of isotropic hyperelastic model at 143°C. As shown, the value of α=10 is the best fit for the experimental data.

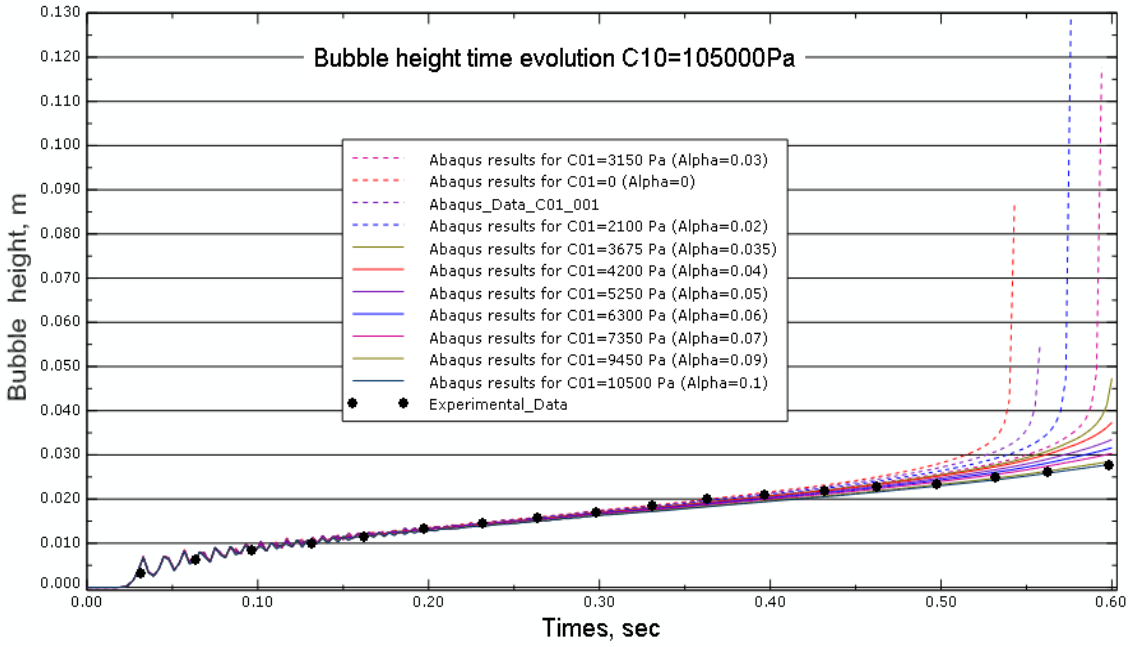


Figure 2-8 Bubble height evolution with various values for α

The value of parameter D1 is submitted as zero, however the analysis platform assumes a default non-zero value for D1 in order to provide some compressibility for the algorithm to work efficiently [36]. This is because the platform has no mechanism for imposing such a constraint at each material calculation point. This default value is $K_0 / \mu_0 = 20$ corresponding to Poisson's ratio of 0.475, where $K_0$ is the initial bulk modulus and $\mu_0$ is the initial shear modulus.

### 2.7.2 Meshing

The membrane is meshed with shell elements. For the air, to ensure uniform distribution for the air particles using SPH method, it initially meshed with solid elements, and then conversion functionality is used to convert the solid element into SPH particles, Figure 2-

9. We can control the number of particles generated per element by specifying the number of particles to be generated per parent element's isoparametric direction [36].

Figure 2-10 shows the internally generated particles per parent element illustrated for three particles per isoparametric direction [36]. In our case, one particle per isoparametric direction is selected and a cubic spline kernel for interpolation is used.

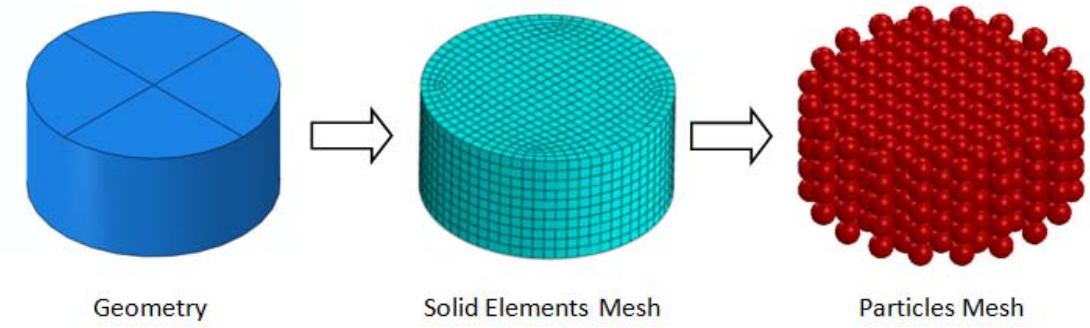


Figure 2-9 Element conversion

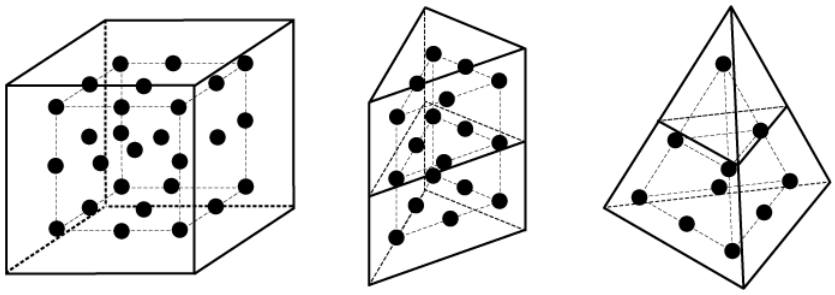

Figure 2-10 Internally generated particles per parent element illustrated for three particles per isoparametric direction (Courtesy of Dassault Systèmes) [36]

We can also specify the time when the conversion of all the elements in the affected element set is to take place. In our case, the conversion time is specified as zero, then the conversion takes place at the beginning of the analysis. The conversion of elements is implemented with keyword code of Abaques® as listed in App. B.

The rigid plate which is acts as a piston is modeled as a rigid body as there is no need to introduce it in the solution. It just acts as inflator's piston. So, no material assigned to it.

| Part Name | Element Type | No of Elements |
|---|---|---|
| Membrane | Linear quadrilateral shell element | 1104 |
| Air | Linear hexahedral solid element (converted into 1-node element) | 34960 |

Table 2-2 Mesh details report

### 2.7.3 Boundary conditions and initial conditions

For the membrane, the boundary conditions of its circumferential is fixed in all degree of freedom (encastre) as well as the side wall. The rigid plate is fixed in all its degree of freedom expect the sliding direction.

A displacement boundary condition is applied to the rigid plate in the sliding direction for a distance equal to 0.027 m, which is sufficient to deliver the volume flow rate necessary to inflate the membrane to the desired height. All the boundary conditions are applied on the model during one step time equal to 0.6 seconds.

### 2.7.4 Interactions

When more than one part involved in a simulation, interaction properties need to be defined. In this case, the interaction property has been defined as frictionless tangential behavior. This property has been applied to all surfaces on the model.

## 2.8 Numerical Results and Observations

A dynamic explicit step with a total duration time equal to 0.6 seconds is trigged to simulate the inflation process. Figure 2-11 shows the initial air particles distribution after the element conversion process at the beginning of the simulation.

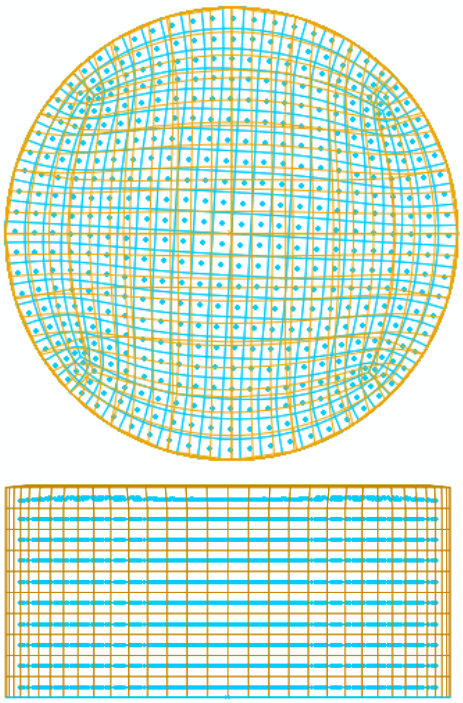

Figure 2-11 Initial air particles distribution at t = 0 s.

Figure 2-12 and Figure 2-13 shows the membrane inflation at 0.3 seconds and at the end of simulation (t = 0.6 seconds) respectively. Animation of the membrane inflation could be viewed at [75].

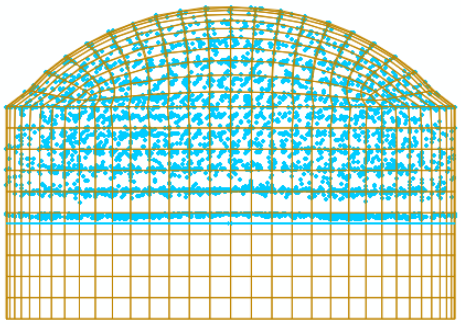

Figure 2-12 Fluid material and structure displacement at t = 0.3 s

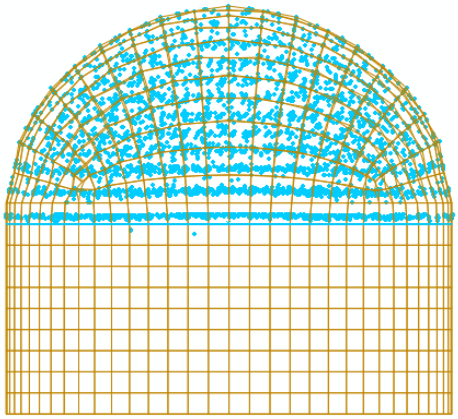

Figure 2-13 Fluid material and structure displacement at t = 0.6 s

Two types of equation of state (EOS) are used to define the air material behavior. The first one is ideal gas EOS which results in excessive noise at the start of simulation due to membrane buckle down. For the real inflation process this phenomenon does not happen. The main reason for this is arises from the fact that the support domain of the kernel is cut by the domain boundary [76]. The bubble height versus time curve is lead as shown in Figure 2-14. The second EOS used is Us-Up which results in more stability at the start of the simulation but, also, with obvious curve leading. As shown in the Figure 2-14, the two assumptions lead to the same bubble height at the end of simulation.

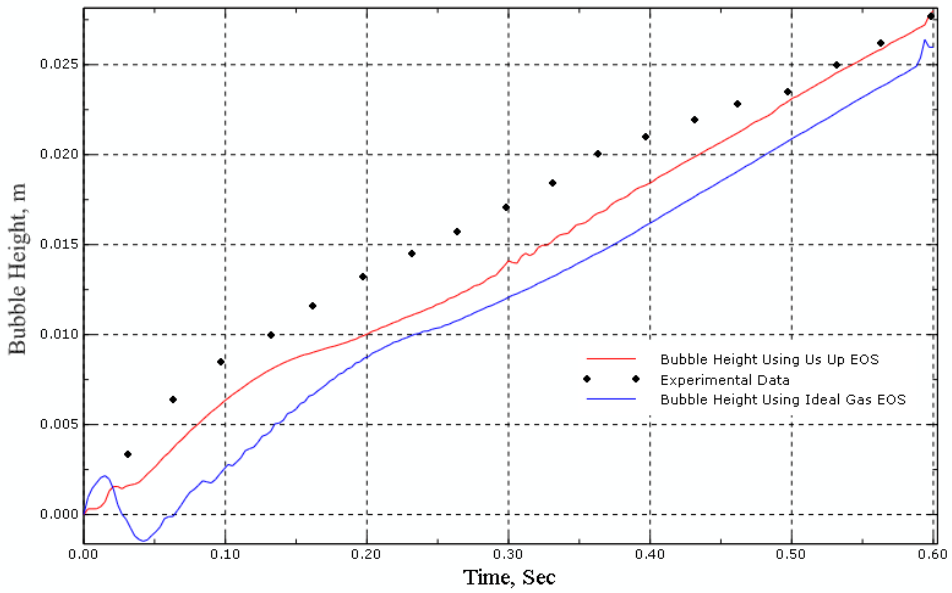


Figure 2-14 - Bubble height time evolution for two different EOS for air comparing with experimental data.

The equation of state (EOS) used to define the air material behavior is Us-Up with the parameter shown in Table 2-1.

As shown in Figure 2-15, the numerical results obtained using higher number of elements are closer to the experimental data than the numerical results obtained with lower number of elements.

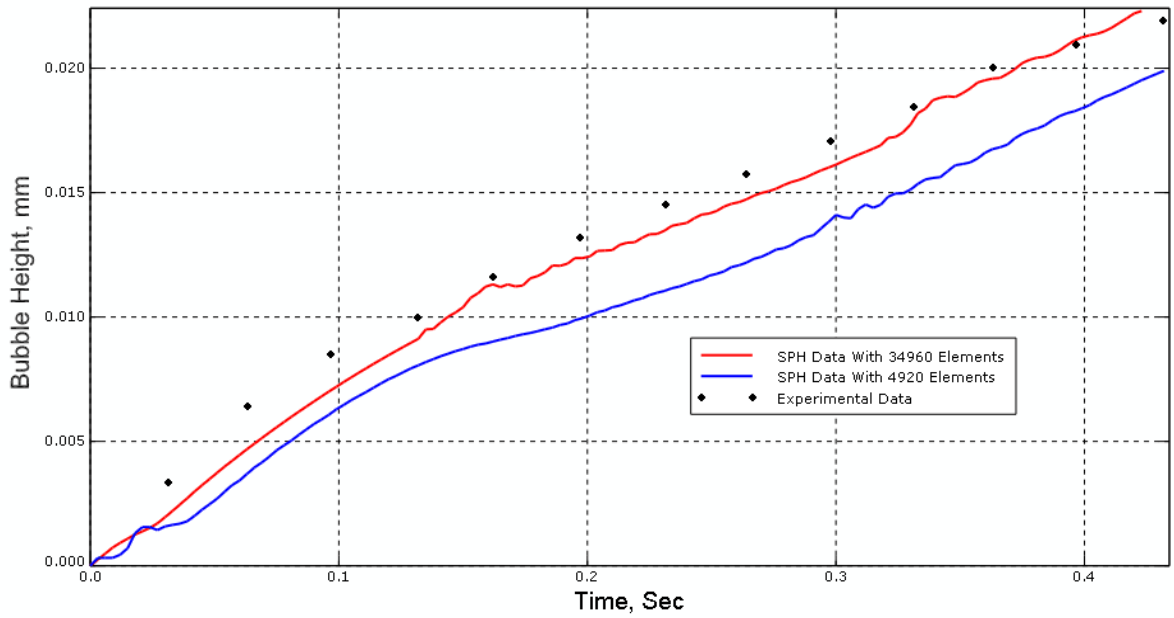


Figure 2-15 Bubble height time evolution with different mesh resolution comparing with experimental data

In the case of SPH method the pressure of the fluid is represented by the equivalent pressure on the particles. Figure 2-16 shows the equivalent pressure curves for a sample of particles represent the air fluid. As shown, the trend of all curves are relatively coincident with experimental pressure data.

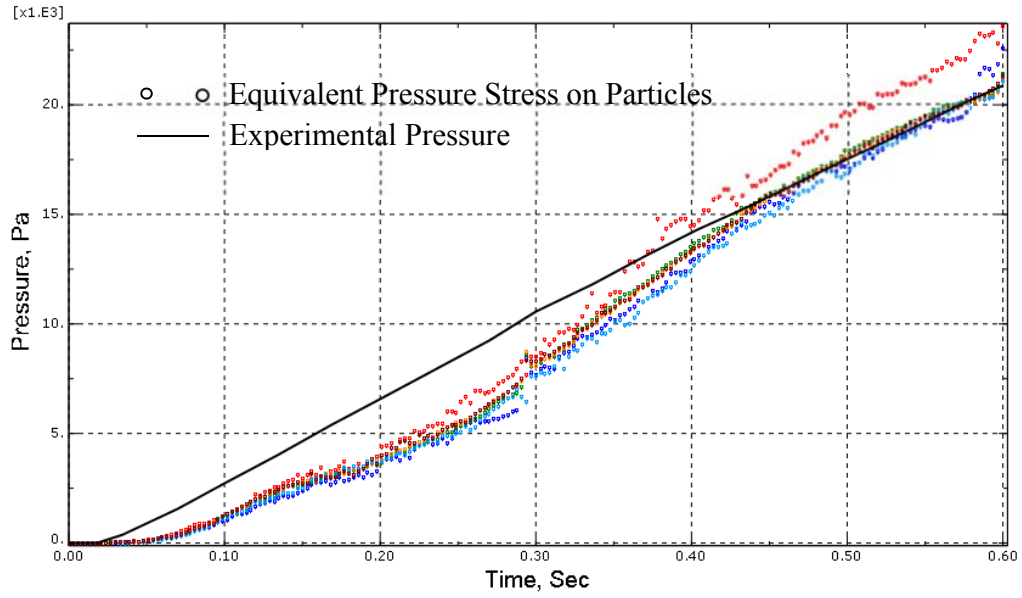


Figure 2-16 Equivalent pressure stress for a sample of elements represent the air

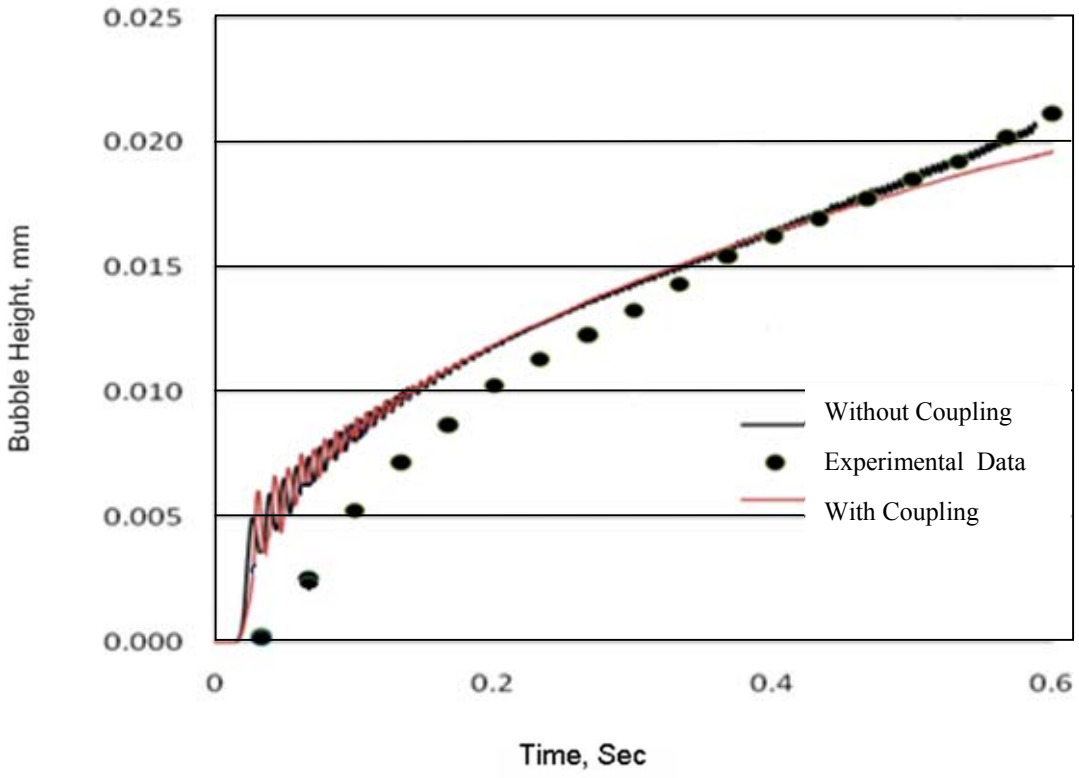


Figure 2-17 Bubble height time evolution for C01=115590 Pa obtained with ALE method

## 2.9 Conclusions

This chapter presents the ALE and SPH methods as well as their limitations for specific problems lime airbag inflation and membrane deployment. Mine explosion, underwater explosion, and bird impact on structures are commonly solved using ALE formulation, in defense industry; some of these problems are solved using SPH method. For the last decade, SPH methods are gaining in accuracy numerical stability, and the use of SPH method is becoming more common in industry for solving fluid structure coupling problems. For instance, in aerospace, where bird impacts on aircraft are very common and cause significant safety threats to commercial and military aircraft. According to Federal American Aviation (FAA) regulations, aircraft should be able to land safely. These applications require a large ALE domain for the coupling between the bird material and the surrounding structure, mainly when the bird is spread all over the space. According to technical reports from engineers in aerospace, ALE formulation is more CPU time consuming and requires more memory allocation that SPH method. In this study, first, we describe both ALE and SPH methods, and we compare numerical results between the two methods using similar mesh size, each ALE element is replaced by an SPH particle at the element center. Using a simple fluid structure interaction problem, it has been observed that using same mesh size for methods, numerical results, displacement and gas pressure using SPH method, provide good correlation with experimental data. For this particular application, without refining the SPH particles, using same number and elements for SPH and ALE, results from SPH method are in good correlation with those from ALE simulation; in terms of displacement, velocity and Von Mises stress on the structure. Since the ultimate objective is the design of structure resisting to load blast, numerical simulations from ALE and SPH methods can be included in shape design optimization with shape optimal design techniques, see Souli et al. [77], and material optimization, see Erchiqui et al. [78]. Once simulations are validated by test results, they can be used as design tool for the improvement of the system structure being involved.

# Chapter 3

# NVH and Random Vibration Analysis Applied to Troop Seat Tube and Landing Gear

Sections 3.2 partly adapted from postprint version of:

**Failure and fatigue life estimate of a pre-stressed aircraft seat support tube**

Essam Al-Bahkali[1], Hisham Elkenani[1], and Mhamed Souli[2]

[1]Department of Mechanical Engineering, King Saud University, P.O. Box 800, Riyadh 11421, Saudi Arabia

[2]Laboratoire de Mécanique de Lille, UMR CNRS 8107, Villeneuve-d'Ascq, France

Published in:
Engineering Failure Analysis
Volume 54, Pages 120-130, 2015.
Doi: http://dx.doi.org/10.1016/j.engfailanal.2015.04.001

Section 3.3 partly adapted from postprint version of:

## Fatigue life estimate of landing gear's leg using modal analysis

Essam Al-Bahkali[1], Hisham Elkenani[1], and Mhamed Souli[2]
[1]Department of Mechanical Engineering, King Saud University, P.O. Box 800, Riyadh 11421, Saudi Arabia
[2]Laboratoire de Mécanique de Lille, UMR CNRS 8107, Villeneuve-d'Ascq, France

Published in:
The International Journal of Multiphysics
Volume 8, Issue 2, Pages 231-244, June 2014.
Doi: http://multi-science.metapress.com/content/7q62602610017864/?p=6f22ecf3a3ec4cdea273bf55c7845fd1&pi=5

In this chapter, Noise, Vibration, and Harshness (NVH) study is applied to three case studies: fatigue life prediction of a notched aluminium beam using Abaqus® and nCode DesignLife®, fatigue life estimate of a pre-stressed aircraft seat support tube and fatigue life estimate of landing gear's leg. In this study we investigate the effect of pre-stresses on modal analysis and demonstrate different methods used for life time estimation. A notched aluminum beam is considered as a benchmark for many literatures [4] where the experimental data and results obtained using other commercial codes are available. So, it was selected as a first case study in order to test our approach for random vibration analysis and fatigue life prediction.

## 3.1 Case Study One: Random Vibration Analysis and Fatigue Life Prediction of a Notched Aluminium Beam Using Abaqus® and nCode DesignLife®

Finite element analysis is very efficient in taking the Power Spectral Density (PSD) of applied loads and determining the PSD of the resulting stresses at various points in the structure. A method of taking the PSD of stress and calculating fatigue lives therefore has attractions. Much of the early work on fatigue analysis from PSD's was carried out by NASA in order to determine the fatigue damage caused by vibration and buffeting of space vehicles.

In this study, random response analysis of a notched aluminium beam, see Figure 3-1, has been carried with Abaqus® software. A frequency step was used for natural frequencies extractions, and then a random response step was used for calculating Root Mean Stress (RMS) from PSD load. The calculated value of RMS, 35.5 MPa, and the natural frequencies are in good agreement with the results by the others commercial software : 33.5 MPa for the ANSYS® and 35.7 MPa for RADIOSS BULK® [4].

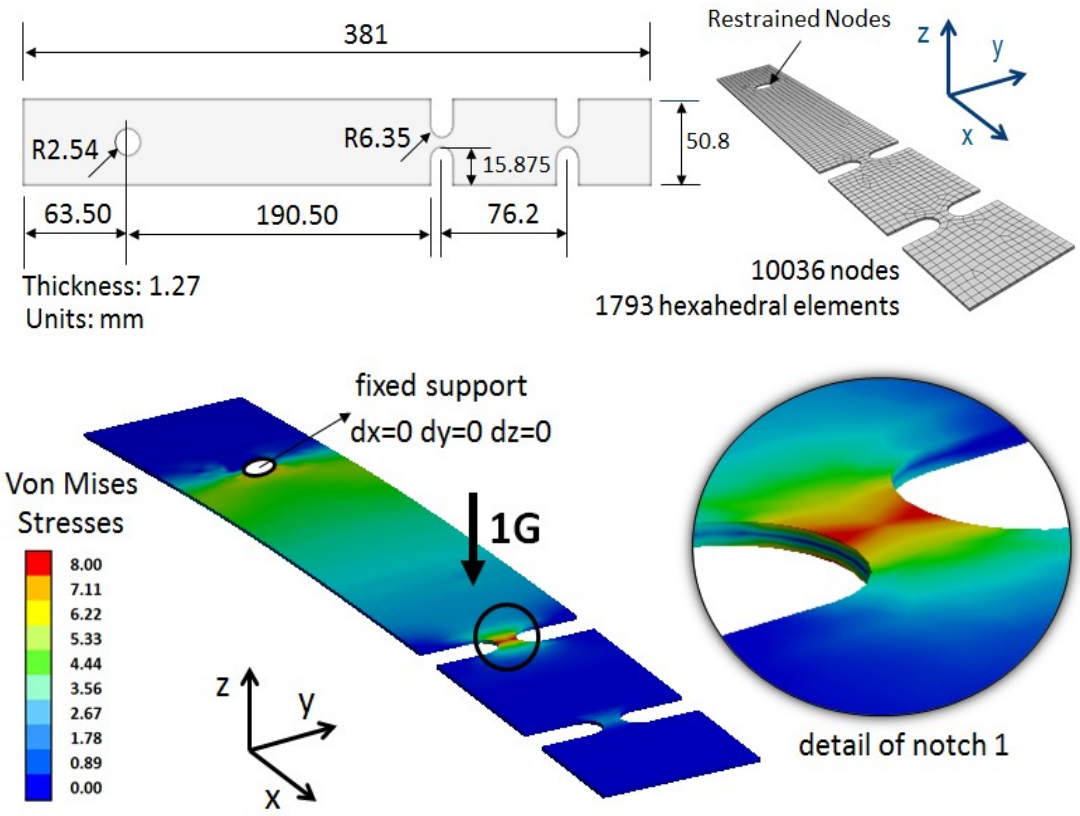


Figure 3-1 Finite element model used in the study

Abaqus® does not have fatigue solver. A third party code, nCode DesignLife®, one of SIMULIA® partners was used for fatigue life prediction. In Abaqus analysis, random response step was replaced with a steady state dynamic step. The base was excited by a 1 g acceleration in the Z-direction. The 1g acceleration is swept from 10 to 300 Hz. A constant damping of 0.04 has been input, and stress results clustered around the model's natural frequencies has been requested.

The fatigue assessment of the notched area is suggested by the European Standard Eurocode 9 [79]. According to this code the fatigue strength of plain material is described by the detail category FAT100 calculated for a probability of survival equal to 97.7%, a

reference fatigue strength $\Delta\sigma$ = 100 MPa at $2.10^6$ cycles and a single inverse constant slope $m$ = 7.0. The beam on the shaker table is shown in Figure 3-2.

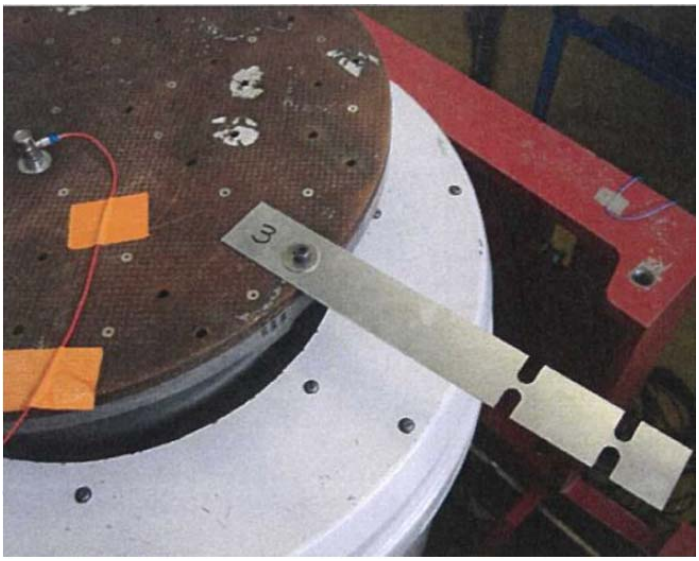


Figure 3-2 Beam on the shaker table.

The shaker test was conducted virtually in the work space of nCode DesignLife®, Figure 3-3 where the vibration load provider Glyph generated the PSD load. The ODB file generated by Abaqus® was used as input for the fatigue analysis Glyph. The ODB file contains Frequency Response Function (FRF) which provides the complex stress response (real and imaginary) to a unit excitation across the frequency range of interest.

The material S-N parameters were defined in nCode DesignLife® as well as the load in efficient and flexible manner. Statistical methods were used to predict PDF and rainflow count, namely: Dirlik, Steinberg and Narrow Band as shown in

Table 3-1. RMS calculated with nCode DesignLife was: 34.95 MPa which is closed to that one calculated with Abaqus.

| Theoretical Method | Fatigue Life (Min, Sec) |
|---|---|
| Dirlik | 5min 35Sec |
| Steinberg | 1min 44Sec |
| Narrow Band | 1min 34Sec |

Table 3-1 Life time values obtained using different theoretical methods

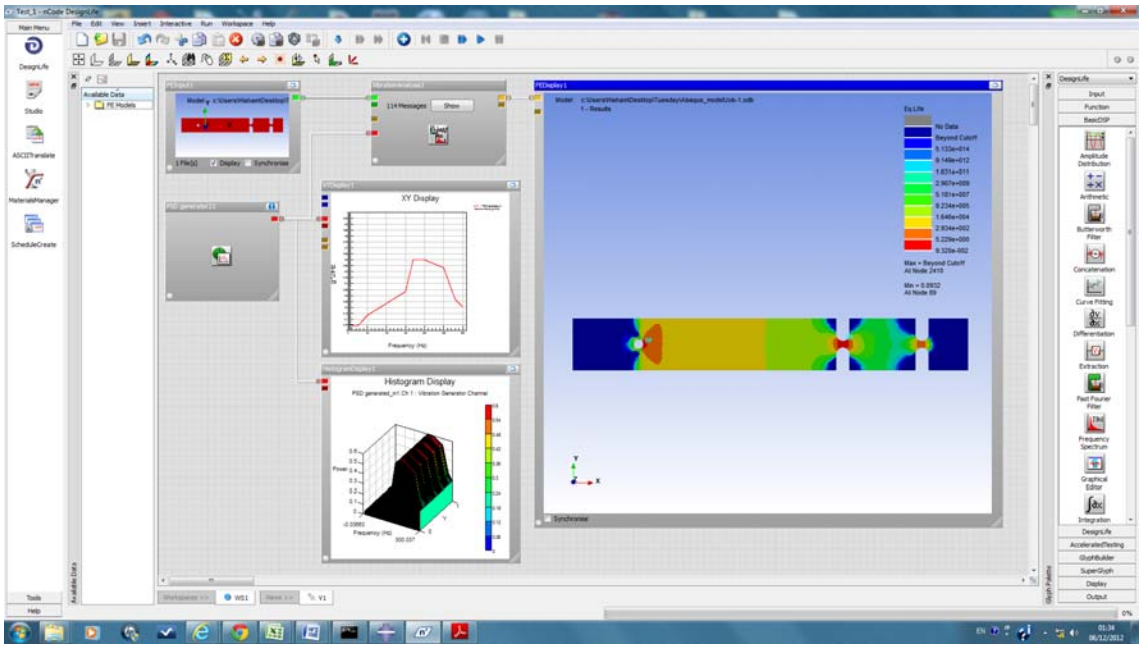


Figure 3-3 The shaker test was conducted virtually in the work space of nCode DesignLife

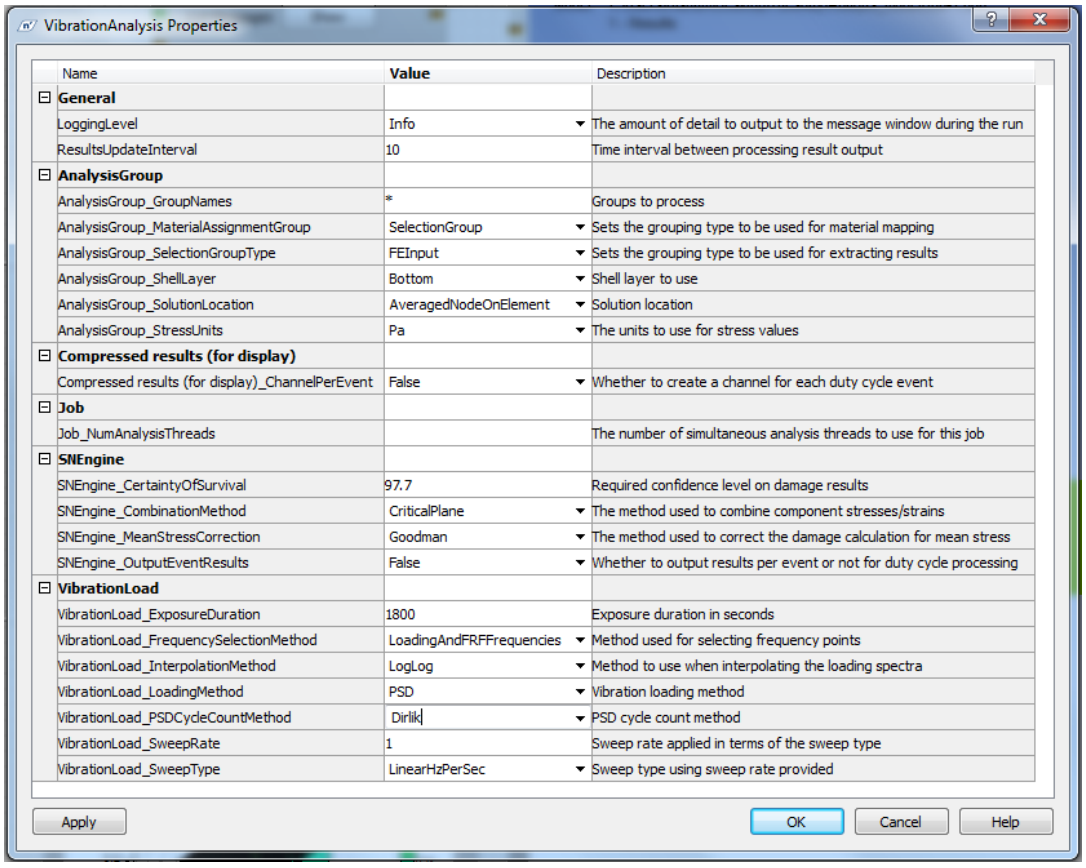


Figure 3-4 Vibration engine parameters

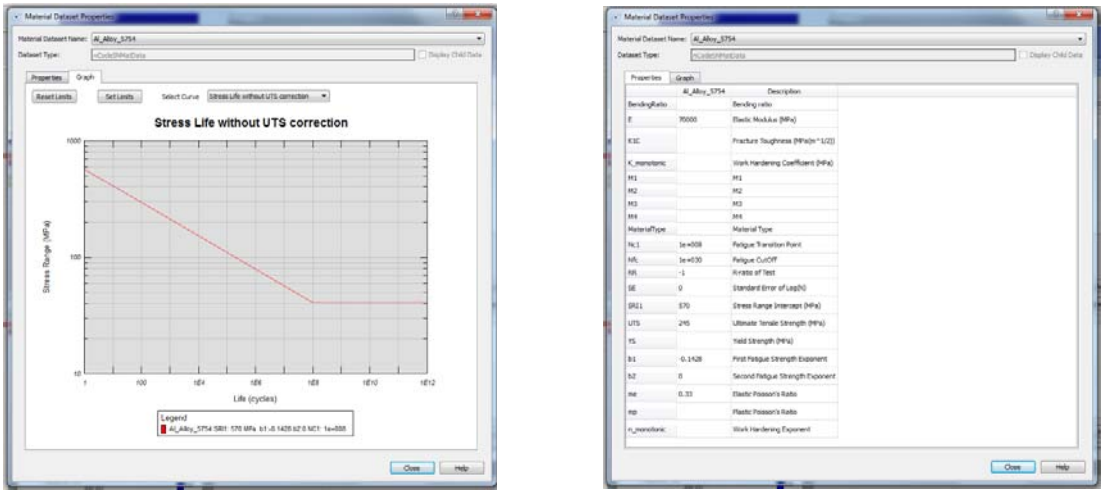


Figure 3-5 Material data editor

At this point we conclude that Abaqus doesn't has fatigue solver. So, in the next two cases I switched to LS-DYNA® commercial code where it has a built in fatigue solver. Throughout my simulation using LS-DYNA®, I gathered good practice with its different aspects and, proudly, earned a letter of appreciation from Livermore Software Technology Corp, LSTC, for my assistance in debugging a keyword input error in the pre/post processor, LS-PrePost, see App. C.

## 3.2 Case Study Two: Failure and Fatigue Life Estimate of a Pre-Stressed Aircraft Seat Support Tube

There have been increasing reports of annoyance, fatigue, and even neck and back pain during prolonged operation of troop propeller aircraft, where persistent multi-axis vibration occurs at higher frequencies. A claim from failure of the aluminum tube used as a seat support tube (SST) for troop seat –wall style- construction. A failure occurs after about 85 flight hours. A numerical static analysis model for the tube with its holders shows that it is safe, even with impact loading. In the present work, a random vibration analysis is

conducted using the mutiphysics software LS-DYNA® capability. First, a static analysis is performed using a pressure load on part of the tube that represents the seating location, followed by random vibration analysis. A contact algorithm is added in order to transfer the support's movement to the tube. The actual PSD profile are calculated according to the standards MIL-STD-810G. Dirlik method is used for the analysis of lifetime as it is proven to provide accurate results for large number of applications, both in automotive and aerospace industry. The predicted service life is about 83.3 hours which is close to the real actual life.

### 3.2.1 Introduction

Most real fatigue loadings are random processes in respect of frequency and stress amplitude. Estimating fatigue damage with Power Spectrum Density (PSD) was first proposed by Rice [80] in 1954. The stress power spectra density (PSD) represents the frequency domain approach input into the fatigue. This is a scalar function that describes how the power of the time signal is distributed among frequencies [81]. Mathematically this function can be obtained by using a Fourier transform of the stress time history's autocorrelation function, and its area represents the signal's standard deviation. It is clear that PSD is the most complete and concise representation of a random process [82]. Finite element analysis is very efficient in taking the PSD of applied loads and determining the PSD of the resulting stresses at various points in the structure. A method of taking the PSD of stress and calculating fatigue lives therefore has attractions. Much of the early work on fatigue analysis from PSD's was carried out by NASA in order to determine the fatigue damage caused by vibration and buffeting of space vehicles. The present work shows that the failure was occurs due to the random vibration load even the seat support tube (SST) geometry was safe regarding to static, dynamic and impact loads analysis. Similar attempt was done by Al-Bahkali, E., Elkenani, H. and Souli, M. [83] for unmanned vehicle landing gear.

### 3.2.2 Random Respons Analysis

Random response linear dynamic analysis is used to predict the response of a structure subjected to a nondeterministic continuous excitation that is expressed in a statistical sense by a cross-spectral density (CSD) matrix. The random response procedure uses the set of eigenmodes extracted in a previous eigenfrequency step to calculate the corresponding power spectral densities (PSD) of response variables (stresses, strains, displacements, etc.) and, hence—if required—the variance and root mean square values of these same variables. This section provides brief definitions and explanations of the terms used in this type of analysis based on the book by Clough and Penzien [84].

Examples of random response analysis are the study of the response of an airplane to turbulence; the response of a car to road surface imperfections; the response of a structure to noise, such as the "jet noise" emitted by a jet engine; and the response of a building to an earthquake.

Since the loading is nondeterministic, it can be characterized only in a statistical sense. We need some assumptions to make this characterization possible. Although the excitation varies in time, in some sense it must be stationary—its statistical properties must not vary with time. Thus, if $x(t)$is the variable being considered (such as the height of the road surface in the case of a car driving down a rough road), then any statistical function of x, $f(x)$, must have the same value regardless of what time origin we use to compute $f$:

$$f\big(x(t)\big) = f\big(x(t+\tau)\big) \quad for\ any\ \tau. \tag{3-1}$$

We also need the excitation to be ergodic. This term means that, if we take several samples of the excitation, the time average of each sample is the same. These restrictions ensure that the excitation is, statistically, constant.

The following subsections explain some concepts used in random response analysis.

### 3.2.2.1 Statistical Measures

The mean value of a random variable $x(t)$ is:

$$E(x) = \lim_{T\to\infty} \frac{1}{T} \int_{-\frac{T}{2}}^{\frac{T}{2}} x(t)\, dt. \tag{3-2}$$

Since the dynamic response is computed about a static equilibrium configuration, the mean value of any dynamic input or response variable will always be zero:

$$E(x) = 0. \tag{3-3}$$

The variance of a random variable measures the average square difference between the point value of the variable and its mean:

$$\sigma_r^2(x) = \lim_{T\to\infty} \frac{1}{T} \int_{-\frac{T}{2}}^{\frac{T}{2}} \big(x(t) - E(x)\big)^2\, dt. \tag{3-4}$$

Since $E(x) = 0$ for our applications, the variance is the same as the mean square value:

$$E(x^2) = \lim_{T\to\infty} \frac{1}{T} \int_{-\frac{T}{2}}^{\frac{T}{2}} x^2(t)\, dt. \tag{3-5}$$

The units of variance are (amplitude)$^2$, and are expressed as root mean square (RMS) values:

$$\sigma_r(x) = \sqrt{\sigma_r^2}. \tag{3-6}$$

### 3.2.2.2 Correlation

Correlation measures the similarity between two variables. Thus, the cross-correlation between two random functions is the integration of the product of the two variables $x_1$ and $x_2$, with one of them shifted in time by some fixed value $\tau$ to allow for the possibility that they are similar but shifted in time. The cross-correlation function for the variables is defined as:

$$R_{x_1x_2}(\tau) = \lim_{T\to\infty} \frac{1}{T} \int_{-\frac{T}{2}}^{\frac{T}{2}} x_1(t)\, x_2(t+\tau)\, dt. \tag{3-7}$$

Since the mean value of any variable is zero, on average each variable has equal positive and negative content. If the variables are quite similar, their cross-correlation (for some values of $\tau$ will be large; if they are not similar, the product $x_1x_2$will sometimes be negative and sometimes positive so that the integral over all time will provide a much smaller value, regardless of the choice of $\tau$). A simple result is:

$$R_{x_1x_2}(\tau) = R_{x_2x_1}(-\tau). \tag{3-8}$$

The autocorrelation is the cross-correlation of a variable with itself. Then the autocorrelation of a variable $x(t)$ is defined as:

$$R(\tau) = \lim_{T\to\infty} \frac{1}{T} \int_{-\frac{T}{2}}^{\frac{T}{2}} x(t)\, x(t+\tau)\, dt. \tag{3-9}$$

Clearly, as $\tau \to o,\ R(\tau) \to\ \sigma_r^2$, the autocorrelation equals the variance (the mean square value). The autocorrelation, $R(\tau)$ tells us about the nature of the random variable. If $R(\tau)$drops off rapidly as the time shift $\tau$ moves away from $\tau = 0$, the variable has a broad frequency content; if it drops off more slowly and exhibits a cosine profile, the variable has a narrow frequency content centered around the frequency corresponding to the periodicity of $R(\tau)$.

This concept is extended to detect the frequency content of a random variable by cross-correlating the variable with a sine wave: sweeping the wave over a range of frequencies and examining the cross-correlation tells us whether the random variable is dominated by oscillation at particular frequencies. We begin to see that the nature of stationary, ergodic random processes is best understood by examining them in the frequency domain.

We can write $x(t)$, which contains many discrete frequencies in terms of a Fourier series expanded in N steps of a fundamental frequency $\omega_0$:

$$x(t) = \sum_{n=1}^{N}[a_n \cos(\, in\, \omega_0 t) + b_n \sin(\, in\, \omega_0 t)] \tag{3-10}$$

Keeping in mind that we will be interested only in the real part, the variance of $x(t)$ can be expressed as:

$$\sigma_r^2(x) = \lim_{T\to\infty} \frac{1}{T} \int_{-\frac{T}{2}}^{\frac{T}{2}} \sum_{n=-N}^{N} A_n^*\, exp\,(-\, in\, \omega_0 t) A_n\, exp(in\omega_0 t)\, dt \tag{3-11}$$

Where $A_n$ is the complex amplitude of the nth term, $A_n^*$ is the complex conjugate of $A_n$. Using the orthogonality of Fourier terms. Continuing:

$$\sigma_r^2(x) = \lim_{T\to\infty} \frac{1}{T} \int_{-\frac{T}{2}}^{\frac{T}{2}} \sum_{n=-N}^{N} A_n^* \, A_n dt.$$

$$= \sum_{n=-N}^{N} A_n^* \, A_n = \sum_{n=-N}^{N} |A_n|^2 = \sum_{n=-N}^{N} \sigma_r^2(x_n) \quad (3\text{-}12)$$

where $x_n$is the $n$th component of the Fourier series.

The contribution to the variance of x, $\sigma_r^2(x)$, at the frequency $f_n = n\omega_0/(2\pi)$, per unit frequency, is thus:

$$S_x(f_n) = \frac{2\pi}{\omega_0} A_n A_n^* \quad (3\text{-}13)$$

since we are stepping up the frequency range in steps of $\Delta f = \omega_0/(2\pi)$. The variance can, therefore, be written as:

$$\sigma_r^2(x) = \sum_{n=-N}^{N} S_x(f_n)\Delta f \quad (3\text{-}14)$$

As we examine x as a function of frequency, $S_x(f_n)$ tells us the amount of "power" (in the sense of mean square value) contained in x, per unit frequency, at the frequency $f_n$. As we consider smaller and smaller intervals, $\Delta f \to 0$, $S_x$ is the power spectral density (PSD) of the variable x:

$$\sigma_r^2(x) = \int_{-\infty}^{\infty} S_x(f) df \quad (3\text{-}15)$$

### 3.2.2.3 Random Response Analysis

For a system excited by some random loads or prescribed base motions, which are characterized in the frequency domain by a matrix of cross-spectral density functions, $S_{NM}(f)$, we can think of N and M as two of the degrees of freedom of the finite element model that are exposed to the random loads or prescribed base motions. In typical applications the range of frequencies will be limited to those to which we know the structure will respond—we do not need to consider frequencies that are higher than the modes in which we expect the structure to respond.

The values of $S_{NM}(f)$ might be provided by Fast Fourier transform of the cross-correlation of time records or by the Fourier transform of the autocorrelation of a single time record, together with known geometric data. The system will respond to this excitation. We are usually interested in looking at the power spectral densities of the usual response variables—stress, displacement, etc. The PSD history of any particular variable will tell us the frequencies at which the system is most excited by the random loading.

An overall picture is provided by looking at the variance (the mean square value) of any variable; the RMS value is provided for this purpose. The RMS value is used instead of variance because it has the same units as the variable itself. It is computed by integrating the single-sided power spectral density of the variable, $\tilde{S}_x$ over the frequency range.

The transformation of the problem into the frequency domain inherently assumes that the system under study is responding linearly.

### 3.2.2.4 The Frequency Response Function (FRF)

Random response is studied in the frequency domain. Therefore, we need the transformation from load to response as a function of frequency. Since the random response is treated as the integration of a series of sinusoidal vibrations. The discrete (finite element) linear dynamic system has the equilibrium equation:

$$\delta u^N \left(M^{NM}\ddot{u}^M + C^{NM}\dot{u}^M + K^{NM}u^M\right) = \delta u^N F^N \quad (3.16)$$

where $M^{NM}$ is the mass matrix, $C^{NM}$ is the damping matrix, $K^{NM}$ is the stiffness matrix, $F^N$ are the external loads, $u^N$ is the value of degree of freedom N of the finite element model, and $\delta u^N$ is an arbitrary virtual variation.

The problem is projected onto the eigenmodes of the system, which are first extracted from the undamped system. The eigenmodes are orthogonal across the mass and stiffness matrices.

#### 3.2.2.5 Von Mises Stress Computation

This is a quite critical issue, which has been largely investigated in the literature. Noting that the von Mises stress is a quadratic stress function, therefore it is a non-Gaussian stress with positive mean value, even if its stress components are zero-mean Gaussian random stresses.

The first one and theoretical proper definition of the Mises stress in frequency domain was proposed by Preumont and Piefort [85]. An interesting paper about including the phase shift into von Mises PSD were written by Bonte [86].

The computation of PSD and RMS of von Mises stresses in this chapter is based on work by Segalman, et al. [87]. Under this approach the PSD of von Mises stress at a node a is given by:

$$S^a_{mises}(f) = \sum_{\beta=1}^{m}\sum_{\alpha=1}^{m} S_{\alpha\beta}(f)T^{\alpha}_{\alpha\beta}. \quad (3\text{-}17)$$

where m is the number of modes, $S_{\alpha\beta}(f)$ are the elements of the PSD matrix of ψgeneralized displacements:

$$T_{\alpha\beta}^{\alpha} = \left[\psi_{\beta}^{\alpha}\right]^{T}[A]\left[\psi_{\beta}^{\alpha}\right]. \tag{3-18}$$

$\left[\psi_{\beta}^{\alpha}\right]$ are the modal stress components of the $\alpha$ th mode at node a, and the constant matrix A is given by:

$$\begin{pmatrix} 1 & -1/2 & -1/2 & 0 & 0 & 0 \\ -1/2 & 1 & -1/2 & 0 & 0 & 0 \\ -1/2 & -1/2 & 1 & 0 & 0 & 0 \\ 0 & 0 & 0 & 3 & 0 & 0 \\ 0 & 0 & 0 & 0 & 3 & 0 \\ 0 & 0 & 0 & 0 & 0 & 3 \end{pmatrix}. \tag{3-19}$$

Similarly, RMS of von Mises stress at a node a is computed as:

$$RMISES^{a}(f) = \sqrt{\sum_{\beta=1}^{m}\sum_{\alpha=1}^{m} V_{\alpha\beta}(f)}\, T_{\alpha\beta}^{a}. \tag{3-20}$$

where $V_{\alpha\beta}(f)$ are the elements of the variance matrix of generalized displacements.

### 3.2.3 Frequency Domain Approaches of Life Estimation

Fatigue analysis can be conducted in both time and frequency domain. In time domain, rain-flow counting algorithm is usually used to calculate the number of cycles at each stress and strain levels based on the time history. Due to random load in many cases, a description in frequency domain is more efficient and hence using a statistical method is the most appropriate approach.

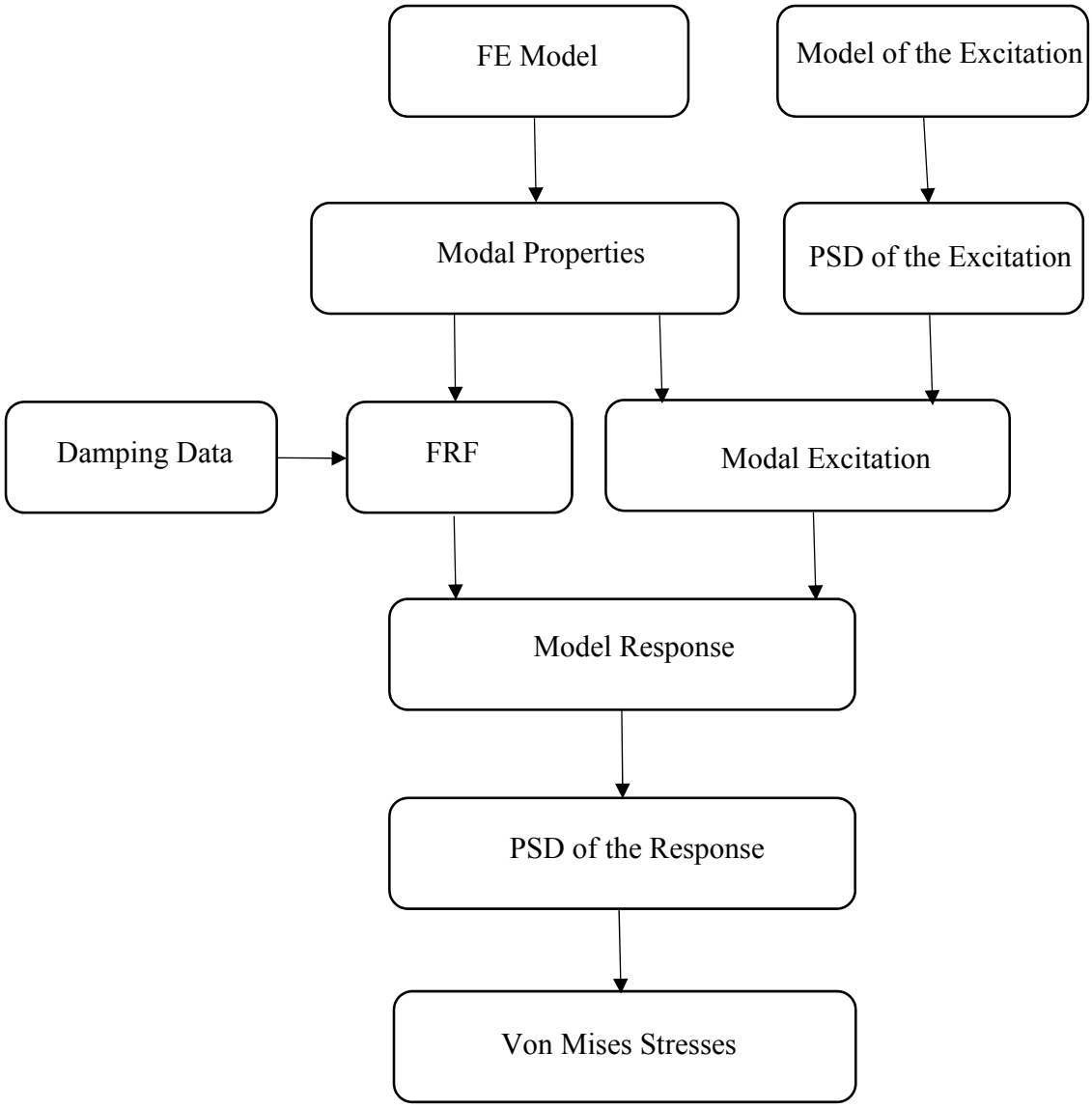


Figure 3-6 Spectral analysis of the stationary random response

There are seven frequency domain fatigue analysis methods have been implemented in LS-DYNA.

Figure 3-7 illustrates these methods and their common applications.

All of the shown methods are based on Palmgren-Miner's rule of cumulative damage ratio:

$$E[D] = \sum_i \frac{n_i}{N_i} \tag{3-21}$$

Where $E[D]$ is the expected damage ratio, $n_i$ is the number of cycles at stress level $S_i$, and $N_i$ is the number of cycles for failure at stress level $S_i$, given by material's S-N curve.

To get $n_i$ from the PSD of the random stress response and further compute E[D], a variety of statistical methods have been used to predict Probability Density Function (PDF) and rainflow count, namely:

Dirlik, Steinberg, Narrow Band,Wirsching, Chaudhury and Dover, Tunna and Hancock method.

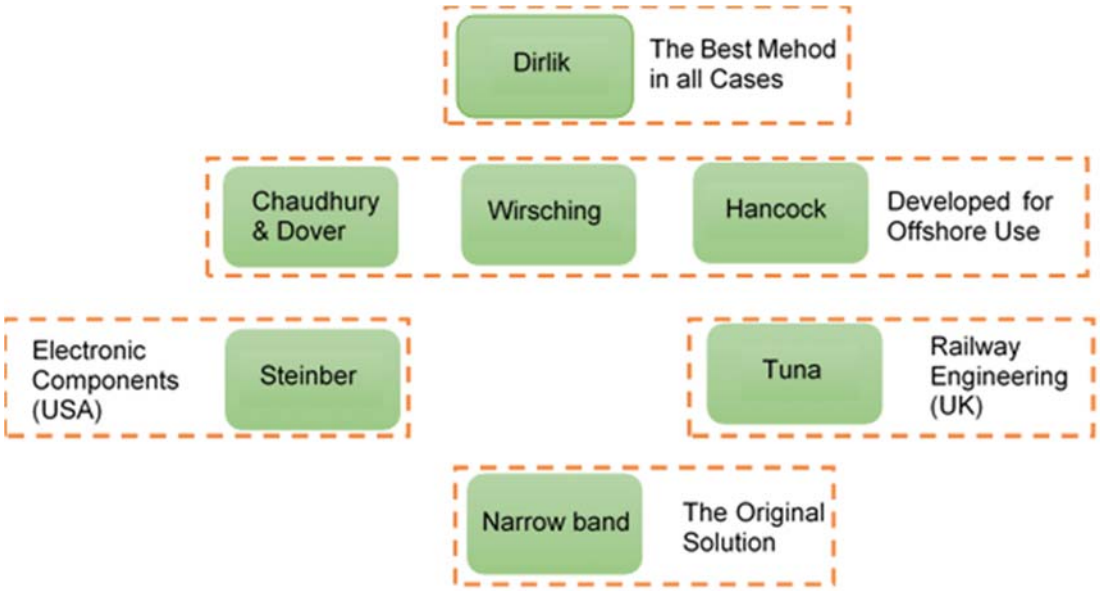


Figure 3-7 Frequency domain methods and their common applications

#### 3.2.3.1 Dirlik Method

The Dirlik method is a mathematical tool which used to performing fatigue analysis. To use this method, signals to be analysed must first be transferred from the time domain to the frequency domain where they are presented in the form of a power spectral density (PSD) function. Stress analysis in the time domain is ideally suited to signals representing periodic or continuous stress loading but for random stress loading data, prohibitively large time records are often required for an accurate analysis. There are distinct advantages in performing stress analysis in the frequency domain rather than the time domain where a random stress loading signal forms the basis for analysis. The main advantage is much less time intensive calculations although this comes at a cost of slight loss in accuracy.

Any fatigue analysis process begins with the response of the structure or component. This is normally expressed as a time history of stress or strain. Stress cycles in the time history result in fatigue and the most important aspects of these cycles are the stress amplitude ranges and the mean stress values. These values are normally analysed using Rainflow Cycle Counting. The time history data can be converted to data in the frequency domain by using a variation of the Fourier Transform. In both formats, the y-axis displays the signal amplitude but in the frequency domain, the x-axis represents the signal frequency as opposed to time. The Fourier Transform effectively breaks the signal down into discrete sinusoidal waves. These waves vary in frequency, phase and amplitude and form the original time signal again when combined using an inverse Fourier Transform.

The Dirlik method [88] [89], devised in 1985, approximates the cycle- amplitude distribution by using a combination of one exponential and two Rayleigh probability densities. It is based on numerical simulations of the time histories for two different groups of spectra. This method has long been considered to be one of the best methods and has already been subject to modifications, e.g., for the inclusion of the temperature effect, by Zalaznik and Nagode [90].

The Dirlik method consists of a series of calculations which are based on four moments of area of the PSD function and was taken from Halfpenny [91]. These moments of area

are $m_0$, $m_1$, $m_2$ and $m_4$. The nth moment of area is calculated as:

$$m_n = \int f^n . \, G(f) df \tag{3-22}$$

where $G(f)$ is the PSD function and f is the frequency in Hertz

The rainflow cycle amplitude probability density, $p_a$ estimate is given by:

$$p_a(S) = \frac{1}{\sqrt{m_0}} \left[ \frac{G_1}{Q} e^{\frac{-Z}{Q}} + \frac{G_2 Z}{R^2} e^{\frac{-Z^2}{2R^2}} + G_3 Z e^{\frac{-Z^2}{2}} \right] \tag{3-23}$$

where $Z$ is the normalized amplitude:

$$Z = \frac{S}{\sqrt{m_0}} \tag{3-24}$$

For a fatigue analysis the moments up to $m_4$ are normally used. The even moments represent the variance $\sigma_X^2$ of the random process X and its derivatives:

$$\sigma_X^2 = m_0 \qquad \sigma_{\dot{X}}^2 = m_2 \tag{3-25}$$

and the parameters $G_1$ to $G_3$, $R$ and $Q$ are defined as:

$$G_1 = \frac{2(x_m - \alpha_2^2)}{1+\alpha_2^2} \qquad G_2 = \frac{1-\alpha_2-G_1+G_1^2}{1-R}$$

$$G_3 = 1 - G_1 - G_2 \qquad R = \frac{\alpha_2 - x_m - G_1^2}{1-\alpha_2-G_1+G_1^2} \tag{3-26}$$

$$Q = \frac{1{,}25\,(\alpha_2 - G_3 - G_2 R)}{G_1}$$

where $x_m$ is the mean frequency, as defined by the author of the method [8]:

$$x_m = \frac{m_1}{m_0}\left(\frac{m_2}{m_4}\right)^{\frac{1}{2}} \tag{3-27}$$

where $\alpha_i$ is used for spectral width estimation and it has the general form:

$$\alpha_i = \frac{m_i}{\sqrt{m_0 m_{2i}}} \tag{3-28}$$

### 3.2.4 Frequency Domain Random Vibration Analysis

The random vibration capability of LS-DYNA® originated from Boeing's in-house vibroacoustic code N-FEARA [92]. This feature computes the dynamic response of structures exposed to vibration or structural-acoustic coupling based on a known source. Various excitations and acoustic environments can be considered, including base excitations, correlated or non-correlated acoustic waves such as plane wave, progressive wave, reverberant wave, turbulent boundary layer, etc. [93].

A keyword has been introduced in LS_DYNA® to perform random vibration analysis. Through the keyword, user provides information about the location, direction, range of frequencies for the random excitation and response area can be given as node, set of nodes,

set of segments, or part. The direction of load can be in any of the x, y, z directions or given as a vector. Load curve for the PSD loads in random computation are also specified under the keyword [4].

The feature of random vibration fatigue is implemented as an option of the keyword, as it is a natural extension of the random analysis procedure. The method for performing fatigue analysis is defined as well as the parts or elements where the fatigue analysis is needed. The material's S-N fatigue curve and some other options like the exposure time are also defined. Modal analysis is the first step for running the analysis and then the implicit solution started.

Ringeval A. and Huang Y. [4] give in their paper several examples to demonstrate the effectiveness of the random vibration fatigue analysis feature with LS-DYNA®. One of those examples is a simple cantilever aluminium beam subjected to base accelerations. The numerical values are compared with the experimental results and different fatigue failure theories are used to predict fatigue life. That example is considered as a benchmark for the verification of the results obtained with LS-DYNA® as the authors compare their results with those found in the literature for the same subject. Also, the same problem has been simulated with ANSYS® and RADIOSS® BULK and the maximum root mean square (RMS) stress computed by LS-DYNA® is in good agreement with the results obtained by the other commercial software. Nagulpalli et al. used commercial software Abaqus coupled with third part software, fe-Safe to study the same penchmark aluminium beam [94].

### 3.2.5 Contact Algorithm

Several contact methods have been published in litterarture between different structure material parts . Classical implicit and explicit coupling are described in detail in Longatte et al. [95] [96], where hydrodynamic forces from the fluid solver are passed to the structure solver for stress and displacement computation. In this study, a coupling method based on contact algorithm is used. Since the coupling method described in this chapter is based on the penalty method for contact algorithms, the contact approach is a good introduction to this method. In contact algorithms, a contact force is computed

proportional to the penetration vector, the amount the constraint is violated. In an explicit FEM method, contact algorithms compute interface forces due to impact of the structure on the fluid, these forces are applied to the fluid and structure nodes in contact in order to prevent a node from passing through contact interface. In contact algorithms, one surface is designated as a slave surface, and the second as a master surface. The nodes lying on both surfaces are also called slave and master nodes respectively. The penalty method imposes a resisting force to the slave node, proportional to its penetration through the master segment, as shown in Figure 3-8 describing the contact process. This force is applied to both the slave node and the nodes of the master segment in opposite directions to satisfy equilibrium.

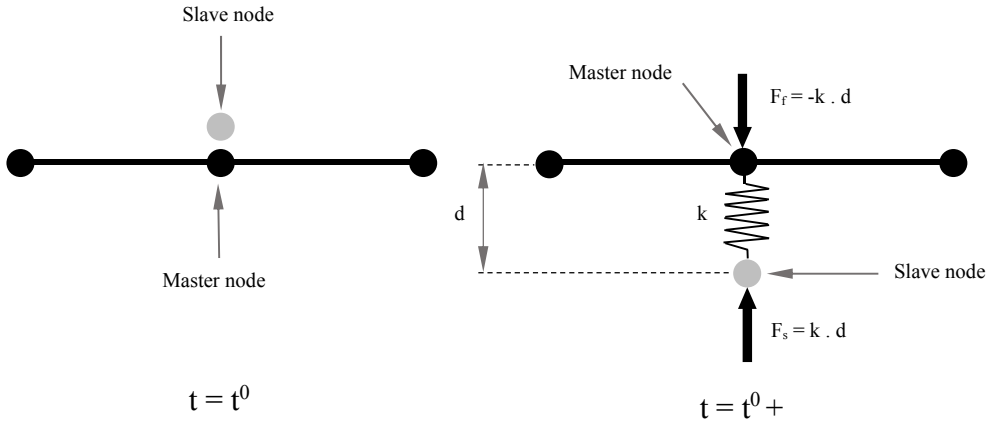


Figure 3-8 Description of Penalty Contact algorithm between slave node and master node

### 3.2.6 Troop Seat Wall Style

Aircraft industries have faced a problem with the seat support tube, Figure 3-9, currently used on the C-130 Lockheed Martin Aircraft. The SST has been continuously fracturing around the joint connection, which introduced the need to replace the SST frequently.

The weight of aircraft components has become an important factor. Efforts are being made to reduce the weight of the aircraft and consequently increase the payload. The SST is made of 2024-T3 Aluminum alloy which is widely used in aircraft industries due to its high strength ($\sigma_y$= 341 MPa) and low weight (density $\rho$ = 2700 kg/m3).

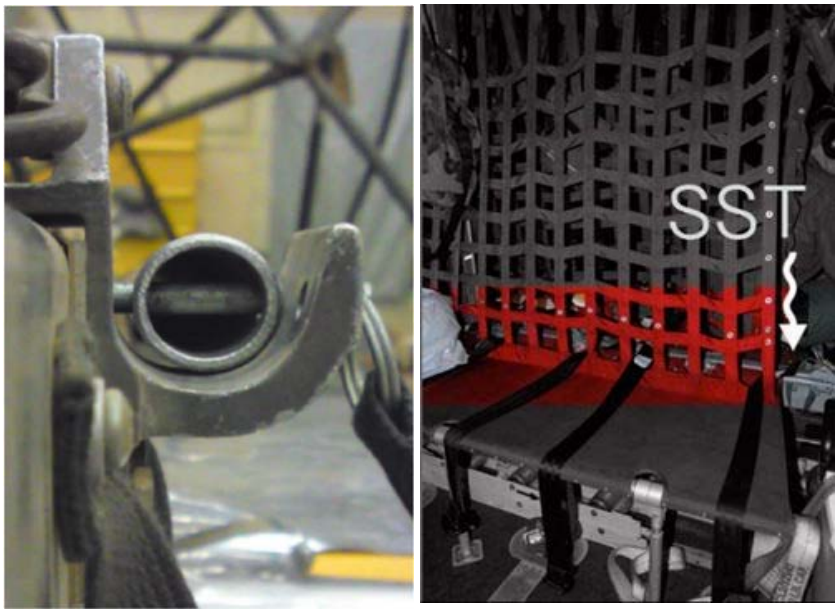


Figure 3-9 Seat Support Tube (SST)

The S-N fatigue curve, Figure 3-10, is selected according to the European Standard Eurocode 9 [97] with a reference fatigue strength $\Delta\sigma$ = 71 MPa at 2.106 cycles and a single inverse constant slope m = 7.0.

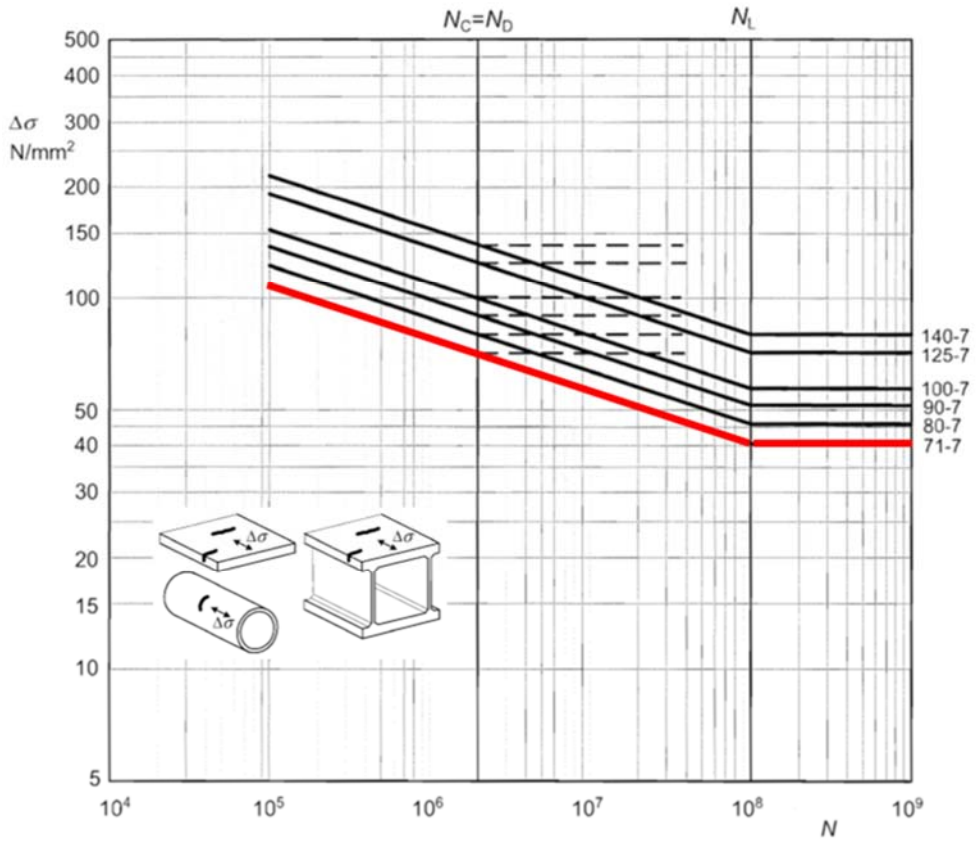


Figure 3-10 S-N fatigue curve used for the SST material

### 3.2.7 Analysis Steps

The tube was meshed with 12624 shell elements and the supporting holders and pins are meshed with 832 solid elements. Figure 3-11 shows the finite element model of the SST.

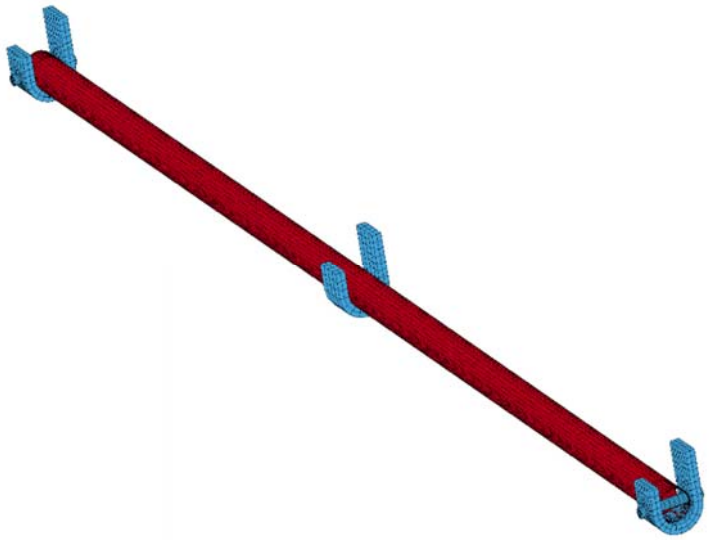

Figure 3-11 Finite element model of the SST.

An uniform pressure load, represents the pressure of the seat pan on the seat tube, is applied, Figure 3-12.

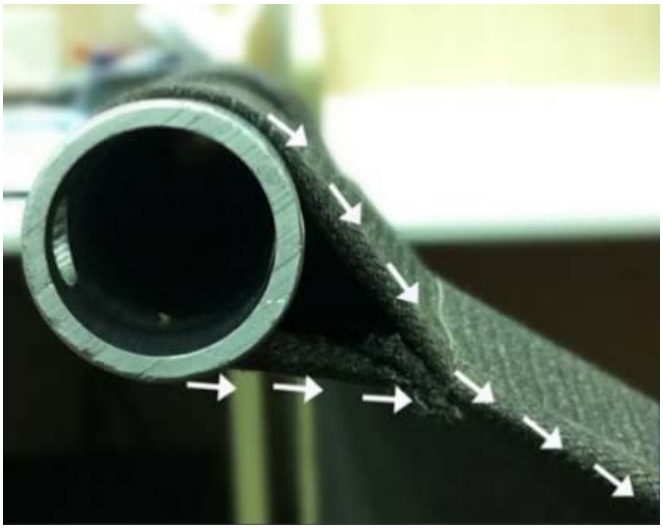

Figure 3-12 Uniform pressure load applied to the SST.

The static analysis results were accessed by the random vibration analysis as a preload stresses. A suitable contact algorithm was added in order to transfer the support's movement to the tube. Tube surface considered as the slave side while the pin surface considered as the master side. Initial assumption was adopted to prevent the initial penetration.

The two fixed pins were subjected to base Acceleration Spectral Density for the range of frequency 15-2000 Hz, as shown in Figure 3-13. The peaks of the load curve were calculated according to the number of propeller blades. In our case, we have four blades, Figure 3-14. The *dB Calculator* was used to calculate those peaks [98]. A constant damping ratio 0.02 was adopted. The SST was exposed to the random vibration load for one hour per axis as recommended by MIL-STD-810G [99].

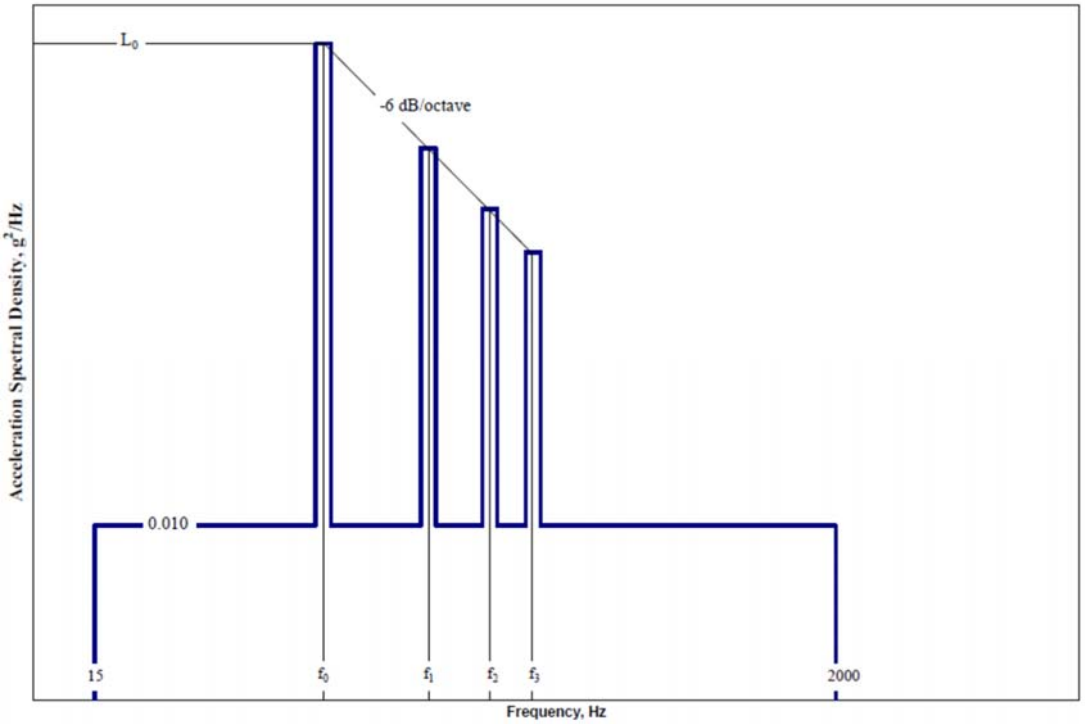


Figure 3-13 Propeller aircraft vibration exposure.

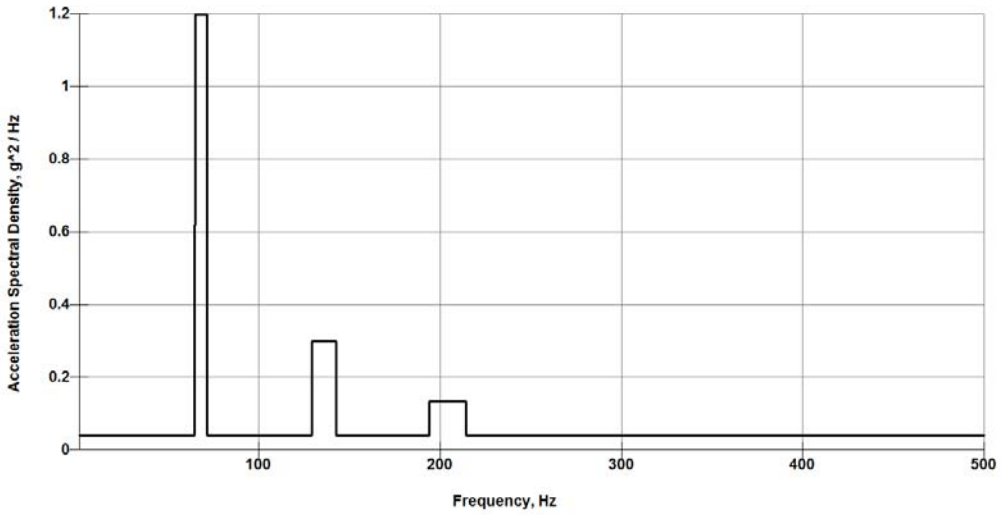


Figure 3-14 Input acceleration PSD.

The first 10 natural modes are required for the eigenvalue analysis. Lobatto's integration rule with three integration points through the thickness of the tube is applied to get the stress on the shell surface. The shear factor which scales the transverse shear stress, is suggested to have a value equal to 5/6. For shell element with implicit solution the invariant node numbering is taken as 2. An infinite fatigue life for stress lower than the lowest stress on S-N curve (40.6 MPa) was assumed, Figure 3-10. Due to the tube side oval holes, a further concentration factor $K_t$ is calculated as 0.26 [100].

### 3.2.8 Results

The response stress PSD measured at the critical point shows that the most natural frequency that has been excited by the input loading in the range 15-2000 Hz, Figure 3-15, equal to 1745 Hz.

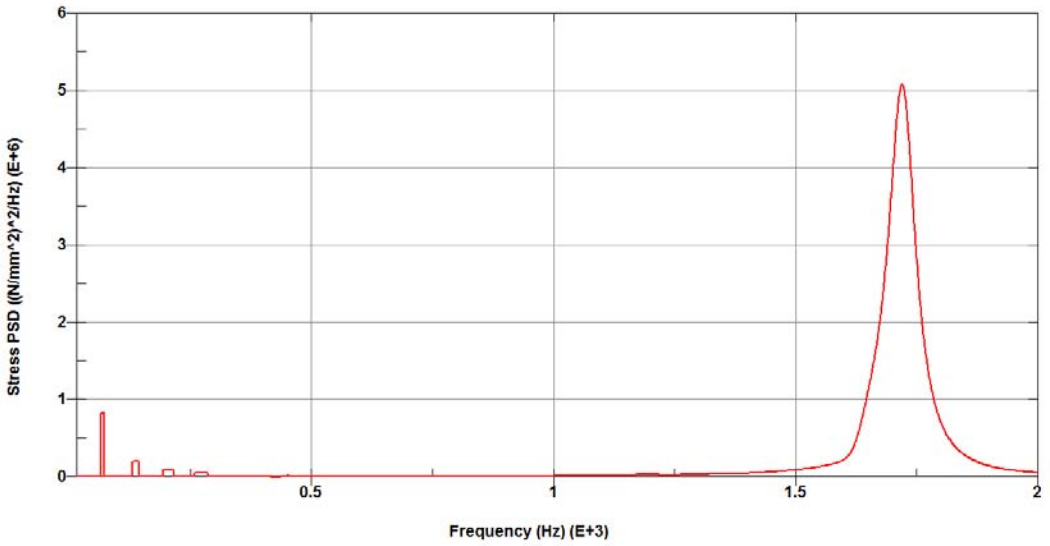


Figure 3-15 Stress PSD at critical point.

Based on Dirlik method results, the service life for the SST will be equal to 83.3 hours which is in a good agreement with the actual service life which is about 85 hours. Figure 3-16-a and Figure 3-16-b provide respectively a photograph of the broken SST and contour plot of the cumulative damage ratio observed on the SST. Results given by the numerical analysis are in good agreement with the actual failure location.

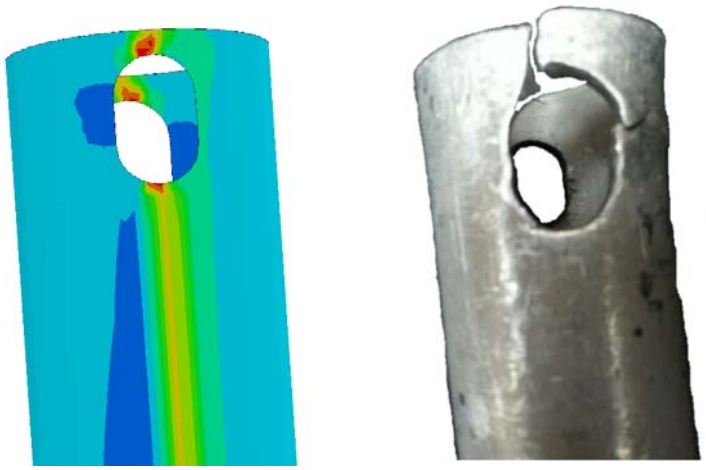

(a) (b)

Figure 3-16 (a) Cumulative damage ratio by Dirlik method and (b) the broken SST.

### 3.2.9 Conclusion

This chapter presents solving frequency domain random vibration fatigue. The analysis provides cumulative damage ratio calculation and fatigue life prediction for a typical Supported Seat Tube (SST) subjected to random vibration excitations. Dirlik method which has long been considered to be one of the best methods is demonstrated.

In this study, the random vibration analysis is conducted on the assembly of the SST where the contact algorithm was added in order to transfer the supporting pins' movement to the tube taking into consideration the pre-stress results in the static loading. Pre-stresses have two effects on the structure under vibration analysis: first, it makes it stiffer; second, it shifts the structure's natural frequencies.

In design of a structure in consideration of fatigue life, it is very important to evaluate not only the service life under the constant loading but also the fatigue life under the service loading. Due to the weight constrain, as in the case of the SST design, the margin of the factor of safety is limited. Therefore, it is essential to conduct fatigue analysis also to

predict the service life. In addition, the frequency response approach can improve understanding of the system dynamic behaviors, in terms of frequency characteristics of both structures and loads and their couplings.

## 3.3 Case Study Three: Fatigue Life Estimate of Landing Gear's Leg Using Modal Analysis

The present case concerns solving Noise, Vibration and Harshness (NVH) and fatigue based on Power Spectrum Density (PSD) analysis of a landing gear's leg for an Un-Manned Aerial Vehicle (UAV). This analysis includes random vibration and high-cycle fatigue analysis in a random vibration environment.

In this analysis, the cumulative damage ratio is computed using material S-N (Stress-Number of cycles) fatigue curve. Dirlik method is used for the analysis of life time as it is proven to provide accurate results for large number of applications, both in automotive and aerospace industry. It is also compared to other methods that have been developed in LS-DYNA® as well. The input acceleration PSD data are provided through measurements.

The obtained analysis results shows that although the landing gear design is safe according to dynamic and static load, its service life is about 3037 hours due to random vibration effect.

### 3.3.1 Landing Gear Design

The landing gear is a structure that supports an aircraft on ground and allows it to taxi, take off, and land [101]. In fact, landing gear design tends to have several interferences with the aircraft structural design. Nowadays the weight of landing gear has become an important factor. Efforts are being made to reduce the weight of the aircraft and consequently increase the payload. Design of landing gears takes the effect of static and dynamic loads as well as the impact loading. This study presents analysis for prediction of the service life for a light landing gear with a thickness optimized to only 8 millimeters. This design

optimization where carried by Albahkali E. and Alqhtani M. [102]. Dimensions of the landing gear are shown in Figure 3-17.

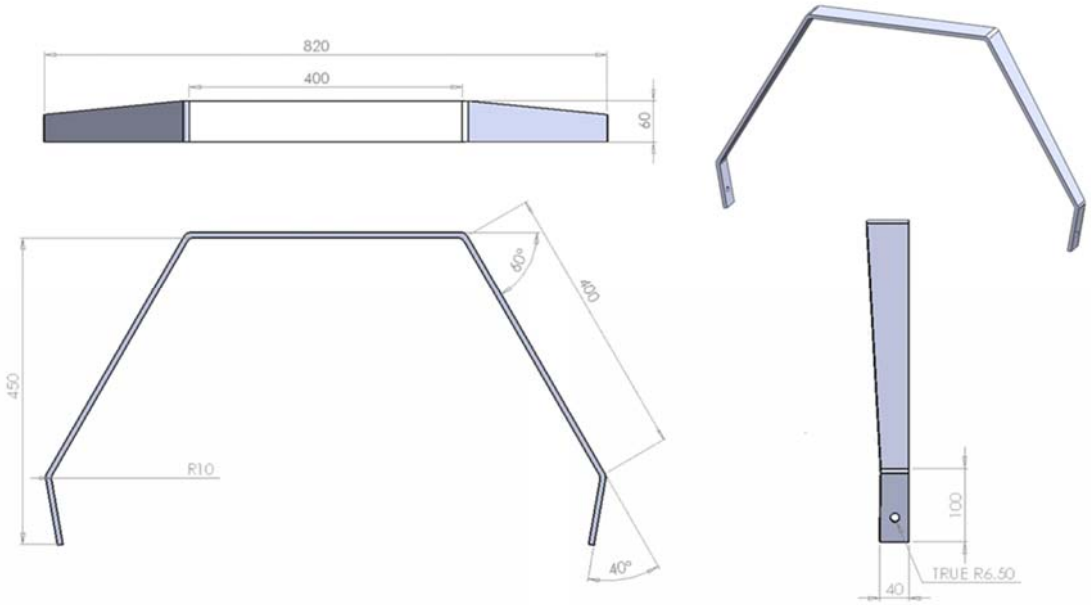


Figure 3-17 Geometry details of the landing gear (all dimensions are in millimeter)

As shown in Figure 3-18, the landing gear is clamped to the fuselage in its middle horizontal part. The two wheels attached to its ends are weighing 0.651 kg each.

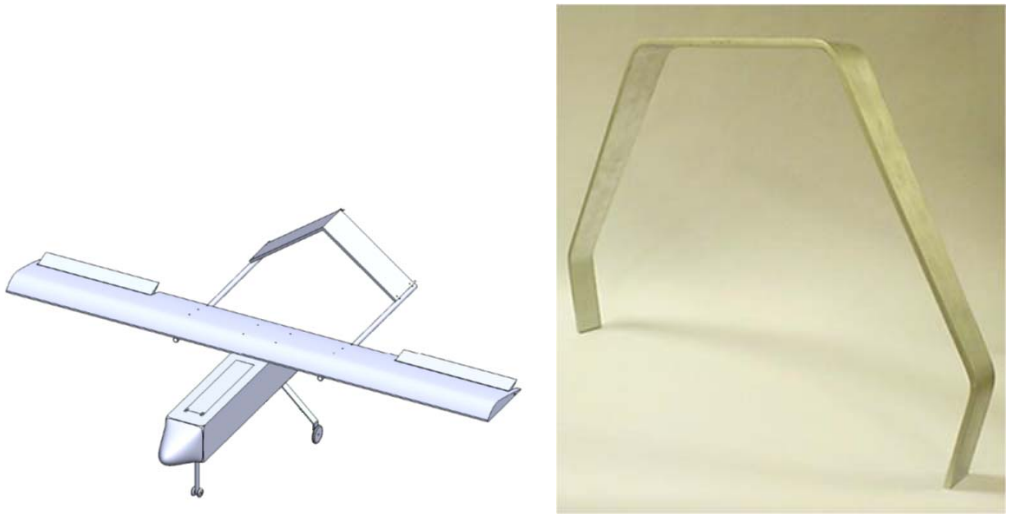

Figure 3-18 Landing gear

Figure 3-19 shows Power Spectral Density (PSD) outputs in $g^2/Hz$ for the landing gear vibration with change in frequency. It indicates random vibration loads on the landing gear. The modal frequencies required to calculate the resultant effect of modal spectrum vibration are extracted up to the spectrum frequency.

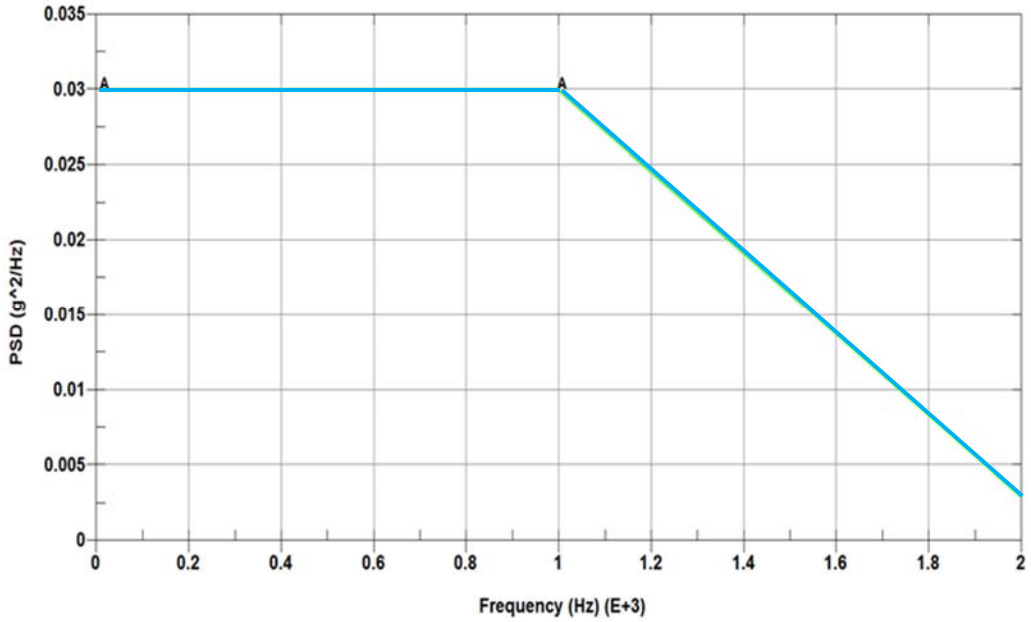


Figure 3-19 Input acceleration PSD

The landing gear is made from AA7076-T6 aluminum alloy with density $\rho$ = 2700 kg/m$^3$, Young's modulus $E$ = 70 G Pa and Poisson's ratio $v$ = 0.33. The S-N fatigue curve, Figure 3-20, is selected according to the European Standard Eurocode 9 [97] with a reference fatigue strength $\Delta\sigma$ = 71 MPa at 2.10$^6$ cycles and a single inverse constant slope m = 7.0.

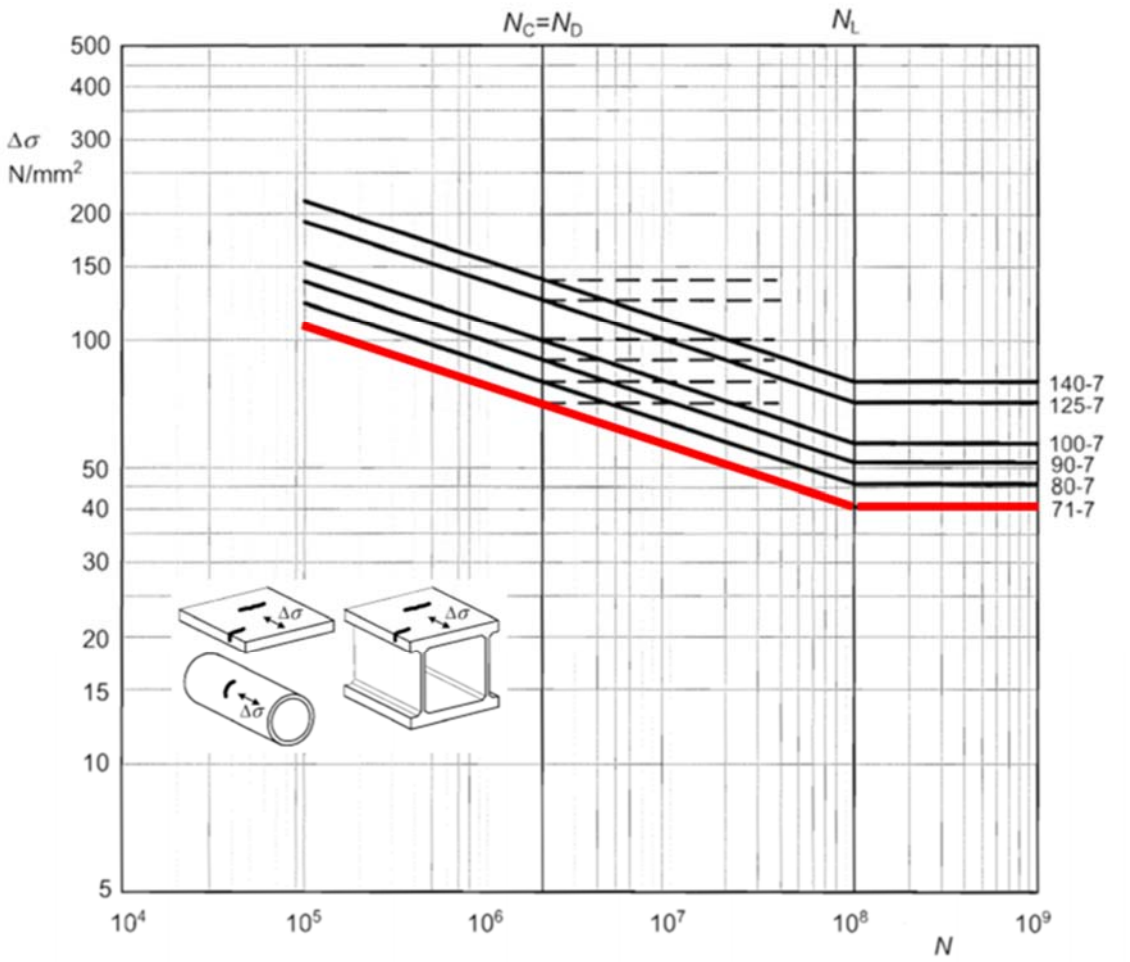


Figure 3-20 S-N fatigue curve used for the landing gear material

### 3.3.2 Analysis Steps

The model is meshed with 9073 nodes and 8576 shell elements (fully integrated linear DK quadrilateral and triangular shell). The two wheels are represented by 28 mass elements with 0.0465 kg each. They distributed uniformly at the circumference of the two holes. The upper face is subjected to base Acceleration Spectral Density for the range of frequency 0-2000 Hz. A constant damping ratio 0.035 is adopted. The landing gear is exposed to the random vibration load for 45 minutes (2700 seconds) which is equal to the flight time.

The first 10 natural modes are required for the eigenvalue analysis. Lobatto's integration rule with three integration points through the thickness of the landing gear is applied to get the stress on the shell surface. The shear factor which scales the transverse shear stress, is suggested to have a value equal to 5/6. For shell element with implicit solution the invariant node numbering is taken as 2. An infinite fatigue life for stress lower than the lowest stress on S-N curve (40.6 MPa) is assumed.

### 3.3.3 Results

The response stress PSD measured at the critical point shows that two natural frequencies are excited by the input loading in the range 10-2000 Hz (Figure 3-21), the first natural frequency (11.711 Hz) and the fifth natural frequency (105.77 Hz). When examine the model with higher input acceleration PSD load (g^2/Hz = 0.1), the eighth natural frequency (287.244 Hz) is excited also. Table 3-2 summarizes the fatigue life obtained by the numerical predictions methods.

As shown in Table 3-2, the results depend on the method used to interpret the RMS results. Steinberg, Chaudhury and Dover and Hancock methods give close results but conservative. Wirsching method gives less conservative results. Tunna's prediction is completely off. Narrow Band's prediction is too conservative comparing to the other methods.

Figure 3-22Figure 3-22 and Figure 3-23 show contour plot for the cumulative damage ratio and the RMS of $S_x$ stress at the critical point using Dirlik method respectively.

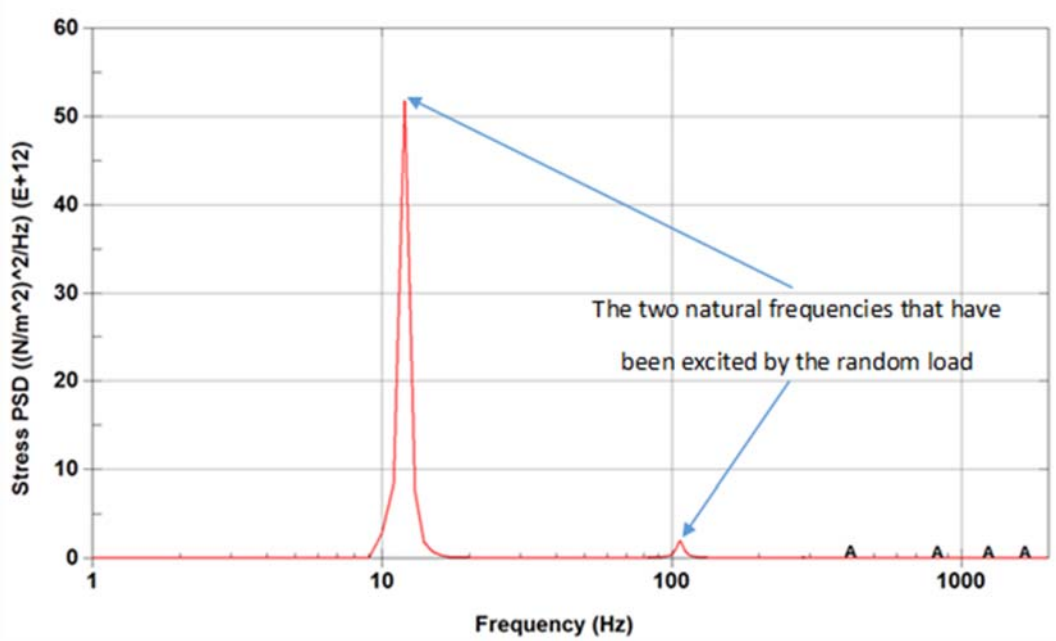


Figure 3-21 Stress PSD at critical point

| Method used | Fatigue life (Hrs.) | Cumulative fatigue ratio |
|---|---|---|
| Steinberg | 994.1 | 0.000754 |
| Dirlik | 3037.6 | 0.000246 |
| Narrow Band | 386.7 | 0.001939 |
| Wirsching | 1389.9 | 0.000539 |
| Chaudhury and Dover | 1035.1 | 0.000724 |
| Tunna | 67021.7 | 0.000011 |
| Hancock | 1040.0 | 0.000721 |

Table 3-2 Fatigue life obtained by the numerical predictions methods used in LS-DYNA®

Based on Dirlik method results, the service life for the landing gear will be equal to 3037.6 Hrs. or 4050 flight trips.

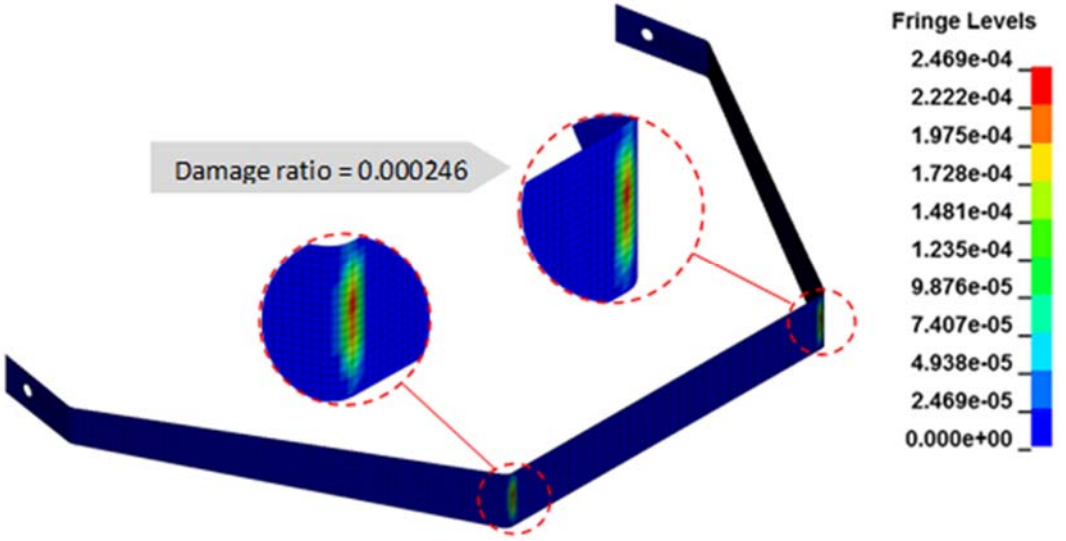


Figure 3-22 Cumulative damage ratio by Dirlik method

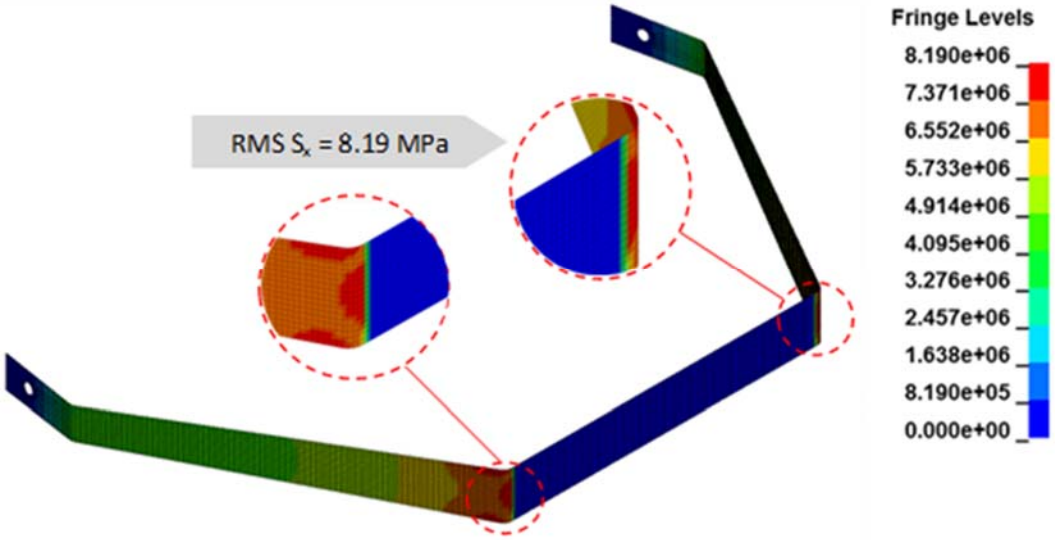


Figure 3-23 RMS of $S_x$ stress at the critical point using Dirlik method

### 3.3.4 Weight Optimization of the Landing Gear's Leg

The static and spectrum results indicate that the obtained stresses are low when compared to allowable stresses of the material, hence there is a possibility for optimization of the landing gear's legs thickness. The model with shell elements is considered for the analysis. The thicknesses are supplied as the real constants which can be easily optimized based on the optimization cycle satisfying the design requirements. The analysis is limited to main landing gear part. Since the axle dimension depends on wheel diameter and suspension, so the axle part is not considered for optimization.

It is shown in Figure 3-24 that a thickness of 6 mm is the optimal thickness regarding to the optimal life of 24000 hours.

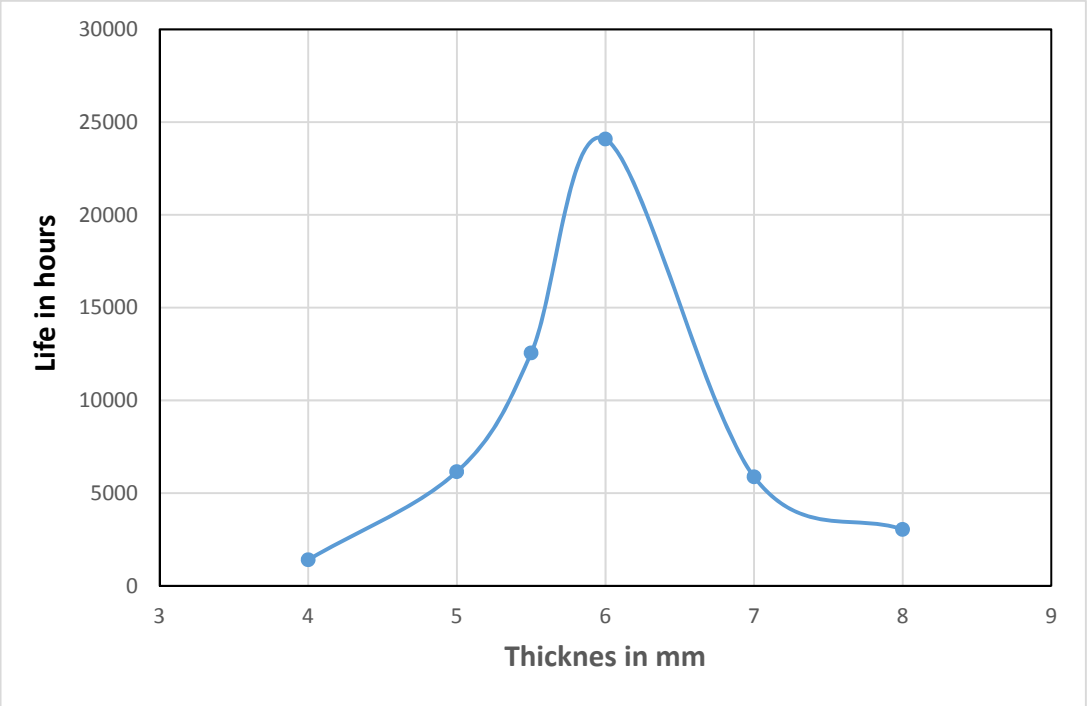


Figure 3-24 Life vs landing gear's leg thickness

### 3.3.5 Conclusion

In this chapter, we present solving frequency domain random vibration fatigue. The analysis provides cumulative damage ratio calculation and fatigue life prediction for a

typical UAV landing gear subjected to random vibration excitations based on various theories. Dirlik method which has long been considered to be one of the best methods is demonstrated.

The conservatism associated with Narrow Band solution method is clear as it gives the lowest predicted service life. On other side, Steinberg method didn't give excessive non-conservative results as the applied random signal is a broad-band one.

In design of a structure in consideration of fatigue life, it is very important to evaluate not only a fatigue life under the constant loading but also a fatigue life under the service loading. Due to weight constrain, as in the case of the landing gear design, the margin of the factor of safety is limited. Therefore, it is essential to conduct fatigue analysis also to predict the service life. In addition, the frequency response approach can improve understanding of the system dynamic behaviors, in terms of frequency characteristics of both structures and loads and their couplings.

# Conclusion and Perspective

## 4.1 Conclusion

The theme of this thesis is numerical and experimental modeling of blood flow in the arteries. Initial attempts to simulate blood flow in arteries made use of simplified geometries. This approach had limited applicability because of its inability to represent complex flow phenomena occurring in real blood vessels. The concept of patient-specific cardiovascular modeling was first established in [103], where real-life geometries were used to simulate blood flow. This opened the door for designing predictive tools for vascular modeling and treatment planning. Dramatic improvements in the computational results were observed in [103], yet the blood vessel wall was treated as being rigid. As was shown earlier, for example with the flexible and rigid wall computations [104], [105] the rigid wall assumption precludes pressure wave propagation and overestimates wall shear stress. There exists a variety of methods to include the effect of the moving wall in computations, the most prevalent being the arbitrary Lagrangian-Eulerian (ALE) and coupled Eulerian-Lagrangian (CEL) approaches.

In chapter one, CEL method have been investigated to solve FSI problem involving pulse wave (PW) propagation in artery wall due to blood flow. The simulation was validated by in vivo data and the theoretical theory. The effect of fluid compressibility, affected by sound speed value, on the computational cost was tested.

In chapter two, SPH method have been investigated to solve membrane inflation problem.

Referred to the two simulations of the above two problems, we can compare both CEL and SPH and conclude that unlike CEL method, and because of the absence of the mesh, SPH method suffers from a lack of consistency that can lead to poor accuracy. We can conclude also that FE method is the most suitable method for modeling blood as it uses less number of elements comparing with SPH method which needs more number of particles and hence more computation time.

On other side, high nonlinearities associated with the behavior of blood vessels in the human body limit the practical application of the analytical methods in their evaluation. Accurate measurement of mechanical parameters in vivo using experimental methods is extremely difficult, if not impossible. Much progress has been made using medical imaging equipment, however challenges still remains. These factors have opened the door to numerical simulations, which are able to give acceptable predictions of the mechanical behavior of blood vessels based on the minimal input information. For the fast decades, numerical simulations are increasingly being used in all branches of the biomechanics and provide valuable information to understand the basic physics of various parts of the human anatomy.

In this context, few attempts of local PWV measurement, as example, in carotid artery exist at present, and the present study provides a new alternative of "gold standard" in this field as it could be applied for a relatively short distance.

In chapter three, NVH study is applied to three case studies: fatigue life prediction of a notched aluminum beam, fatigue life estimate of a pre-stressed aircraft seat support tube and fatigue life estimate of landing gear's leg. In this study we investigate the effect of pre-stresses on modal analysis and demonstrate different methods used for life time estimation. Our intend from this study is to investigate the nature of random vibration and its fatigue sequence and its relation to the PW propagation through arteries. Due time restriction, we consider it as a future study.

## 4.2 Perspectives

This thesis follows the practices gathered from the mentioned simulations problems that conducted using Abaqus®, nCode DesignLife® and LS-DYNA® finite element commercial packages and SolidWorks® commercial package as well as the different simulation techniques. These practices gave arise to additional future works in the following areas:

- **Patient-specific cardiovascular modeling:** Where real-life geometries were used to simulate blood flow.
- **Local PWV measurement:** In the early stage of arterial stiffness, fibrous spots with small diameter are scattered on the arterial wall and, in the final stage, the arterial wall becomes homogeneously hard. The simulation of local PWV measurement is made on a short segment of an artery and represents an early diagnosis tool able to identify the local stiffness of the arterial wall [4] [5].
- **Wall shear stress of blood vessels:** These simulations are gradually expanded to include results for the wall shear stress distributions of the blood vessels.
- **Prediction of plaque rupture:** The study of fatigue life estimation could be applied on plaque rupture prediction.
- **Human vibration:** The effect of vibration on artery wall could be simulated.

# Bibliography

[1] Mohiaddin RH, Longmore DB, "MRI studies of atherosclerotic vascular disease: structural evaluation and physiological measurements," *Br Med Bull,* vol. 45(4), no. Oct, pp. 968-90, 1989.

[2] Kao TW, Taylor HF, "High-sensitivity intrinsic fiber-optic Fabry-Perot pressure sensor," *Opt Lett ,* vol. 21, pp. 615-7, 1996.

[3] Tabrizchi R, Pugsley MK, "Methods of blood flow measurement in the arterial circulatory system," *J Pharmacol Toxicol Methods ,* vol. 44, pp. 375-84, 2000.

[4] Ringeval A., Huang Y., "Random vibration fatigue analysis with LS-DYNA®," in *Proceedings of the 12th International LS-DYNA® Users Conference*, Dearborn, Michigan, USA , June 3-5, 2012 .

[5] L. L. Lanoye, J. A. Viereneels, P. Segers, P.R. Verdonck, "Simulation of arterial pulse wave propagation with fluid–structure interaction using Fluent and Abaqus software," *Computer Methods in Biomechanics and Biomedical Engineering. 2007,10:sup1, 61.,* vol. 10, no. 1, pp. 61-62, 2007.

[6] T. Young, "Hydraulic investigations, subservient to an intended croonian lecture on the motion of blood," *Philosophical Transactions of the Royal Society (London),* vol. 98, pp. 164-186, 1808.

[7] J. R. Womersley, "An elastic tube theory of pulse transmission and oscillatory flow in mammalian arteries," *Tech. Rep. ,* Vols. WADC-TR-56, p. 614 , 1957.

[8] W. W. Nichols, "Clinical measurement of arterial stiffness obtained from noninvasive pressure waveforms," *Am. J. Hypertens,* vol. 18 (1Pt2), no. 3S, 2005.

[9] Sturla, F.; Emiliano, V.; Marco, S.; Carlo, A. C.; Alberto, R., "Impact of modeling fluid–structure interaction in the computational analysis of aortic root biomechanics," *J. Medical Eng. & Physics,* vol. 35, pp. 1721-1730 , 2013.

[10] Wu, W.; Pott, D.; Mazza, B.; Sironi, T.; Dordoni, E.; Chiastra, C.; Petrini, L.; Pennati, G.; Dubini, G.; Steinseifer, U.; Sonntag, S.; Kuetting, M.; Migliavacca, F., "Fluid–structure interaction model of a percutaneous aortic valve: comparison with an in vitro test and feasibility study in a patient-specific case," *Annals of Biomedical Engineering,* vol. 44, no. 2, pp. 590-603, 2016.

[11] Lau, K. D.; Dı´az-Zuccarini, V.; Scambler, P.; Burriesci, G., "Fluid–structure interaction study of the edge-to-edge repair technique on the mitral valve," *Journal of Biomechanics,* vol. 44, pp. 2409-2417, 2011.

[12] Kuntz, M., Menter, F. R., "Simulation of fluid-structure interactions in aeronautical applications," *European Congress on Computational Methods in Applied Sciences and Engineering,* vol. ECCOMAS, 2004.

[13] Penrose, J. M. T., Staples, C. J., "Implicit fluid–structure coupling for simulation of cardiovascular problems," *Int. J. Numer. Meth. Fluids,* vol. 40, pp. 467-478, 2002.

[14] D. Korteweg, "Uber Die Fortpflanzungsgeschwindigkeit Des Schalles in Elastiischen Rohren," *Ann. Phys. Chem.,* vol. 5, pp. 525-537, 1878.

[15] Moatamedi, M., Souli, M., Al-Bahkali, E., "Fluid structure coupling method of blood flow in vessels," *Molecular & Cellular Biomechanics,* vol. 11, no. 4, pp. 221-234, 2014.

[16] Souli, M, Al-Bahkali, E., Al-Bahkali, T., Moatamedi, M., "Investigation of blood flow modeling in artery using ALE formulation," *Int. J. Computational Methods,* vol. 14, no. 1, 2017.

[17] Shahmirzadi, D., Li , RX., Konofagou, EE., "Pulse-wave propagation in straight-geometry vessels for stiffness estimation: theory, simulations, phantoms and in vitro findings," *J. Biomechanical Engineering. ASME,* vol. 134, no. 11, pp. 1-6, 2012.

[18] Fukui, T., Parker, K. H., Yamaguchi, T., "Single and Two-Phase Flows on Chemical and Biomedical Engineering," Vols. [14] Fukui, T.; Parker, K. H.; Yamaguchi, T.: Single and Two-Phase Flows on Chemical and Biomedical Engineering, Benthem Books. ISBN: 978-1-60805-504-3, 460-471 (2012), Benthem Books. ISBN: 978-1-60805-504-3, 2012, pp. 460-471.

[19] Laurent S and Cockroft J, "Central Aortic Blood Pressure," *Elsevier,* vol. s.1., 2008.

[20] E. King, et al., "The reliable measurement of radial pulse characteristics," *Acupunct Med,* vol. 20, p. 150-9, Dec 2002.

[21] Westerhof N., et al., Snapshots of Hemodynamics, Springer, 2005.

[22] N. Westerhof, et al., Snapshots of Hemodynamics, Springer, 2005.

[23] R. Asmar, Arterial Stiffness and Pulse Wave Velocity. Clinical Applications, ELSEVIER, 1999.

[24] M. Faber and G. Oller-Hou, "The human aorta. V. Collagen and elastin in the normal and hypertensive aorta," *Acta Pathol Microbiol Scand,* vol. 31, p. 377-82, 1952.

[25] A. P. Avolio, et al., "Effects of aging on changing arterial compliance and left ventricular load in a northern Chinese urban community," *Circulation,* vol. 68, no. Jul , p. 50-58, Jul 1983.

[26] G. M. London, et al., "Influence of sex on arterial hemodynamics and blood pressure. Role of body height," *Hypertension,* vol. 26, no. Sep, p. 514-9, 1995.

[27] B. Sonesson, et al., "Compliance and diameter in the human abdominal aorta--the influence of age and sex," *Eur J Vasc Surg,* vol. 7, no. Nov , p. 690-7, 1993.

[28] A. Benetos, et al., "Determinants of accelerated progression of arterial stiffness in normotensive subjects and in treated hypertensive subjects over a 6-year period," *Circulation,* vol. 105, no. Mar 12, p. 1202-7, 2002.

[29] P. Boutouyrie, et al., "Sympathetic activation decreases medium-sized arterial compliance in humans," *Am J Physiol,* vol. 267, no. Oct, p. H1368-76, 1994.

[30] Wentland AL, Grist TM, Wieben O, "Review of MRI-based measurements of pulse wave velocity: a biomarker of arterial stiffness," *Cardiovasc Diagn Ther,* vol. 4, no. 2, pp. 193-206, 2014.

[31] E. Arnold, Blood Flow in Arteries, Paris: McDonald, 1990.

[32] D. H. Bergel, *The visco-elastic properties of the arterial wall,* PhD thesis, University of London , 1961.

[33] Taewon, "Numerical simulations of blood flow in arterial bifurcation models," *Taewon (2013). Studies conducted by Gupta (2011) and Fan (2009)Korea-Australia Rheology Journal,* vol. 25, no. 3 , pp. Taewon (2013). Studies conducted by Gupta (2011) and Fan (2009) Numerical simulations of blood flo153-161 , Taewon (2013). Studies conducted by Gupta (2011) and Fan (2009) Numerical simulations of blood flo2013.

[34] A. Gupta, "Performance and analysis of blood flow through carotid artery," *Int. J. Eng. Bus. Manag,* vol. 3 , no. , pp. 1-6 , 2011 .

[35] Fan, Y., W. Jiang, Y. Zou, J. Li, J. Chen and X. Deng , "Numerical simulation of pulsatile non-Newtonian flow in the carotid artery bifurcation," *Acta Mech Sin. ,* vol. 25, no. , pp. 249-255 , 2009.

[36] A. 6.13, *Online Documentation 2013. ©Dassault Systèmes.,* ©Dassault Systèmes, 2013.

[37] Grote, M. J., Keller, J. B., "Exact non-reflecting boundary conditions for the time dependent wave equation," *SIAM Journal of Applied Mathematics,* vol. 55, no. 2, pp. 280-297, 1995.

[38] Grote, M. J., Keller, J. B., "Non-reflecting boundary conditions for time dependent scattering," *Journal of Computational Physics,* vol. 127, no. 1, pp. 52-65, 1996.

[39] Bayliss, A., Turkel, E., "Radiation boundary conditions for wave-like equations," *Communications in Pure and Applied Mathematics,* vol. 33, no. 6, pp. 707-725, 1980.

[40] Millasseau, S. C., Stewart, A. D., Patel, S. J., Redwood, S. R., Chowienczyk, P. J., "Evaluation of carotid-femoral pulse wave velocity: influence of timing algorithm and heart rate," *Hypertension,* vol. 45, no. 2, pp. 222-226, 2005.

[41] Shahmirzadi, D., Konofagou, E. E., "Detection of aortic wall inclusions using regional pulse wave propagation and velocity in silico," *J. Artery Research,* vol. 6, no. 3, pp. 114-123, 2012.

[42] C.G. Caro, T.J. Pedley, R.C. Schroter, W.A. Seed, The Mechanics of the Circulation, Oxford University Press, ISBN 0-19-263323-6, 1978.

[43] P. Boutouyrie, S. J. Vermeersch, "Determinants of pulse wave velocity in healthy people and in the presence of cardiovascular risk factors: establishing normal and reference values," *Eur Heart J,* vol. 31, no. 19, p. 2338–2350, 2010.

[44] Aquelet N, Souli M, Olovson L., "Euler Lagrange coupling with damping effects: Application to slamming problems," *Computer Methods in Applied Mechanics and Engineering,* vol. 195, pp. 110-132, 2005.

[45] Ozdemir Z, Souli M, Fahjan, YM., "Application of nonlinear fluid-structure interaction methods to seismic analysis of anchored and unanchored tanks," *Engineering Structures,* vol. 32, no. 2, pp. 409-423, 2010.

[46] Han,Z.D.;Atluri,S.N. , "On the Meshless Local Petrov-Galerkin MLPG-Eshelby Method in Computational, Finite Deformation Solid Mechanics - Part II," *CMES: Computer Modeling in Engineering & Sciences,* vol. 97, no. 3, pp. 199-237, 2014.

[47] Shuyao, L.; Atluri, S. N. , "A Meshless Local Petrov-Galerkin Method for Solving the Bending Problem of a Thin Plate," *CMES: Computer Modeling in Engineering & Sciences ,* vol. 3, no. 1, pp. 53-63 , 2002.

[48] Atluri, S. N.; Han, Z. D.; Rajendran, A. M. , "A New Implementation of the Meshless Finite Volume Method, through the MLPG 'Mixed Approach'," *CMES: Computer Modeling in Engineering & Sciences,* vol. 6, no. 6, pp. 491-513 , 2004.

[49] H. JO., *LS-DYNA theory manual,* Software Technology Corporation, 1998.

[50] Von Neumann, J.; Richtmeyer, R. D., "A method for the numerical calculation of hydrodynamical shocks," *Journal of Applied Physics,* vol. 21, p. 232, 1950.

[51] D. Benson, "Computational methods in Lagrangian and Eulerian hydrocodes," *Computer Method Applied Mech and Eng ,* vol. 99, no. 2-3, pp. 235-394, 1992.

[52] J. R. R. Von Neumann, "A method for the numerical calculation of hydrodynamical shocks," *Journal of Applied Physics ,* vol. 21, no. 3, p. 232, 1950.

[53] J. J. Monaghan, "Smoothed Particle Hydrodynamics and Its Diverse Applications," *Annual Review of Fluid Mechanics,* vol. 44, p. 323–346, 2012.

[54] T. Belytschko, Y. Krongauz, D. Organ, M. Fleming, and P. Krysl, "Meshless methods: An overview and recent developments," *T. Belytschko, Y. Krongauz, D. Organ, M. Fleming, and P. Krysl. Meshless methods: An overview and recent Computer Methods in Applied Mechanics and Engineering,* Vols. T. Belytschko, Y. Krongauz, D. Organ, M. Fleming, and P. Krysl. Meshless methods: An

overview and recent 139, no. T. Belytschko, Y. Krongauz, D. Organ, M. Fleming, and P. Krysl. Meshless methods: An overview and recent 1 - 4, pp. T. Belytschko, Y. Krongauz, D. Organ, M. Fleming, and P. Krysl. Meshless methods: An overview and recent 3 – 47, T. Belytschko, Y. Krongauz, D. Organ, M. Fleming, and P. Krysl. Meshless methods: An overview and recent 1996.

[55] A. Chaniotis, *Remeshed Smoothed Particle Hydrodynamics for the Simulation of Compressible, Viscous, Heat Conducting, Reacting and Interfacial Flows,* A. Chaniotis. Remeshed Smoothed Particle Hydrodynamics for the Simulation of Compressible, Viscous, Heat ConductiPhD thesis, Swiss Federal Institute of Technology Zurich, A. Chaniotis. Remeshed Smoothed Particle Hydrodynamics for the Simulation of Compressible, Viscous, Heat Conducti2002.

[56] L. B. Lucy, "A numerical approach to the testing of the fission hypothesis," *Astronomical Journal,* vol. 82, p. 1013–1024, 1977.

[57] R. A. Gingold and J. J. Monaghan, "R. A. Gingold and J. J. Monaghan. Smoothed particle hydrodynamics: theory and application to non-spherical stars," *Monthly Notices of the Royal Astronomical Society,* vol. 181, pp. 375-389, 1977.

[58] Liu MB, Liu GR, "Smoothed Particle Hydrodynamics (SPH): an overview and recent developments," *Arch Computer Methods Eng. ,* vol. 17, p. 25–76, 2010.

[59] T. Rung and C. Ulrich, in *6th Int. Spheric Workshop*, Schriftenreihe Schiffbau, 2011.

[60] J. J. Monaghan, "Simulating Free Surface Flows with SPH," *Journal of Computational Physics,* vol. 110, p. 399–406, 1994.

[61] S. Marrone, A. Colagrossi, M. Antuono, C. Lugni, and M.P. Tulin, "A 2d+t sph model to study the breaking wave pattern generated by fast ships," *Journal of Fluids and Structures,* vol. 27, no. 8, p. 1199–1215, 2011.

[62] L.-C. Qiu, "Two-Dimensional SPH simulations of landslide-generated water waves," *J. Hydraulic Engineering,* vol. 134, p. 668–671, 2008.

[63] M. Pastor, B. Haddad, G. Sorbino, S. Cuome, and V. Drempetic, "A depth-integrated, coupled SPH model for flow-like landslides and related phenomena," *Int. J. Numer. And Anal. Meth. in Geomech.,* vol. 33, p. 143–172, 2009.

[64] S. Manenti, S. Sibilla, M. Gallati, G. Agate, and R. Guandalini, "SPH Simulation of Sediment Flushing Induced by a Rapid Water Flow," *Journal of Hydraulic Engineering,* vol. 138, no. 3, p. 272–284, 2012..

[65] R. Vacondio, B. D. Rogers, P. K. Stansby, and P. Mignosa, "SPH modeling of shallow flow with open boundaries for practical flood simulation," *J. Hydraulic Engineering,* vol. 138, p. 530–541, 2012.

[66] H. H. Bui, R. Fukagawa, K. Sako, and S. Ohno, "Lagrangian meshfree particles method (SPH) for large deformation and failure flows of geomaterial using elasticplatic soil constitutive model," *H. H. Bui, R. Fukagawa, K. Sako, and S. Ohno. Lagrangian meshfree particles method (SPH) for large deformation and failure flows of geomaterialJ. Numer. Anal. Meth. Geomech.,* vol. 32, p. 1537–1570, 2008.

[67] H. H. Bui, C. T. Nguyen, K. Sako, and R. Fukagawa , "A SPH model for seepage flow through deformable porous media," in *6th Int. SPHERIC workshop, pages 164–171*, , 2011 .

[68] Libersky LD, Petschek AG, Carney TC, Hipp JR, Allahdadi FA, "High strain Lagrangian hydrodynamics: a three-dimensional SPH code for dynamic material response," *Journal of Computational Physics ,* vol. 109, pp. 67-75, 1993.

[69] L. LB., "A numerical approach to the testing of fission hypothesis," *Astronom. J. ,* vol. 82, p. 1013–24, 1977.

[70] Gingold RA, Monaghan JJ, "Smoothed particle hydrodynamics: theory and applications to non-spherical stars," *Monthly Notices of the Royal Astronomical Society ,* vol. 181, p. 375–89, 1977.

[71] D. Violeau, Fluid Mechanics and the SPH Method: Theory and Applications, Oxford Univ Press, 2012.

[72] Longatte E, Bendjeddou Z, Souli M, "Application of Arbitrary Lagrange Euler Formulations to Flow-Induced Vibration problems," *Journal of Pressure Vessel and Technology,* vol. 125, no. 4, pp. 411-417, 2003.

[73] Longatte E, Verreman V, Souli M, "Time marching for simulation of Fluid-Structure Interaction Problems," *Journal of Fluids and Structures,* vol. 25, no. 1, pp. 95-111, 2009.

[74] Erchiqui F, Bendada A, Gakwaya A, Kandil N, "Dynamic finite element analysis of forming process in long fiber reinforced hyperelastic materials," in *AIP Conf. Proc.*, 712-21, 2004.

[75] E. H., "YouTube," Hisham Elkenani, 7 Dec 2014. [Online]. Available: https://www.youtube.com/watch?v=XuBbHlWX1ic.

[76] S. Adami, X.Y. Hu, N.A. Adams, "A generalized wall boundary condition for smoothed particle hydrodynamics," *Journal of Computational Physics,* vol. 231, no. 21, p. 7057–7075, 2012.

[77] Souli M, Zolesio JP, "Shape derivative of discretized problems," *Computer Methods in Applied Mechanics and Engineering,* vol. 108, p. 187–99, 1993.

[78] Erchiqui F, Souli M, Ben Yedder R, "Nonisothermal finite-element analysis of thermoforming of polyethylene terephthalate sheet: Incomplete effect of the forming stage," *Polymer Engineering and Science,* vol. 47, no. 12, pp. 2129-44. , 2007.

[79] E. 9, "Design of aluminum structures - Structures susceptible to fatigue.".

[80] R. S., Mathematical analysis of random noise, New York: Dover, 1954.

[81] B. J., "Probability functions for random responses: prediction of peaks, fatigue damage, and catastrophic failures," NASA, 1964.

[82] Braccesi C., Cianetti F., Lori G., Pioli D., "Fatigue behaviour analysis of mechanical components subject to random bimodal stress process: frequency domain approach," *International Journal of Fatigue,* vol. 27, no. 4, pp. 335-345, 2005.

[83] Al-Bahkali E., Elkanani H., Souli M., "Fatigue Life Estimate of Landing Gear's Leg Using Modal Analysis," *The International Journal of Multiphysics,* vol. 8, no. 2, pp. 231-244, 2014.

[84] Clough, R. W., and Penzien, J., Dynamics of Structures, New York: McGraw-Hill, 1975.

[85] Preumont A., Piefort V., "Predicting Random High-Cycle Fatigue Life With Finite Elements," *Journal of Vibration and Acoustics,* vol. 116, no. 2, p. 245–248, 1994.

[86] Bonte M. H. A., de Boer A., Liebregts R., "Determining the von Mises stress power spectral density for frequency domain fatigue analysis including out-of-phase stress components," *Journal of Sound and Vibration,* vol. 302, no. 1-2 , p. 379–386, Apr., 2007.

[87] Segalman D. J., Fulcher C. W. G., Reese G. M., Field R. V., Jr., "An Efficient Method for Calculating RMS von Mises Stress in a Random Vibration Environment," Sandia Report, SAND98-0260, 1998.

[88] D. T., *Application of computers in fatigue analysis,* Ph.D. thesis: The University of Warwick, 1985.

[89] Mršnik M., Slavic J., Boltezar M., "Frequency-domain methods for a vibration-fatigue-life estimation – Application to real data," *International Journal of Fatigue,* vol. 47, p. 8–17, Feb., 2013.

[90] Zalaznik A, Nagode M., "Frequency based fatigue analysis and temperature effect," *Materials and Design,* vol. 32, no. 10, p. 4794–802, 2011.

[91] H. A., *A frequency domain approach for fatigue life estimation from Finite Element Analysis,* Sheffield UK: nCode® International Ltd, 1999.

[92] *LS-DYNA® Keyword User's Manual, Version 971,* Livermore, California: Livermore Software Technology Corporation, 2012.

[93] Huang Y., Souli M., Ashcraft C., Grimes R., Wang j., Rassaian M., Lee J., "Development of frequency domain dynamic and acoustic capability in LS-DYNA®," in *Proceedings of the 8th European LS-DYNA® Users Conference*, Strasbourg, May, 2011..

[94] Nagulapalli, V.K., Gupta, A., Fan, S., "Estimation of fatigue life of aluminum beams subjected to random vibration," in *IMAC-XXV: Conference & Exposition on Structural Dynamics*, Orlando, Florida, Feb. 19-22, 2007.

[95] Longatte, F., Bendjeddou, Z., Souli, M., "Methods for numerical study of tube bundle vibrations in cross-flows," *J. Fluids Struct,* vol. 18, no. 5, p. 513–528, 2003.

[96] Longatte, F., Kueny JL., "Analysis of rotor-stator-circuit interactions in a centrifugal pump," in *Proceedings of the 3rd ASME/JSME Joint Fluids Engineering Conference*, 2009.

[97] "Design of aluminium structures - Part 1-3: Structures susceptible to fatigue," Eurocode 9, Aug., 2011.

[98] T. Irvine, "dB Calculator," [Online]. Available: www.vibrationdata.com.

[99] "Test Method Standard: Envronmental Engineering Considerations and Laboratory Tests, MIL-STD-810G," Department of Defense, USA, Oct., 31, 2008.

[100] Richard G. Budynas, J. Keith Nisbett, Shigley's Mechanical Engineering Design, Ninth Edition ed., McGraw Hill, 2011.

[101] Matta A., Kumar G., Kumar R., "Design optimisation of landing gear's leg for an un-manned aerial vehicle," *International Journal of Engineering Research and Applications (IJERA) ISSN: 2248-9622,* vol. 2, no. 4, pp. 2069-2075, July-August 2012.

[102] Albahkali E., Alqhtani M., *Design of light landing gear,* Riyadh, KSA: Graduate Project, King Saud University, June, 2011.

[103] C. A. Taylor, T. J. R. Hughes, and C. K. Zarins, "Finite element modeling of blood flow in arteries," *Computer Methods in Applied Mechanics and Engineering,* vol. 158. , p. 155–196, 1998.

[104] R. Torii, M. Oshima, T. Kobayashi, K. Takagi, and T.E. Tezduyar, "Influence of wall elasticity on image-based blood flow simulation," *Japan Society of Mechanical Engineers Journal Series A,* vol. 70, p. 1224–1231, 2004.

[105] R. Torii, M. Oshima, T. Kobayashi, K. Takagi, and T.E. Tezduya, "Influence of the wall elasticity in patient-specific hemodynamic simulations," *Computers and Fluids,* vol. 36, pp. 160-168, 2007.

# Appendix A: List of the Published Papers

1. **Elkanani Hesham,** Al-Bahkali Essam, Souli Mhamed "Numerical Investigation of Pulse Wave Propagation in Arteries Using Fluid Structure Interaction Capabilities", Computational and Mathematical Methods in Medicine, Volume 2017, Article ID 4198095, pages 1-12, 2017.
   https://doi.org/10.1155/2017/4198095

2. Al-Bahkali Essam, **Elkanani Hesham**, Souli Mhamed "Experimental and numerical investigation for membrane deployment using SPH and ALE formulations", Computer Modeling in Engineering & Sciences, 104(5), pp 405-424, 2015.

3. Al-Bahkali Essam, **Elkanani Hesham**, Souli Mhamed "Failure and fatigue life estimate of a pre-stressed aircraft seat support tube", Engineering Failure Analysis, 54, pp 120-130, 2015.
   http://dx.doi.org/10.1016/j.engfailanal.2015.04.001

4. Al-Bahkali Essam, **Elkanani Hesham**, Souli Mhamed "Failure of an Aircraft Seat Support Tube", Multiphysics 2014 Conference, Dec 11-12, 2014, Sofia, Bulgaria.
   http://www.multiphysics.org/MULTIPHYSICS%202014%20-%20Abstracts.pdf

5. Al-Bahkali Essam, **Elkanani Hesham**, Souli Mhamed "SPH and ALE Methods for Membrane Inflation", Multiphysics 2014 Conference, Dec 11-12, 2014, Sofia, Bulgaria.
   http://www.multiphysics.org/MULTIPHYSICS%202014%20-%20Abstracts.pdf

6. Al-Bahkali Essam, **Elkanani Hesham**, Souli Mhamed "Fatigue Life Estimate of Landing Gear's Leg Using Modal Analysis", The International Journal of Multiphysics, 8(2), pp. 231-244, June 2014.
   http://multi-science.metapress.com/content/7q62602610017864/?p=6f22ecf3a3ec4cdea273bf55c7845fd1&pi=5

7. Al-Bahkali Essam, **Elkanani Hesham**, Souli Mhamed "Random Vibration and Fatigue Analysis Using Modal Analysis", Multiphysics 2013 Conference, Dec 12-13, 2013, Amsterdam, The Netherlands.
   http://www.multiphysics.org/images/MULTIPHYSICS%202013-Abstracts.pdf

8. Al-Bahkali Essam, **Elkanani Hesham**, Souli Mhamed "NVH and Random

Vibration Fatigue Analysis of a Landing Gear's Leg for an Un-Manned Aerial Vehicle Using LS-DYNA", 9th European LS-DYNA Users' Conference, June 2-4, 2013 Manchester, UK.
http://www.dynalook.com/9th-european-ls-dyna-conference/nvh-and-random-vibration-fatigue-analysis-of-a-landing-gearss-leg-for-an-un-manned-aerial-vehicle-using-ls-dyna-r

# Appendix B: List of Elements Conversion Keyword Code

```
*Heading
** Job name: Memprane_Inflation Model name: Model-1
** Generated by: Abaqus/CAE 6.13-1
*Preprint, echo=NO, model=NO, history=NO, contact=NO
**
** PARTS
**
*Part, name=Air
*Node
      1,           0.,           0., 0.0299999993
      2, -0.00176117313, -0.0317011178, 0.0299999993
      3, 0.0317011178, -0.00176117313, 0.0299999993
      ..........................................
      ..........................................

*Element, type=C3D8R
   1,  561,  562,  657,  654,   34,   35,  130,  127
   2,  562,  563,  658,  657,   35,   36,  131,  130
   3,  563,  564,  659,  658,   36,   37,  132,  131
   ..............................................
   ..............................................

*Nset, nset=Whole_Air, generate
    1,  5797,     1
*Elset, elset=Whole_Air, generate
    1,  4920,     1
*Nset, nset=Air_nodes, generate
    1,  5797,     1
** Section: Air_Sec
*Solid Section, elset=Whole_Air, controls=EC-1, material=Air
,
*End Part
**
*Part, name=Membrane
*Node
      1,  0.031750001,           0.,           0.
      2,           0., 0.0299999993, -0.031750001
      3, -0.031750001, 0.0299999993,           0.
      ......................................
      ......................................

*Element, type=S4R
  1,   1,  72, 146,  73
```

```
  2,  72,  71, 147, 146
  3,  71,  70, 148, 147
  ......................
  ......................

*Nset, nset=Whole_Membrane, generate
    1,  1139,     1
*Elset, elset=Whole_Membrane, generate
    1,  1104,     1
*Nset, nset=Fixed_Surface, generate
   1,  748,    1
*Elset, elset=Fixed_Surface, generate
   1,  680,    1
*Nset, nset=Membrane_Lower_Surface
    2,    3,    4,    5,   82,   83,   84,   85,   86,   87,
88,   89,   90,   91,   92,   93
   ......................................................
   ......................................................

*Elset, elset=Membrane_Lower_Surface, generate
  681,  1104,     1
*Nset, nset=Pole_Node
 770,
*Elset, elset=_Membrane_Lower_Surf_SNEG, internal, generate
  681,  1104,     1
*Surface, type=ELEMENT, name=Membrane_Lower_Surf
_Membrane_Lower_Surf_SNEG, SNEG
** Section: Shell_Sec
*Shell Section, elset=Whole_Membrane, material=Rubber
0.00157, 5
*End Part
**
*Part, name=Piston
*Node
      1,           0.,           0., -0.031750001
      2,           0.,           0.,           0.
      3, -0.031750001,           0.,           0.
      ........................................
      ........................................

*Element, type=R3D4
 1, 14, 15, 40, 38
 2, 15, 16, 39, 40
 3, 16,  1,  6, 39
 ..................
 ..................

*Node
     74,           0.,           0.,           0.
*Nset, nset=Piston-RefPt_, internal
74,
```

```
*Nset, nset=Set-Ref_Point
 74,
*Elset, elset=_Piston_Upper_Surf_SNEG, internal, generate
  1,  60,   1
*Surface, type=ELEMENT, name=Piston_Upper_Surf
_Piston_Upper_Surf_SNEG, SNEG
*Elset, elset=_Piston_Lower_Surf_SPOS, internal, generate
  1,  60,   1
*Surface, type=ELEMENT, name=Piston_Lower_Surf
_Piston_Lower_Surf_SPOS, SPOS
*Elset, elset=Piston, generate
  1,  60,   1
*Element, type=MASS, elset=Set-Ref_Point_Inertia-1_
61, 74
*Mass, elset=Set-Ref_Point_Inertia-1_, alpha=0.02
10.,
*End Part
**
**
** ASSEMBLY
**
*Assembly, name=Assembly
**
*Instance, name=Air-1, part=Air
          0.,           0.,           0.
          0.,           0.,           0.,          -1.,
0.,           0.,          90.
*End Instance
**
*Instance, name=Membrane-1, part=Membrane
*End Instance
**
*Instance, name=Piston-1, part=Piston
*End Instance
**
*Rigid Body, ref node=Piston-1.Piston-RefPt_, elset=Piston-
1.Piston
*End Assembly
**
** ELEMENT CONTROLS
**
*Section Controls, name=EC-1, ELEMENT CONVERSION=YES, CONVERSION
CRITERION=TIME, KERNEL=CUBIC
1., 1., 1.


1, 0.
*Amplitude, name=Amp-Force, Value=Absolute
            0.,             0.,          0.018,
0.,         0.03445,          1.185,           0.07,
4.9375
```

```
         0.1007,            8.69,        0.133825,
.....................................................
.....................................................

*Amplitude, name=Amp-Pressure, Value=Absolute
   0.,              0.,           0.018,              0.,
0.03445,            375.,            0.07,          1562.5
         0.1007,           2750.,        0.133825,
.....................................................
.....................................................

*Amplitude, name=Amp-Volume
             0.,              0.,       0.0180021,
0.,       0.0330028,      0.14597219,       0.0720056,
0.181264465
       0.102005,     0.263595704,        0.132004,
.....................................................
.....................................................

*Amplitude, name=Displacement
             0.,              0.,             0.6,
1.
**
** MATERIALS
**
*Material, name=Air
*Density
 1.127,
*Eos, type=IDEALGAS
 286.9,101325.
*Specific Heat
 1006.4,
*Viscosity
 1.983e-05,
*Material, name=Rubber
*Damping, alpha=0.6, beta=3e-05
*Density
1100.,
*Hyperelastic, mooney-rivlin
105000.,10500.,    0.
**
** INTERACTION PROPERTIES
**
*Surface Interaction, name=IntProp-1
*Surface Behavior, pressure-overclosure=HARD
**Fluid Behavior, name=IntProp-1
**Molecular Weight
**0.0289
**Capacity, type=POLYNOMIAL
**28.11,   0.001967,  4.802e-06, -1.966e-09,         0.
**
```

```
** PHYSICAL CONSTANTS
**
*Physical Constants, absolute zero=-273.15, universal gas=8.31434
**
** BOUNDARY CONDITIONS
**
** Name: Fixed_Surface Type: Symmetry/Antisymmetry/Encastre
*Boundary
Membrane-1.Fixed_Surface, ENCASTRE
** ----------------------------------------------------------------
--
**
** STEP: Step-1
**
*Step, name=Step-1, nlgeom=YES
*Dynamic, Explicit
, 0.6
*Bulk Viscosity
0.06, 1.2
**Boundary, Type=Displacement, Amplitude=Displacement
**Piston-1.Piston-RefPt_,2,2,0.1
**Boundary, Type=Velocity
**Piston-1.Piston-RefPt_,2,2,0.045
*Boundary, Type=Displacement
Piston-1.Piston-RefPt_,1,1
**Boundary, Type=Displacement
**Piston-1.Piston-RefPt_,2,2
*Boundary, Type=Displacement
Piston-1.Piston-RefPt_,3,3
*Boundary, Type=Displacement
Piston-1.Piston-RefPt_,4,4
*Boundary, Type=Displacement
Piston-1.Piston-RefPt_,5,5
*Boundary, Type=Displacement
Piston-1.Piston-RefPt_,6,6
**
** LOADS
**
** Name: Load-Force   Type: Concentrated force
*Cload, amplitude=Amp-Force
Piston-1.Set-Ref_Point, 2, 1.
**
** INTERACTIONS
**
** Interaction: Int-1
*Contact, op=NEW
*Contact Inclusions, ALL EXTERIOR
*Contact Property Assignment
 ,  , IntProp-1
**
** OUTPUT REQUESTS
```

```
**
*Restart, write, number interval=1, time marks=NO
**
** FIELD OUTPUT: F-Output-1
**
*Output, field, variable=PRESELECT
**
** HISTORY OUTPUT: H-Output-1
**
*Output, history
*Node Output, nset=Membrane-1.Pole_Node
U2,
**
** HISTORY OUTPUT: H-Output-2
**
*Element Output, elset=Air-1.Whole_Air
PRESS,
*End Step
```

# Appendix C: Letter of Appreciation

LSTC
Livermore Software Technology Corp.

Livermore Software Technology Corporation • 7374 Las Positas Road Livermore, CA 94551
Telephone: (925) 449-2500 • Fax: (925) 449-2507 • Website: www.lstc.com

February 14, 2014

King Saud University
Prof. Khalid Ibrahem Alhumaizi
College of Engineering
Office of the Dean
P.O. Box 2459
Riyadh, Saudi Arabia 11451
By E-Mail: humaizi@ksu.edu.sa

Dear Prof. Alhumaizi;

I would like to bring to your attention the assistance Mr. Hisham Elkenani provided our engineer, Dr. Yun Huang, in debugging a Keyword input error in our pre/post processor, LS-PrePost. With his help, our developers were able to locate and correct the coding error.

The error was revealed while Mr. Elkenani and Dr. Huang were attempting to solve a random vibration analysis problem with our LS-DYNA software. Mr. Elkenani's cooperation and feedback contributed to improving the operability of our software and is greatly appreciated.

Regards,

John O. Hallquist

John O. Hallquist
President

cc: Mr. Hisham Elkenani

# Table of Contents